

***Multi-modal Analysis of Metabolic  
Enzyme Disruption in Adipocytes***

A dissertation

submitted by:

**James Kenneth Sims**

In partial fulfillment of the requirements

for the degree of

Doctor of Philosophy

in

*Chemical Engineering*

**Tufts University**

February 2015

ADVISOR: Kyongbum Lee, Ph.D



## ***Abstract***

Obesity results from a chronic imbalance in caloric intake and expenditure. The excess calories are stored mainly as lipids (triglycerides, TG), leading to an expansion of body fat or adipose tissue through increases in fat cell (adipocyte, AD) size and number. One approach to controlling body fat could be to intervene in the metabolic processes of the adipose tissue that directly contribute to lipid accumulation and cell growth. The goal of this study is to investigate targets for reducing AD size and TG accumulation via RNAi-mediated gene silencing (i.e. siRNA knockdown) of metabolic proteins. Targets for siRNA knockdown were selected based on our knowledge of adipocyte metabolism, and were identified from each stage of lipid accumulation: early synthesis (breakdown and transformation of glycolysis intermediates into precursors of fatty acid synthesis), late synthesis (formation of triglyceride from synthesized precursors), and droplet stability (protection from intracellular lipases and formation of larger lipid droplets). Pyruvate carboxylase (PCX) and isocitrate dehydrogenase (IDH) were identified as targets for early synthesis, diglyceride acyltransferase (DGAT) for late synthesis, and fat-specific protein 27 (FSP) and perilipin (PLIN) for droplet stability.

In addition to monitoring TG accumulation via conventional, destructive biochemical assays, we developed an image processing method, which identifies LDs in microscopy images, and quantifies their number, size distribution, and total lipid content. This method could prospectively be used as a high-throughput screening method for a variety of applications. We also conducted a metabolomic

analysis and isotopic labeling experiments to understand how disrupting each enzyme affected metabolite concentrations and reaction fluxes across the entire metabolic network. We have shown successful knockdown of several metabolic proteins, which led to reduction in accumulation of triglycerides; however, inhibition of PCX and DGAT had the greatest individual effects. Interestingly, DGAT and FSP had the greatest combined effect on and this combination was selected for further analysis. Prospectively, results from this study could be used to identify potential therapeutic targets for treating obesity, guided by an improved understanding of how the enzymes and LD proteins regulate the balance of TG in adipocytes.

## ***Table of Contents***

Abstract .....	iii
List of Figures .....	viii
List of Tables .....	viii
1 Introduction.....	1
1.1 Hypertrophy in Adipocytes.....	2
1.2 Methods for Analysis of Tissue Metabolism .....	5
1.2.1 Methods for Quantitative Analysis of Metabolic Flux .....	7
1.2.2 Metabolic Flux Analysis of Mammalian Cells and Tissues.....	9
1.2.3 Genome-scale Metabolic Analysis.....	12
1.2.4 Spatiotemporally Resolved Metabolic Analysis .....	14
1.3 Thesis Outline .....	17
Chapter 2 .....	17
Chapter 3 .....	17
Chapter 4 .....	18
Chapter 5 .....	18
2 Identification of Enzyme Targets to Reduce Triglyceride Accumulation .....	19
2.1 Abstract.....	19
2.2 Introduction.....	20
2.3 Materials and Methods.....	26
2.3.1 Materials .....	26
2.3.2 Cell culture.....	26
2.3.3 Three-Dimensional Co-culture .....	27
2.3.4 siRNA Transfection .....	28
2.3.5 Triglyceride accumulation and DNA content .....	29
2.3.6 Real time RT-PCR .....	29
2.3.7 Microscopy and Manual Image Analysis.....	30
2.4 Results.....	30
2.4.1 Perilipin Knockdown Reduces TG Accumulation.....	30
2.4.2 Manual Image Analysis of Perilipin Knockdown.....	31
2.4.3 Gene Expression .....	32
2.4.4 Targeted Knockdown Reduces TG Accumulation .....	33
2.5 Discussion.....	34
3 Image Processing Algorithm for Non-invasive Analysis of Lipid Droplets.....	37
3.1 Abstract.....	37
3.2 Introduction.....	38

3.3	Methods.....	41
3.3.1	Materials .....	41
3.3.2	Cell culture.....	41
3.3.3	Enzymatic assay.....	42
3.3.4	Microscopy .....	42
3.3.5	Image Processing Overview.....	43
3.3.6	Calculating LD Size, Volume, and Distribution.....	51
3.4	Results.....	52
3.4.1	Comparison with ground truth .....	52
3.4.2	Comparison with biochemical data .....	54
3.4.3	Culture heterogeneity.....	55
3.4.4	Size distribution of LDs .....	56
3.4.5	Comparison of Imaging Modalities .....	58
3.5	Discussion.....	60
4	Analysis of Network-wide Effects of Individual Enzyme Knockdown.....	70
4.1	Abstract.....	70
4.2	Introduction.....	71
4.3	Materials and Methods.....	73
4.3.1	Materials .....	73
4.3.2	Cell culture.....	73
4.3.3	siRNA Transfection .....	74
4.3.4	Metabolite Extractions .....	74
4.3.5	LC-MS .....	75
4.3.6	Principal Component Analysis and Hierarchical Clustering.....	76
4.4	Results.....	77
4.4.1	Measured Metabolite Levels and Extracellular Fluxes.....	77
4.4.2	Principal Component Analysis.....	78
4.5	Discussion.....	82
5	Coordinated Knockdown of Multiple Targets .....	85
5.1	Abstract.....	85
5.2	Introduction.....	86
5.3	Materials and Methods.....	88
5.3.1	Materials .....	88
5.3.2	Cell culture.....	88
5.3.3	siRNA Transfection .....	89
5.3.4	Triglyceride assay .....	90

5.3.5	Metabolite Extractions .....	90
5.3.6	LC-MS .....	91
5.3.7	Stoichiometric Model.....	91
5.3.8	Isotopomer Model.....	92
5.3.9	Isotopomer Measurements .....	92
5.3.10	Target Metabolites .....	93
5.4	Results.....	94
5.4.1	Metabolic Network Mapping.....	94
5.4.2	Reduced TG Accumulation in Coordinated Double Knockdown.....	95
5.4.3	Metabolite Levels and Measured Extracellular Fluxes.....	96
5.4.4	Mass Isotopomer Distribution.....	96
5.4.5	Flux Profiles.....	98
5.4.6	Analyzing Network-wide Effects of Knockdown.....	98
5.5	Discussion.....	100
	Future Directions and Recommendations .....	104
	Appendix A: Sample Code for Image Analysis Algorithm.....	108
	Appendix B: Solvent and Column Info for LC-MS/MS .....	118
	TCA Cycle/Glycolysis/Cofactors.....	118
	Amino Acids.....	118
	Fatty Acids .....	118
	Appendix C: Measured Metabolites (Individual Knockdown) .....	119
	Appendix D: Principal Component Analysis .....	121
	Appendix E: Hierarchical Clustering .....	122
	Appendix F: Reaction stoichiometry of the model network.....	123
	Appendix G: Measured Metabolites (Double Knockdown).....	125
	Appendix H: Workflow for MID Measurements .....	127
	Appendix I: Mass Isotopomer Distributions .....	132
	Appendix J: Results of Isotopomer Model.....	133
	References .....	137

## ***List of Figures***

Figure 2-1: Triglyceride Accumulation Pathway .....	21
Figure 2-2: Triglyceride Accumulation in 3D Co-culture.....	31
Figure 2-3: Manual Analysis of Adipocyte Images.....	31
Figure 2-4: Perilipin mRNA Levels .....	32
Figure 2-5: Triglyceride Accumulation in 2D Culture.....	33
Figure 3-1: Overview of Image Processing Algorithm.....	45
Figure 3-2: Representative Grayscale Images .....	47
Figure 3-3: Pixel Histograms for Representative Images.....	47
Figure 3-4: Illustration of Processing Steps .....	53
Figure 3-5: Calculated vs Enzymatically measured TG content .....	55
Figure 3-6: Heat Maps Showing Culture Heterogeneity.....	56
Figure 3-7: Average Number of Droplets per Image .....	57
Figure 3-8: Droplet Size Distribution.....	57
Figure 3-9: Representative Image Under Different Modalities.....	58
Figure 3-10: Comparison of Different Modalities.....	59
Figure 3-11: Droplet Size Distribution from BF, DIC and PC Images .....	60
Figure 3-12: Representative Images Taken Over Time.....	66
Figure 3-13: Representative Set of Processed BF, DIC, and PC Images .....	69
Figure 4-1: Principal Component Analysis (Over Time).....	78
Figure 4-2: Components Scores (Over Time) .....	79
Figure 4-3: Principal Component Analysis (Day 8 and 14).....	80
Figure 4-4: Heatmap of Normalized Metabolite Concentrations (Day 8).....	81
Figure 5-1: Example Knockdown Strategy for Reducing TG Accumulation .....	86
Figure 5-2 Network map of adipocyte metabolism.....	94
Figure 5-3 Reduction in Intracellular Triglyceride Concentration.....	95
Figure 5-4 Metabolic Changes of Double Knockdown.....	99
Figure S-1: Component Scores (Day 8) .....	121
Figure S-2: Component Scores (Day 14) .....	121
Figure S-3: Hierarchical Clustering of Metabolites (Day 8) .....	122

## ***List of Tables***

Table 1: Abridged List of Enzymes involved in TG Accumulation.....	22
Table 2: siRNA sequences of target enzymes .....	29
Table 3: Intracellular Metabolite Concentrations.....	119
Table 4: Extracellular Flux Measurements.....	120
Table 5: Stoichiometric model for the adipocyte network .....	123
Table 6: Intracellular Metabolite Concentrations (Double KD).....	125
Table 7: Extracellular Flux Measurements (Double KD) .....	126
Table 8: Mass Isotopomer Distribution (Double KD).....	132
Table 9: Flux Estimates (Double KD).....	133
Table 10: Glucose Normalized Fluxes (Double KD).....	135



## ***1 Introduction***

In adults, body fat essentially consists of white adipose tissue (WAT). Distributed across the body in various depots, WAT performs metabolic as well as signaling functions critical for whole body homeostasis. The core metabolic functions of WAT are to store excess nutrients as esterified lipids (i.e. triglycerides, TGs) and to mobilize these stores during fasting. The bulk of WAT cellular mass consists of lipid-laden white adipocytes, held in a dense network of fibrous extracellular matrix (ECM) proteins. Differentiated adipocytes express high levels of enzymes for lipid uptake, synthesis, storage, and breakdown. *In vivo*, almost the entire adipocyte volume is filled by a single large lipid droplet (LD), which expands or shrinks depending on the body's energy balance. Chronic overfeeding can lead to significant expansion of adipocyte volume, termed hypertrophy, to accommodate the storage of excess nutrients as lipids. This expansion requires a reorganization of the surrounding ECM as well as neovascularization for adequate oxygen supply. Hypertrophic expansion cannot proceed without limit; it is thought that recruitment and differentiation of locally resident precursor cells may also be necessary to accommodate additional lipid stores. Adipocyte hypertrophy, especially in the context of obesity, correlates with accumulation of pro-inflammatory immune cells in WAT, which in turn underpins tissue insulin resistance and other metabolic alterations associated with obesity-related metabolic diseases.

## ***1.1 Hypertrophy in Adipocytes***

There is now increasing evidence that mechanistic relationships exist between adipocyte hypertrophy, tissue remodeling, inflammation, and metabolic alterations (Lee & Kuo, 2015). Several biochemical explanations have been proposed to connect tissue remodeling and inflammation, including hypoxia-induced deposition of excess collagen (Sun, 2011). In obese subjects, adipose expandability could be compromised, as deposition of fibrillar ECM proteins outpaces MMP activity, resulting in fibrosis. It remains an open question whether fibrosis acts to limit differentiation of precursor cells into adipocytes, expansion of mature adipocytes, or both. Regardless, the ensuing “stiffening” of the tissue could further contribute to a state of metabolic stress by favoring the hydrolysis of stored TG, i.e. lipolysis, over fatty acid esterification and storage.

Normally, lipolysis is under tight hormonal regulation. Catecholamine stimulation activates hormone-sensitive lipase (HSL) through a G-protein coupled receptor (GPCR)-dependent signalling cascade mediated by protein kinase A (PKA). Insulin potently inhibits lipolysis by activating a phosphodiesterase (PDE3B) to lower the intracellular level of cAMP and reduce PKA activity, thereby attenuating post-translational activation of HSL. Under conditions of fibrosis and limited adipose expandability, excess free fatty acids that cannot be stored as esterified lipids could establish a positive feedback loop for elevated lipolysis, as the metabolite products of HSL are putative ligands or pro-ligands for peroxisome proliferator-activated receptor- $\gamma$  (PPAR $\gamma$ ) (Shen, 2011). The transcription factor PPAR $\gamma$  is a key regulator of differentiation adipocyte function

whose many metabolic targets include adipose triglyceride lipase (ATGL), a lipolytic enzyme that acts upstream of HSL.

Experiments with isolated cells from human subcutaneous WAT showed that both basal and hormone stimulated lipolysis positively correlates with cell size (Laurencikiene, 2011). The same study also observed higher expression of lipolytic enzymes hormone sensitive lipase (HSL) and ATGL in larger adipocytes. These and other metabolic studies on hypertrophic adipocytes suggest that increased lipolysis, sustained over time, could overwhelm the re-esterification capacity of WAT depots, and up-regulate net fatty acid efflux (Mitrou, 2010). Elevation of extracellular free fatty acid levels in turn could further promote local inflammation through a variety of signaling mechanisms involving recruitment and/or polarization of macrophages (Lumeng, 2007, 2008; Nguyen, 2007) . In addition to fatty acids, the levels of several immune cell recruitment factors are elevated in WAT of obese individuals. An important factor linking adipose tissue inflammation with metabolic phenotypes characteristic of obesity is the monocyte chemoattractant protein-1 (MCP-1). Adipose-specific overexpression of MCP-1 in mice led to insulin resistance, higher levels of free fatty acids in circulation, and greater accumulation of macrophages and elevated expression of pro-inflammatory cytokines in WAT (Kamei, 2006).

Almost all macrophages in adipose tissue localize to dying/dead adipocytes, where they scavenge residual free lipid droplets and fuse with other macrophages to form multinucleate giant cells (Cinti, 2007). This would suggest that adipocyte death is an early event in WAT macrophage recruitment and inflammation

(Strissel, 2007). However, recent studies with granulocyte/monocyte-colony stimulating factor-null mice showed that HFD induced adipocyte death can occur independently of macrophage infiltration and activation (Feng, 2011), which suggests that macrophage recruitment and activation could result from, rather than cause, adipocyte hypertrophy and cell death.

Adipocytes are unique in their ability to expand in volume by a factor near 1000x. This is largely due to their role as a storage depot for esterified lipids. However, TG synthesis is a complex pathway which involves many metabolic and regulatory pathways, with complex interactions. These pathways are described in further detail in Chapter 2. Briefly, TG accumulation can be roughly broken down into three stages: upstream synthesis, downstream synthesis and droplet stability. Upstream synthesis involves the formation of precursor metabolites (i.e. glycerol and acetyl-coA) from intermediates of glycolysis and the TCA cycle. Acetyl-coA is the building block for biosynthesis of fatty acids which are then esterified to a glycerol backbone (downstream synthesis).

Once TG is synthesized, it is sequestered in intracellular lipid droplets, which are stabilized by a variety of proteins that shield the droplets from intracellular lipases. Ultimately, a single LD occupies almost the entire volume of the cell. As more TG is accumulated, the LD continues to grow, and so does the cell itself (i.e., hypertrophy). These pathways are tightly interconnected and highly regulated as well. Therefore, it is the goal of this study to examine these pathways using a systems approach. There are several new methods available for the metabolic analysis of tissues, which will be described in the following section.

## ***1.2 Methods for Analysis of Tissue Metabolism<sup>1</sup>***

Metabolism refers to biochemical processes that extract chemical energy from nutrients (or solar energy in the case of phototrophic organisms), and use this energy to convert nutrients into building blocks for biosynthesis. The intermediates of these processes, i.e. metabolites, also act as regulatory molecules that coordinate the activities of metabolic pathways and other cellular pathways such as signaling. Even for cells and tissues whose primary physiological role is not metabolic *per se*, e.g. immune cells (Bordbar, 2012), there is increasing evidence that their metabolic state is a key factor in determining function.

For metabolically active cells in liver, muscle, and adipose, metabolic indicators are integral to tissue function assessment. More broadly, analysis of cellular metabolism can reveal opportunities to tailor the culture environment to fit the tissue engineering objectives, for example by identifying metabolic pathways whose activities correlate with improved function (Sharma, 2011). Rational redesign of cellular metabolism, termed metabolic engineering, has been successfully used in the microbial cell engineering community to upgrade the catalytic properties (Wang, 2013; Shaw, 2008) or biosynthetic capabilities (Avalos, 2013; Smith, 2011; Huo, 2011) of various unicellular organisms. In comparison, cells relevant to tissue engineering and regenerative medicine applications have been examined to only a limited extent from a metabolic engineering perspective.

---

<sup>1</sup> Sims JK, Manteiga S, Lee K. Towards High Resolution Analysis of Metabolic Flux in Cells and Tissues. *Curr Opin Biotechnol.* 2013, 24: 933-939.

Fortunately, many of the methods developed to analyze microbial metabolism can be readily adopted to study tissue metabolism, as the main pathways for extracting energy and generating building block biomolecules are highly conserved across organisms (Peregrin-Alvarez, 2009). One qualification is that cells of differentiated tissue require rich media with more than one carbon source. This adds complexity (Orman, 2011), in terms of both the number of metabolites that need to be monitored and the mathematical models that need to be formulated/solved to interpret the measurements. Another important qualification is that metabolic studies on microbes have typically assumed that the system of interest is homogeneous, or that characterization of bulk behavior is satisfactory.

In the case of tissue systems, which often comprise a heterogeneous population of cells, it can be desirable to obtain spatially and/or temporally resolved information. Spatial heterogeneity in metabolic state could reflect the presence of nutrient or signaling gradients, which are nearly always present in an avascular system due to mass transfer limitations. Spatial heterogeneity is sometimes an inherent feature representing physiological or pathological variations such as tissue zonation (Allen, 2003; Davidson, 2012) or tumor microenvironments (Konig, 2013; Xu, 2013). Temporal heterogeneity can arise as cells respond to hormones and other stimuli to engage and disengage different metabolic pathways. Terminal changes in metabolic phenotypes can occur over longer time periods, as illustrated by stem cells exhibiting dramatic changes in their redox levels as they transition from a proliferative state to terminally differentiated state (Reid, 2013). Ideally, these types of heterogeneities are studied

using spatiotemporally resolved, noninvasive methods that enable repeated observations over time.

In this remainder of this section, we first provide an overview of the most commonly used methods for quantitative characterization of cellular metabolism, highlighting representative applications in systems that are relevant to tissue engineering and regenerative medicine. We then discuss emerging methods that could enable highly resolved analysis of cellular metabolism, and thus address the issues of heterogeneity outlined above.

### ***1.2.1 Methods for Quantitative Analysis of Metabolic Flux***

Metabolic flux, typically expressed as a rate per unit amount of cell or tissue, measures the degree of engagement of various metabolic pathways in the intact cell. Compared to gene expression level or enzyme amount, metabolic flux provides a more immediate description of cellular activity. In the absence of detailed knowledge of enzyme kinetics, which is rarely available, steady-state fluxes provide useful quantitative snapshots of cellular metabolism. In the context of engineering microbial cells, metabolic flux analysis is already an established methodology, and has been discussed extensively in a number of excellent reviews (Mueller, 2013; Dandekar, 2012). Broadly, there are three groups of methods: metabolic flux analysis, flux balance analysis (FBA), and isotopomer analysis. Metabolic flux analysis (MFA) refers to the quantification of intracellular reaction rates from measurements on the rates of uptake or output of major nutrients and metabolic products in conjunction with a stoichiometric model of the major metabolic pathways. Given sufficient measurements, the

intracellular reactions rates can be calculated from stoichiometric mass balances. The major limitations are that the measurement requirements can be high if broad coverage of metabolism is desired and that resolution is limited.

Flux balance analysis (Schilling, 1998) incorporates the stoichiometric mass balances as constraints into a linear programming framework to predict intracellular reaction rates when measurements are insufficient to completely determine the system. This method is especially useful for large-scale metabolic models, which cannot be fully constrained using measurements. The main limitation is that FBA depends on identifying one or more recognizable metabolic objectives for the system of interest, which is not always possible for mammalian cells. In the context of tissue engineering, FBA can be viewed as a valuable analysis and design tool to explore possible (e.g. genetic) modifications that could redirect metabolic resources for a desired engineering objective. An interesting variant is flux variability analysis (FVA), which estimates the possible ranges of reaction rates by iteratively maximizing and minimizing the flux through each reaction in the metabolic model, thereby exploring alternate metabolic states for a given set of uptake and output measurements (Yang, 2011; Mahadevan, 2003). A useful outcome of FVA is to discriminate between well and poorly constrained parts of the metabolic network, which can then be used to focus additional experiments to improve the resolution of specific pathways.

Isotopic labeling is the current gold standard for experimental resolution of metabolic fluxes. Isotopomer (isotopic isomer) analysis exploits asymmetries in atom transfers of enzymatic reactions to relate reaction fluxes in a cell to the



distribution of label from an input substrate (typically a  $^{13}\text{C}$  labeled sugar, amino acid, or fatty acid) to various metabolic pathway intermediates. The relationship between reaction fluxes and label distribution is defined by a mathematical model, which is usually solved computationally to obtain the flux estimates. A clear advantage of isotopomer analysis is that details such as exchange fluxes of reversible reactions can be quantified with good confidence. The drawbacks are that the computational, experimental, and analytical efforts can be substantial.

### ***1.2.2 Metabolic Flux Analysis of Mammalian Cells and Tissues***

There have been numerous metabolic studies on the liver, which performs catabolic and anabolic functions essential for whole body homeostasis, including fasting glucose production, ammonia clearance, and xenobiotic transformation. While the hepatocyte is the dominant parenchymal cell type, other cell types also contribute to the organ's metabolism. Therefore, MFA studies aimed at characterizing alterations in liver metabolism under different physiological (Orman, 2010) or pathological (Lee, 2003) conditions have often utilized *ex vivo* organ perfusion to isolate systemic influences while preserving the *in vivo* cell composition. Hepatocyte specific metabolism has been studied using cultures of established cell lines as well as primary cells from rodents, pigs and humans.

One of the most widely utilized cell lines is HepG2, which has been used to study the metabolic effects of various stresses such as fatty acid toxicity (Srivastava, 2008) and drug challenge (Niklas, 2009). The latter study is particularly interesting, as MFA revealed alterations in central metabolism, specifically TCA cycle flux, even for sub-toxic doses of drugs, suggesting that an

examination of metabolic fluxes could provide insights into more subtle impacts of a drug before onset of outright toxicity. Isotopic labeling experiments have long been used to measure metabolic flux in the liver, although historically this approach has focused on a small subset of reactions in central metabolism (Des Rosiers, 1991; Di Donato, 1993).

In recent years, technological advances in high-resolution tandem mass spectrometry (MS), paired with new methods for extracting positional labeling information (Ruhl, 2012) as well as developments in modeling isotopic label distribution in metabolic networks (Crown, 2012) have steadily improved both resolution and breadth to enable increasingly sophisticated and comprehensive flux quantification experiments. For example, utilizing transient label enrichment data can facilitate the analysis of pathways whose intermediates do not rapidly reach isotopic steady state (Jazmin, 2013). This approach was used to examine the effect of a statin drug on both cholesterol synthesis as well as central carbon metabolism in primary rat hepatocytes, confirming that the drug exerts only minor effects outside of its target pathway (Maier, 2009).

Similar to the liver, metabolic studies of muscle cells, notably cardiomyocytes, have centered on energy metabolism in the context of overall tissue function (Schroeder, 2009) and metabolic consequences of drug challenge (Strigun, 2012). In a recent study, Strigun et al. used  $^{13}\text{C}$  labeling experiments using a murine atrial cell line (HL-1) to examine the effects of verapamil, a calcium channel blocker used to treat hypertension, and found that the drug reduces flux through glycolysis while minimally affecting the TCA cycle,

suggesting a possible explanation for the drug's potential anti-cancer activity (Strigum, 2011).

For adipocytes, isotopic labeling experiments have been used to specifically interrogate lipid synthesis (Lligona-Trulla, 1997) and, in conjunction with MFA, to broadly profile the changes in central metabolism as the cells mature phenotypically through differentiation (Si, 2007). More recently, we have utilized MFA as a screening tool to identify and characterize enzyme targets for reducing lipid accumulation in adipocytes in the context of obesity (Si, 2009).

For neuronal cell types, a major focus has been on glutamate metabolism, due to the metabolite's central role as a neurotransmitter. *In vivo*, glucose is first converted to glutamine in astrocytes, and then taken up and hydrolyzed to glutamate in neurons (Lapidot, 1994). This compartmentalization presents a challenge for conventional MFA (Chatziioannou, 2003), which assumes that metabolite pools are homogeneous. Thus, isotopic labeling has been the method of choice. For *in vivo* studies, NMR spectroscopy has been particularly useful as a noninvasive analytical tool. In an earlier study, Shen et al. used this approach to estimate that glutamine/glutamate cycling rate is ~80% of glucose oxidation in resting human brains, confirming the quantitative importance of this metabolic cycle (Shen, 1999). *In vitro* studies where destructive sampling is an option have typically used MS to take advantage of increased sensitivity. Recently, Amaral et al. analyzed the dynamics of <sup>13</sup>C label enrichment in cell extracts collected over time to determine the quantitative significance of branched chain amino acid metabolism in cultured primary rat cortical astrocytes (Amaral, 2011).

In comparison to liver, muscle, and neuronal cells, relatively little is known regarding immune cell metabolism. The field of immunometabolism is relatively new, having emerged only a few years ago. However, the field has already proposed compelling hypotheses (Mathis, 2011) linking cellular energy metabolism to the regulation of immune cell phenotypes. Here, we focus on macrophages, although metabolism appears to play an important role in the functions of dendritic cells (Everts, 2012) and T-cells (Miccheli, 2006). For macrophages, it has been suggested that the metabolic state of the cell influences its activation state (Mantovani, 2013). A recent isotopic labeling study in cultured primary murine macrophages showed that activated macrophages exhibit a tumor cell-like tendency favoring glycolysis over oxidative metabolism (Rodriguez-Prados, 2010). Another intriguing observation was that classical (M1) activation led to a significant shift to glucose catabolism via glycolysis, whereas alternative activation had minimal impact. Such a metabolic “switch” has been also identified in the pentose phosphate pathway (PPP), where the switch can direct the cell towards M1 polarization by rebalancing the carbon fluxes through glycolysis and PPP (Haschemi, 2012).

### ***1.2.3 Genome-scale Metabolic Analysis***

Since the publication of the first genome-scale model of *Escherichia coli* MG1655 more than a decade ago (Edwards, 2000), a number of such models have been assembled for many industrially significant unicellular organisms, and used to characterize, design or optimize cellular metabolism, very often in conjunction with FBA or related constraint-based methods. In recent years, several models

reflecting a global reconstruction of enzyme-catalyzed pathways have also appeared for mammalian species, including humans (Thiele, 2013). A major challenge in the construction of tissue-specific models has been the need to manually curate the reconstruction based on literature reports due to the complexities arising from tissue-specific distribution of enzymes (Gille, 2010).

A notable example of a large-scale tissue-specific model is HepatoNet1, the first comprehensive reconstruction of human hepatocyte metabolism capable of simulating a large number of the liver's canonical metabolic functions (Gille, 2010). As a demonstration of potential utility, this model was used to identify metabolic enzymes that are essential to a pathogen, but nonessential to the liver, and thus targets for antibiotics, demonstrating an intriguing possibility to analyze tissue metabolism in the context of infectious disease studies. Another example is a model of human macrophage metabolism (Bordbar, 2012), which was recently used to show that oxidative phosphorylation is more important for alternative (M2) activation, whereas shuttling of glycolytic NADH from cytosol to mitochondria is more important for M1 activation, underscoring the quantitative role of metabolism in determining macrophage phenotype.

Beyond cell-type specific analysis, an exciting development in the use of genome-scale models has been to examine the integration of metabolism across multiple tissues in the body. For example, the HepatoNet1 model was combined with a physiologically based pharmacokinetic (PBPK) model to examine the consequences of perturbing specific enzymes in the liver on the metabolic profile of the whole body (Krauss, 2012). Using a related approach, Bordbar et al.

tailored a genome-scale reconstruction of human metabolism into cell-type specific models for adipocytes, hepatocytes and myocytes, which was then used to simulate several known metabolic cycles that integrate the different cell types (Bordbar, 2011). The integrated model predicted that alterations in metabolic gene expression in disease (e.g. obesity) lead to differentially active sets of reactions in these cycles, demonstrating potential uses for multi-tissue models in characterizing and understanding complex metabolic diseases. The predictions of these multi-scale FBA models remain to be experimentally validated, and would almost certainly benefit from the inclusion of other important cell types and regulatory (e.g. endocrine) mechanisms. In this regard, recent advances in micro-physiological lab-on-chip devices could offer timely opportunities to validate the multi-tissue models by isolating the interactions of selected cell types under controlled conditions.

#### ***1.2.4 Spatiotemporally Resolved Metabolic Analysis***

The metabolic analysis methods discussed thus far are inherently limited in their ability to address cellular heterogeneity. One way to address this limitation could be to measure isotopic enrichment of metabolites at the single cell level for calculation of metabolic fluxes. Single cell metabolomics is a relatively recent development (reviewed by Rubakhin, 2013)). To date, a majority of single cell metabolomics efforts have targeted unicellular organisms such as yeast (Ibanez, 2013) and simple algae (Amantonico, 2010), which exist in a population, but not bound cohesively as in tissue. Examples of animal cell studies involve zebra fish embryos (Hayashi, 2011) and mollusk neurons. In the latter study, capillary

electrophoresis coupled electrospray ionization MS was used to detect several hundred distinct metabolite signatures in individual neurons of a mollusk (Nemes, 2011). These studies demonstrate that metabolite detection at subcellular concentration is possible; however, challenges remain in isolating the cells and quantifying the metabolites (Rubakhin, 2011).

An obvious limitation of MS based single cell metabolomics is that the analysis of intracellular metabolites is destructive, thus precluding repeated observations over time on the same cell. An alternative is to utilize noninvasive imaging methods, which additionally offer the benefit of providing spatially resolved information. There are many established fluorescent chemical probes used to quantify metabolic flux through specific pathways, with earlier studies relying on non-metabolized analogs of native substrates. An interesting variation involves fluorescence generating reporter substrates competing with the native substrate of the target enzyme. Sames and coworkers, who have reported extensively on this approach, demonstrated that the synthetic chemical coumestrol selectively competes for human hydroxysteroid dehydrogenases of the aldo-keto reductase (AKR) superfamily, and thus can be used to infer the flux of enzymes that couple with AKRs (Rodriguez, 2010). In principle, this approach could be extended to other enzymes, provided that a fluorescence generating substrate with suitable affinity similar to the native substrate is available for the enzyme of interest.

Genetically encoded probes have only recently been to be utilized to directly measure metabolite fluxes. In pioneering work, Frommer and coworkers

developed a glucose sensor based on Förster Resonance Energy Transfer (FRET). The sensor comprised a glucose recognition element from a bacterial periplasmic glucose/galactose binding protein fused with a cyan version GFP (CFP) and a yellow version of GFP (YFP). Upon binding of a glucose molecule, the fusion protein undergoes a conformational change, leading to increased FRET when CFP is excited (Hou, 2011). More recently, a similarly constructed FRET sensor for lactate has also been described, and used to quantitatively compare lactate flux in primary and cancerous glial cells at a single cell resolution (Barros, 2013; San Martin, 2013).

While achieving impressive sensitivity without the use of exogenously introduced dyes, the genetically encoded FRET sensors present the drawback that they require at least one transfection step, which may introduce artifacts from uneven transfection efficacy. In this regard, an attractive option is to utilize methods that exploit the auto-fluorescence of endogenous metabolites. This advantage is especially important for applications involving three-dimensional (3D) systems, where uniform labeling or transfection is challenging. Well-known examples of auto-fluorescent metabolites are nicotinamide and flavin adenine dinucleotides, which emit fluorescence upon near infrared excitation. These cofactor metabolites participate ubiquitously in cellular metabolism, coordinating the regulation of virtually every major pathway. Ratios of these and related cofactors have been used as a measure of metabolic activity in numerous studies over the last several decades. With the advent of sophisticated imaging techniques such as two-photon excited fluorescence (TPEF) microscopy, it has now become



possible to image ratios of auto-fluorescent cofactors at substantial tissue depths. Very recently, Quinn et al. utilized TPEF microscopy to correlate a decrease in cellular redox with stem cell differentiation into adipocytes in a 3D vascularized human adipose construct, reporting time- and tissue depth-dependent differences in the redox ratio (Quinn, 2012).

### ***1.3 Thesis Outline***

#### ***Chapter 2***

We first identified several enzyme targets to reduce triglyceride accumulation. These targets were selected from each stage of TG synthesis: pyruvate carboxylase and isocitrate dehydrogenase from upstream synthesis, diacylglycerol acyltransferase from downstream synthesis, and perilipin and fat specific protein 27 from droplet stability. We evaluated TG accumulation after siRNA knockdown of each target and selected targets for further analysis.

#### ***Chapter 3***

In order to non-invasively monitor TG accumulation, we used light microscopy to capture images at different time points in adipocyte differentiation. We developed an algorithm to automatically detect lipid droplets in an image so that we can quantify lipid droplet number, size, distribution and total lipid content. Using this algorithm, we can better understand spatial heterogeneity in adipocyte differentiation.

## ***Chapter 4***

After identifying promising targets, we examined changes in metabolite profiles due to enzyme knockdown. Using LC-MS, we measured concentrations of metabolites in many different pathways: glycolysis, TCA cycle, amino acid metabolism, fatty acids and cofactors. We used principal component analysis and hierarchical clustering to understand differences between knockdown conditions and which metabolites contribute most strongly.

## ***Chapter 5***

We then combined knockdown of multiple targets (in multiple stages of TG synthesis, as well as multiple targets within the same stage) to examine the effects on TG accumulation and the overall metabolic network. In addition to metabolomic analysis, we conducted an isotopic labeling experiment to resolve the fluxes using a previously developed stoichiometric model.

## ***2 Identification of Enzyme Targets to Reduce Triglyceride Accumulation***

### ***2.1 Abstract***

We have previously assembled a three dimensional (3D) co-culture model of the adipose tissue using type I collagen gel as the scaffolding material. This co-culture significantly enhanced differentiation and lipid accumulation of adipocytes as well as proliferation and organization of endothelial cells (ECs) into a capillary-like network. The goal of the present study is to investigate reduction in TG accumulation and AD size via RNAi mediated gene silencing (siRNA knockdown) of metabolic proteins in both 3D and 2D culture.

Targets for siRNA knockdown were selected based on our knowledge of adipocyte metabolism. Metabolic proteins were identified from each stage of lipid accumulation: upstream synthesis (breakdown and transformation of glycolysis intermediates into precursors of fatty acid synthesis), downstream synthesis (formation of triglyceride from synthesized precursors), droplet stability (protection from intracellular lipases and formation of larger, more stable lipid droplets). Pyruvate carboxylase (PCX) and isocitrate dehydrogenase (IDH) were identified as targets for upstream synthesis, diglyceride acyltransferase (DGAT) for downstream synthesis, and fat-specific protein 27 (FSP) and perilipin (PLIN1) for droplet stability. To understand the efficacy of the lipofection in 3D culture, we characterized the effect of PLIN1 knockdown. Although, PLIN1 knockdown led to reduction in TG accumulation, gene expression data suggested that

knockdown was not sustained for the entire experiment, therefore, the remaining targets were examined in 2D mono-culture.

## **2.2 Introduction**

Previous work identified pyruvate as a key intermediate in adipocyte triglyceride (TG) accumulation (Si, 2009). Although pyruvate is involved in many pathways, including glycolysis, TCA cycle, and amino acid metabolism, upon differentiation, adipocytes increasingly utilize pyruvate for *de novo* fatty acid synthesis. The activities of enzymes involved in the fatty acid synthesis pathway increase up to 20-fold as undifferentiated 3T3-L1 cells differentiate into mature adipocytes (Freytag, 1980). One of the key enzymes involved is pyruvate carboxylase (PCX), which carboxylates pyruvate to form oxaloacetate (OAA). Inhibition of PCX by phenylacetate has been shown to reduce TG accumulation by up to 30% *in vitro*.

The present study builds on this previous finding to examine the effects of disrupting the activities of additional, multiple enzymes across a network of metabolic pathways centered on TG synthesis. We constructed a simplified model of TG synthesis, separated into multiple segments (Figure 2-1). The upstream segment involves the production of building blocks/precursors from intermediates of glycolysis and the TCA cycle. The key precursors are cytosolic acetyl-CoA and 3-glycerol-P, which are the building block for long-chain fatty acids and the alcohol backbone for esterification, respectively. The downstream segment comprises *de novo* biosynthesis of long-chain fatty acids and esterification into TG. The third segment of TG accumulation is the protection and stabilization of

intracellular LDs. Once TG is synthesized, it is localized in membrane-enclosed inclusion bodies, called lipid droplets (LDs), within the cell. These LDs are shielded from uncontrolled degradation by many LD-associated proteins. The pathways and enzymes identified in Figure 2-1 by no means represent an exhaustive list. Transcriptional (and post-transcriptional) regulation of the enzymes involved is critically important in the synthesis and mobilization of TG. For example, intracellular lipases, which are involved in the breakdown of TG, clearly contribute to the balance of TG and free (non-esterified) fatty acids, and could be additional targets to investigate. However, as quantitatively important lipases are regulated primarily via allosteric mechanisms that are difficult to disrupt selectively, we decided to focus on synthesis enzymes and stability-related proteins that can be selectively disrupted at the level of translation.

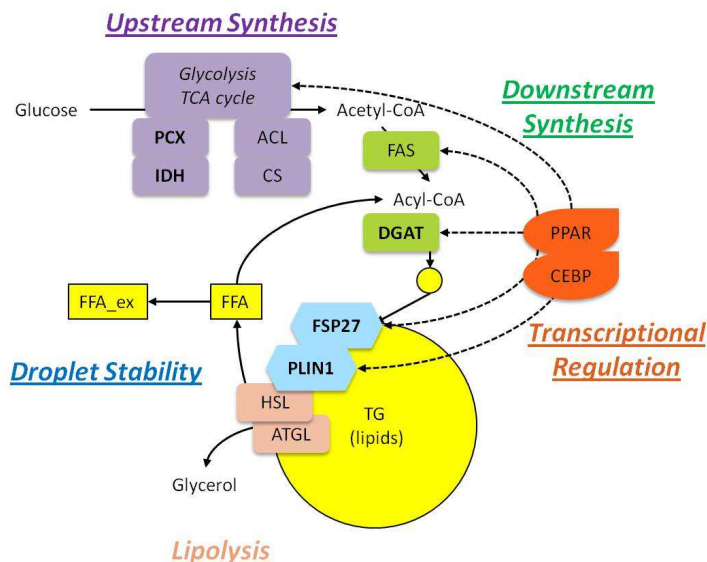


Figure 2-1: Triglyceride Accumulation Pathway

The triglyceride accumulation pathway is grouped into three segments: upstream synthesis (purple), downstream synthesis (green) and droplet stability (blue). Lipolysis (tan) is also an important factor affecting the intracellular TG level. Intracellular lipid droplets are represented as yellow circles. See Table 1 for more detailed list of these enzymes.

Table 1: Abridged List of Enzymes involved in TG Accumulation

<b>Enzyme</b>	<b>Abbr.</b>	<b>Reaction Catalyzed</b>	<b>Stage</b>
<b>Pyruvate Carboxylase</b>	<b>PCX</b>	Pyruvate → Oxaloacetate (mitochondria)	Early Synthesis
Pyruvate Dehydrogenase	PDC	Pyruvate → Acetyl-CoA	Early Synthesis
Citrate Synthase	CS	Oxaloacetate → Citrate (mitochondria)	Early Synthesis
ATP-Citrate Lyase	ACL	Citrate → Acetyl-CoA (cytosol)	Early Synthesis
<b>Isocitrate Dehydrogenase</b>	<b>IDH</b>	Isocitrate → 2-Oxoglutarate (cytosol)	Early Synthesis
Glycerol-3-P Dehydrogenase	GPDH	Dihydroxyacetone-P → Glycerol-3-P	Early Synthesis
Fatty Acid Synthase	FAS	Acetyl-CoA + Malonyl-CoA → Palmitate	Late Synthesis
<b>Diacylglycerol Acyltransferase</b>	<b>DGAT</b>	Diacylglycerol → Triglyceride	Late Synthesis
<b>Perilipin</b>	<b>PLIN1</b>	Coats lipid droplet, shields from lipase	Stability
<b>Fat Specific Protein 27</b>	<b>FSP27</b>	Promotes lipid droplet fusion	Stability
Hormone Sensitive Lipase	HSL	Hydrolyzes TG to fatty acids	Lipolysis
Adipose TG Lipase	ATGL	Hydrolyzes TG to fatty acids (committal step)	Lipolysis

Within each segment, we selected key protein targets for further examination. These targets are highlighted in bold in Table 1. As discussed previously, PCX catalyzes the carboxylation of pyruvate to oxaloacetate, which goes on to supply the carbons required to form fatty acids. Chemical inhibition of PCX has been shown to decrease TG accumulation in differentiated 3T3-L1 cells. Furthermore, PCX may also play a role in glyceroneogenesis that leads to the formation of the glycerol backbone in adipose tissue (Nye, 2008). PCX expression has been shown to be transcriptionally regulated by PPAR $\gamma$ , a key pro-adipogenic transcription factor (Jitrapakdee, 2005). Another target in early synthesis is isocitrate

dehydrogenase 1 (IDH), which catalyzes the oxidative decarboxylation of isocitrate to 2-oxoglutarate while reducing NADP<sup>+</sup> to NADPH. Although many intermediates of the TCA cycle are precursors for fatty acid and TG synthesis, the importance of IDH is the formation of NADPH, which is an essential cofactor in fatty acid synthesis (Koh, 2004). Cytosolic NADPH can also be produced by glucose-6-phosphate dehydrogenase, 6-phosphogluconate dehydrogenase, and malic enzyme; however, research has shown that IDH is a major producer of NADPH in lipogenic tissues (Koh, 2004). Overexpression of IDH positively correlates with adipogenesis in 3T3-L1s and transgenic mice with overexpressed IDH showed fatty liver, hyperlipidemia, and obesity. It is important to note that there is also a mitochondrial isozyme of IDH, which catalyzes the third step of the TCA cycle and also plays a role in reducing oxidative damage via glutathione metabolism.

Diacylglycerol transferase (DGAT) catalyzes the final reaction in TG synthesis, the covalent addition of a fatty acyl chain to diacylglycerol (Harris, 2011). This reaction takes place primarily in the endoplasmic reticulum; however, there is also evidence suggesting local synthesis on the surface of lipid droplets (Walther, 2012). There are two primary forms of DGAT, both of which are highly expressed in adipose tissue, as well as liver and other tissues. DGAT2-deficient mice typically do not survive, but DGAT1 deficiencies lead to a reduction in adipose mass and smaller adipocyte size (Chen, 2004). Therefore, DGAT1 could be a promising target for in vivo modulation of adipose tissue hypertrophy.

After synthesis, TG is typically sequestered in intracellular lipid droplets (LDs). While the mechanisms of droplet formation and enlargement are not fully understood, the current model of LD formation involves budding from the ER membrane to form an organelle that is bounded by a monolayer of phospholipids and LD-associated proteins (Martin, 2006). Among these associated proteins is perilipin (PLIN1), a member of the PAT family of proteins (perilipin, adipophilin and TIP47) (Brasaemie, 2007). PLIN1 localizes to the surface of LDs and protects them from lipolytic degradation. Interestingly, under lipolytic conditions, perilipin is phosphorylated and recruits HSL to the droplets. However, for the purposes of this study, we assume that PLIN1 is not phosphorylated, and thus protects LDs from lipolysis, given the fact that the cells are exposed to the anabolic hormone insulin, which stimulates glucose uptake and TG synthesis.

Another key stage of TG accumulation is the formation of larger lipid droplets. Typically, *in vivo*, almost the entire cytoplasm of adipocytes (in WAT) is occupied by a large, unilocular (single droplet) LD (Nishino, 2008), though the mechanism of large LD formation is still unclear. Fat-specific protein of 27 kDa (FSP27) is thought to promote the formation of unilocular LDs. FSP27 was first identified as a member of the CIDE family of proteins (Cell death-Inducing DNA fragmentation factor 45-like Effector), but was also found to be highly expressed in adipose tissue and upregulated during adipogenesis (Puri, 2007). FSP27 has been shown to promote fusion of small LDs, which reduces the amount of surface area available to lipolytic enzymes. Therefore, knockdown of FSP27 leads to



decreased droplet size and increased lipolysis, and is a promising target for therapeutic action.

In order to examine the effects of disrupting each target, we used RNA interference (RNAi) via siRNA. Previous studies primarily used chemical inhibition of enzymes; however, chemical inhibitors are rarely specific to one enzyme and often result in off target effects, which can confound the analysis. For example, oxamate can be used to inhibit lactate dehydrogenase (LDH), which reduces pyruvate to lactate. Oxamate is a structural analog of pyruvate that competitively inhibits LDH activity. However, oxamate might also inhibit other enzymes where pyruvate is a substrate (e.g. PCX) and it is thus difficult to isolate the effects to the target enzyme. Therefore, we chose siRNA to knock down selected targets based on this method's high degree of specificity.

*In vitro*, adipose tissue is typically studied using an immortalized cell line, 3T3-L1, which was isolated from mouse fibroblasts (Green, 1974). These cells have been shown to recapitulate most of the key features of adipogenesis *in vivo*, including morphological changes, expression of lipogenic enzymes, extensive lipid accumulation, etc (Rosen, 2000). Furthermore, transplantation studies confirm that preadipocyte cell lines represent faithful models for adipogenesis (MacDougald, 1995). The use of isolated preadipocytes is largely limited due to their decreased proliferative capacity and decline in differentiation potential during subculture (Feve, 2005). Typically, 3T3-L1 cells are grown and differentiated in planar culture (e.g. 12-well plates); however, previous work identified the effects of culture dimensionality on differentiation and TG

accumulation (Lai, 2009; Shi, 2010). Briefly, when embedded in a collagen matrix, the cells accumulate more TG, indicating a higher degree of differentiation. This is likely due to the cells' freedom to exhibit morphological changes (i.e. rounding and expansion as TG is accumulated), which better represents the cells' behavior *in vivo*. Furthermore, when endothelial cells were incorporated, the effects were compounded. Adipose tissue is highly vascularized, and the importance of intercellular interactions is becoming increasingly important to *in vitro* studies of adipocytes, and many other cell types. We have thus expanded on previous work to examine the effects of targeted enzyme knockdown in both 2D and 3D culture.

## ***2.3 Materials and Methods***

### ***2.3.1 Materials***

3T3-L1 cells were purchased from ATCC (Manassas, VA). Tissue culture reagents including Dulbecco's Modified Eagle's Medium (DMEM), calf serum (CS), fetal bovine serum (FBS), human insulin, and penicillin/streptomycin were purchased from Invitrogen (Carlsbad, CA). Unless otherwise noted, all other chemicals were purchased from Sigma (St. Louis, MO).

### ***2.3.2 Cell culture***

Low passage 3T3-L1 preadipocytes were seeded into 12 well plates at a concentration of  $2 \times 10^4$  cells/cm<sup>2</sup> and cultured in a humidified incubator at 37°C and 10% CO<sub>2</sub>. The cultures were expanded in a growth medium consisting of DMEM supplemented with 10% v/v CS, 100 units/mL penicillin, 100 µg/mL

streptomycin, and 2.5 µg/mL amphotericin. The growth medium was changed every 2-3 days until confluence was reached. Two days post-confluence (designated as day 0), the cells were induced to differentiate using an adipogenic cocktail (DM1: 1 µg/ml insulin, 0.5 mM isobutylmethylxanthine, 1 µM dexamethasone, and 2 nM triiodothyronine) added to a basal medium (DMEM with 10% FBS and penicillin/streptomycin/amphotericin). After 48 h, the first induction medium was replaced with a second induction medium (DM2) consisting of the basal adipocyte medium supplemented with only insulin (1 µg/ml). After another 48 h, DM2 was replaced with the adipocyte basal medium. On days 4, 8, and 14, images were recorded for three randomly selected wells, which were then sacrificed for enzymatic assays of total TG content.

### ***2.3.3 Three-Dimensional Co-culture***

Previous work has shown that adipocytes co-cultured in a 3D matrix with vascular endothelial cells exhibited greater metabolic activity and attained morphological parameters that more closely approached *in vivo* values (Lai, 2009). Therefore, preliminary knockdown experiments were conducted in 3D co-culture based on the rationale that effects on LD size should be more readily detectable in this more tissue-like setting. On day 3 post-induction in planar culture, 3T3-L1 preadipocytes were detached using trypsin-EDTA and resuspended in ice-cold collagen prepolymer solution (2 g/L) at a density of  $2 \times 10^6$  cells/mL. For co-culture, HUVECs separately expanded in tissue culture flasks were detached and mixed into the collagen solution at a ratio of 10:1 (adipocytes to endothelial cells) as previously described (Lai, 2009). This mixture was added

to each well (0.5 mL per well), and allowed to gel at 37°C. After 1 hour, 0.5 mL of basal medium was added on top of the collagen gels. After another 24 hours, the spent medium was replaced with fresh basal medium (day 4 post-induction). To enhance differentiation and mediate effects of detachment, the cells received another round of the adipogenic cocktail (DM1) for 48 hours, followed by insulin treatment (DM2) for 48 hours. On days 8 and 14, images were recorded for three wells, and gels were digested using a collagenase solution. The suspensions containing the liberated cells were then mixed with SDS buffer and sonicated to lyse the cells.

#### ***2.3.4 siRNA Transfection***

Beginning on day 4 post-induction, cells were transfected with siRNA at 30 nM. Lipofectamine 2000 (Invitrogen) was used as a transfection reagent based on the manufacturer's suggested protocol. Briefly, Lipofectamine and the target siRNA were combined in Opti-Mem reduced serum medium and incubated for 10 minutes at room temperature to allow the nucleic acids to complex with the liposomes. After replacing the insulin supplemented adipocyte medium (DM2) with the reduced medium containing the siRNA-lipid complexes, the cells were incubated as normal. Preliminary experiments using nonsense siRNA showed no signs of cytotoxicity. Knockdown was sustained by continuing the siRNA treatment every 48 hours for the remainder of culture. The siRNA sequences were optimized for target specificity based on Sigma's Rosetta predictions. The vendor did not provide the exact nucleotide sequences, but the approximate nucleotide positions on the target RNAs are known. The sequence locations for each target

are listed in Table 2. The nucleotide position is given relative to the beginning of the NCBI RefSeq sequence for the given target gene. All sequences are for the target enzyme in mice, because 3T3-L1 preadipocytes come from a murine source. As a control, cells were transfected with a nonsense siRNA sequence.

Table 2: siRNA sequences of target enzymes

<b>Enzyme Target</b>	<b>Sequence Start</b>	<b>Mission siRNA ID</b>
Diglyceride acyltransferase	660	SASI_Mm01_00165594
Fat specific protein – 27	1211	SASI_Mm01_00118727
Isocitrate dehydrogenase	432	SASI_Mm02_00306822
Perilipin	1206	SASI_Mm02_00307953
Pyruvate carboxylase	1047	SASI_Mm01_00196797

### ***2.3.5 Triglyceride accumulation and DNA content***

Triglyceride measurements were performed on cell lysates as described previously (Si, 2007). Briefly, cells were rinsed with warm 1× PBS after aspirating the medium, and lysed *in situ* using a 0.1% SDS buffer followed by sonication. Free glycerol and TG were measured using an enzymatic assay kit from Sigma (catalog number TR0100). Data was normalized to the corresponding cell sample DNA content, which was determined with a fluorescence-based assay using the Hoescht dye.

### ***2.3.6 Real time RT-PCR***

Total RNA was isolated using the RNeasy Mini Kit from Qiagen (Valencia, CA). Reverse transcription was performed on a Stratagene MX 3000P qPCR (Qiagen), using high capacity RNA-to-cDNA kit (Applied Biosystems, Foster City, CA) and primers specific for perilipin and pyruvate carboxylase. mRNA and 18S rRNA levels were determined using the TaqMan gene expression assay. Gene

expression data was normalized to the 18S rRNA content in corresponding samples, and fold-changes with respect to untreated control were calculated using the normalized data.

### ***2.3.7 Microscopy and Manual Image Analysis***

Images were acquired using a Nikon Eclipse TE300 inverted microscope (Melville, NY), Orca-HR digital CCD camera and Simple PCI imaging software (HC Image/Hamamatsu, Sewickley, PA). At 200× total magnification, the image pixel to physical distance calibration was ~3 pixels/μm. For each condition, 10 images were randomly captured per well and manually analyzed. The diameter of every visible lipid droplet within an image was measured using ImageJ in order to calculate the average LD area and approximate size distribution.

## ***2.4 Results***

### ***2.4.1 Perilipin Knockdown Reduces TG Accumulation***

Preliminary experiments were conducted in 3D culture to determine the efficacy of siRNA-mediated knockdown. Perilipin was selected as the initial target due to its known role in LD stability. As expected, co-culture with HUVECs led to increased TG accumulation (Figure 2-2, open bars). Reduction of TG accumulation in monoculture (adipocytes only) was modest, but this reduction was significantly amplified in co-culture.

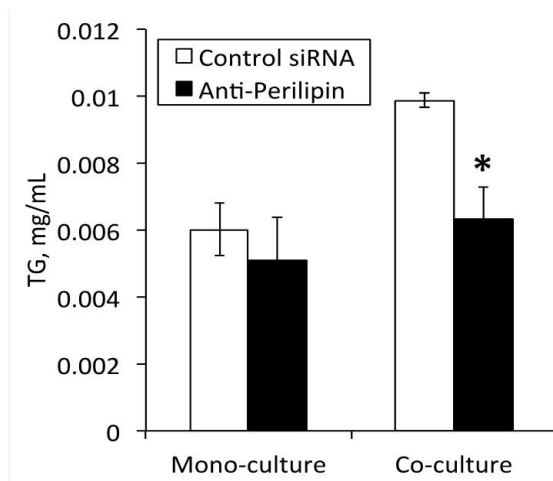


Figure 2-2: Triglyceride Accumulation in 3D Co-culture  
Open bars represent control (scrambled siRNA sequence) and close bars represent anti-perilipin siRNA. Error bars represent one standard deviation (n=3) and \*indicates statistically significant differences (p<0.05).

#### 2.4.2 Manual Image Analysis of Perilipin Knockdown

We manually analyzed images to investigate the effect of PLIN1 knockdown on average LD size and distribution. Compared to the monoculture, co-culture with HUVECs led to a ~100% increase in average droplet size (Figure 2-3, left panel, open bars). Similar to intracellular TG content, PLIN1 knockdown reduced the average size of LDs, with a greater effect observed in co-culture. In addition to a reduction in average droplet size, knockdown caused an apparent shift in LD size distribution towards droplets of smaller size.

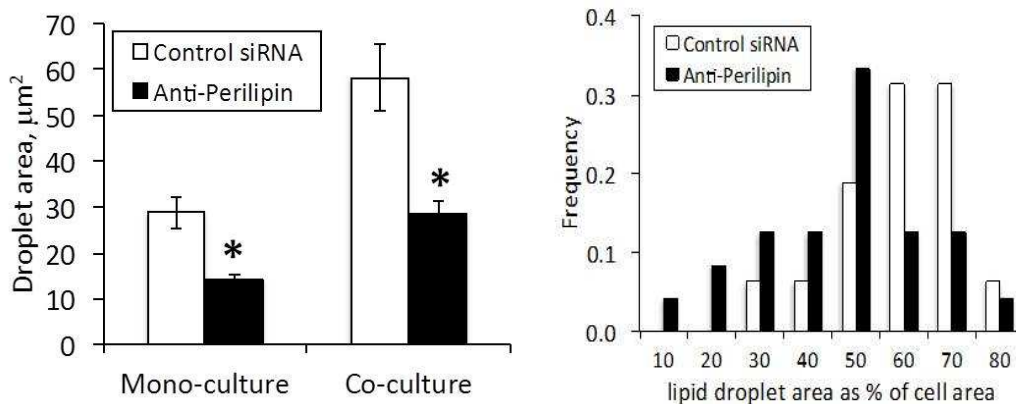


Figure 2-3: Manual Analysis of Adipocyte Images

Open bars represent control (scrambled siRNA sequence) and close bars represent anti-perilipin siRNA. Error bars represent one SD (n=10 images, ~100 droplets per image) and \* indicates statistically significant differences (p<0.05).

### 2.4.3 Gene Expression

In order to confirm knockdown, mRNA levels were analyzed for perilipin knockdown in 3D culture. 48 hours after the first treatment, mRNA levels were decreased significantly (Figure 2-4). However, perilipin mRNA expression steadily returned to normal over the course of the experiment, until day 10 when it reached the control level. This suggests that knockdown was not sustained for the entire time course of the experiment, which may be due to transport limitations of the siRNA-lipid complex through the collagen gel. Initial knockdown was achieved from the first treatment (when the cells were still in planar culture). Interestingly, even transient knockdown of perilipin led to significant changes in triglyceride accumulation (see next section). Based on these findings, we determined that the 3D culture system was not appropriate for knockdown experiments and performed the remainder of the knockdown experiments in 2D culture.

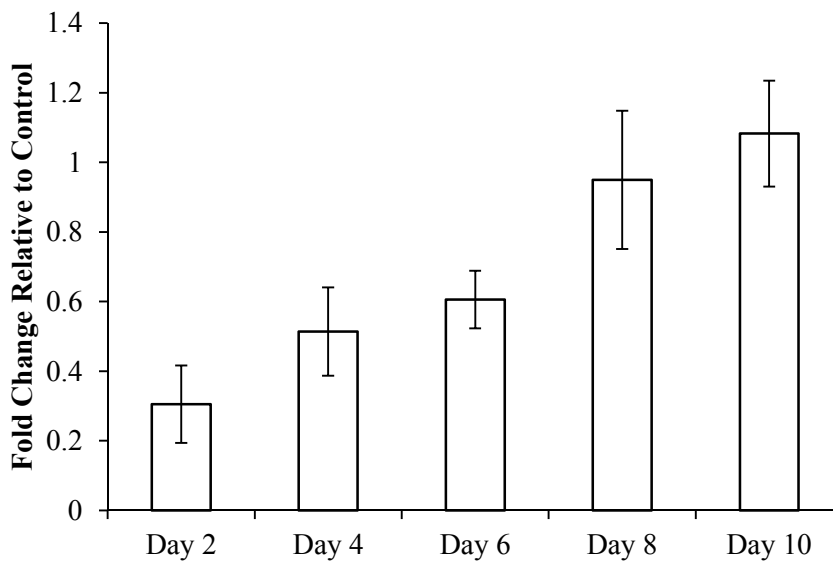


Figure 2-4: Perilipin mRNA Levels

Data was normalized to 18s rRNA of each sample, and reported as a fold change with respect to the untreated control for each time point.



#### 2.4.4 Targeted Knockdown Reduces TG Accumulation

After the preliminary experiments with perilipin, knockdown experiments of other metabolic targets were conducted in 2D mono-culture. As expected, knockdown of metabolic enzymes led to significant reduction in TG accumulation. On day 14, intracellular TG was reduced by as much as 30%. The largest difference was seen in pyruvate carboxylase knockdown, with smaller differences in the other conditions (Figure 2-5). There were no significant differences between the experimental conditions. siRNA treatment did not lead to cell death at any time point, as DNA content was relatively constant between replicates and experimental conditions (data not shown).

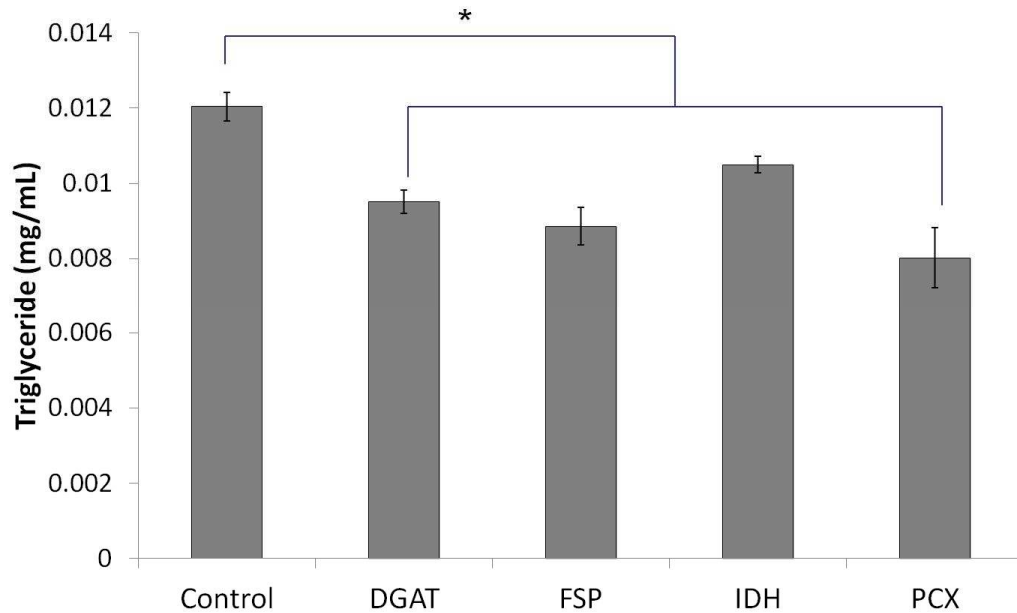


Figure 2-5: Triglyceride Accumulation in 2D Culture

On day 14, triglyceride concentration for each knockdown condition compared to the control. Error bars represent one standard deviation (n=3) and \* indicates significant difference ( $p < 0.05$ ).

## ***2.5 Discussion***

In this study, we explored potential enzyme targets across multiple pathways for reducing triglyceride accumulation. We selected targets from different pathways contributing to TG accumulation, with the ultimate goal of achieving greater TG reduction through coordinated knockdown of multiple enzyme/protein targets. siRNA was used to selectively knock down each enzyme, with little to no off-target effects. The first target we investigated was perilipin (PLIN1), a lipid droplet associated protein. Previous work in the literature showed that PLIN1 knockout reduced LD size, but there were conflicting results regarding reduction of TG. We confirmed a significant decrease in LD size, and a shift in the distribution as well (Figure 2-3). In monoculture, TG accumulation was reduced, but not significantly (Figure 2-2).

As previously reported, incorporation of endothelial cells significantly increased adipogenesis, leading to higher TG accumulation and larger LD size. Interestingly, PLIN1 knockdown had a more significant effect when analyzed in the co-culture system. Although the mechanisms are not fully understood, adipocytes and endothelial cells interact with each through secretion of soluble factors, as well as cell-to-cell contact. Due to the increased degree of adipogenesis in co-culture, we were able to observe a greater effect of knockdown. Furthermore, although PLIN1 knockdown would not have any direct effect on the growth and differentiation of ECs (as ECs do not express PLIN1), it is possible that knockdown impaired adipogenesis, causing reduction in the secretion of soluble factors by the ADs. Therefore, in the co-culture system, we may be observing compound effects of knockdown.

Unfortunately, mRNA levels of PLIN1 increased over the course of the experiment (Figure 2-4). This is likely due to transport issues of siRNA-lipid complexes through the collagen matrix; we estimated diffusion rates ~60-240 hours, based on the size of lipoparticles and porosity of the collagen matrix. The effective diffusion constant of lipoparticles is roughly 100 times greater than glucose and other small molecules. While metabolites are able to diffuse through the gel relatively quickly, lipoparticles do not reach the cells within an appreciable time frame. Despite this fact, we still observed a significant effect at the end of the experiment. It is likely that depressed mRNA levels early in the culture were sufficient to cause an effect, combined with the fact that expression of PLIN1 early in differentiation is also low. PLIN1 has a relatively long half-life (70h) (Koysan, 2007), so if expression was substantial at early time points, we might not have observed any effect at all. Although there are other transfection reagents and methods available, we decided to conduct future experiments in 2D monoculture to simplify the analysis, and ensure maximal knockdown of targets.

For each of the selected targets, we observed significant reduction in TG accumulation ranging from 20-40% (Figure 2-5). IDH knockdown had the least effect, followed by DGAT and FSP27, and PCX had the greatest effect. This likely reflects the respective methods of TG reduction. IDH knockdown causes a reduction in availability of NADPH, which would slow the synthesis of fatty acids. However, there are many pathways in the cell, which balance cofactor production. Furthermore, fatty acids can be taken up from the media as well, and a decrease in fatty acid synthesis could be mediated by increasing fatty acid

uptake rates. Similarly, PCX knockdown could reduce the availability of acetyl-CoA, a precursor for fatty acid synthesis; however, there are also several other pathways that produce acetyl-CoA. While PCX and IDH knockdowns both lead to reduced TG accumulation, it is possible that flux through these alternative pathways could increase to attenuate the effects of knockdown.

In contrast, there is one pathway that synthesizes TG, and the terminal enzyme is DGAT. In this study, DGAT knockdown did not result in total elimination of TG accumulation, due to the fact that DGAT expression may not have been knocked down completely, and other isoforms of the enzyme (notably DGAT2) are also expressed in the cell. Similarly, FSP27 is not the only LD associated protein. There are many other LD-associated proteins that affect LD stability (e.g. PLIN, adipophilin, S3-12, vimentin) (Brasaemie, 2004); however, without FSP27 to promote droplet fusion, LDs are more sensitive to lipolytic degradation. Although FSP27 does not directly reduce the amount of TG, it leads to an overall reduction in droplet size, and subsequent increase in total surface area. This increase in surface area provides greater access to lipases within the cell, and increased lipolysis.

### ***3 Image Processing Algorithm for Non-invasive Analysis of Lipid Droplets<sup>2</sup>***

#### ***3.1 Abstract***

Cellular hypertrophy of adipose tissue underlies many of the proposed pro-inflammatory mechanisms for obesity-related diseases. Adipose hypertrophy results from an accumulation of esterified lipids (triglycerides) into membrane-enclosed intracellular lipid droplets (LDs). The coupling between adipocyte metabolism and LD morphology could be exploited to investigate biochemical regulation of lipid pathways by monitoring the dynamics of LDs. This chapter describes an image processing method to identify LDs based on several distinctive optical and morphological characteristics of these cellular bodies as they appear under bright field (BF). The algorithm was developed against images of 3T3-L1 preadipocyte cultures induced to differentiate into adipocytes. We show that the calculated lipid volumes are in excellent agreement with enzymatic assay data on total intracellular triglyceride content. We also demonstrate that the image processing method can efficiently characterize the highly heterogeneous spatial distribution of LDs in a culture by showing that differentiation occurs in distinct clusters separated by regions of nearly undifferentiated cells. Prospectively, the LD detection method described in this work could be applied to time-lapse data collected with simple, visible light microscopy equipment to quantitatively investigate LD dynamics.

---

<sup>2</sup> Sims JK, Rohr B, Miller E, Lee K. Automated Image Processing for Spatially Resolved Analysis of Lipid Droplets in Cultured 3T3-L1 Adipocytes. *Tissue Eng Part C Methods*. 2014 Nov 12.

### ***3.2 Introduction***

Biochemically, adipocyte LD volume depends on the balance of synthesis and degradation of lipids. There is also a biophysical component, as the LDs are sequestered in a membrane-enclosed compartment that interacts with various components of the cytoskeleton through vesicle transport-associated proteins (Bostrom, 2007). How these different mechanisms interact to govern LD fate is an active area of research. To this end, methods are needed for monitoring the dynamics of LDs under controlled experimental conditions to quantitatively track the morphological changes in relation to cellular metabolism, signaling, and other biochemical processes.

Conventional methods used for LD analysis can be broadly categorized into enzymatic and dye-based assays. Enzymatic assays offer the benefit of absolute quantitation, but require the cells to be lysed, and are thus incompatible with live cell analysis. Moreover, information on size and spatial distribution of LDs cannot be obtained. An alternative approach is to stain the LDs with lipophilic dyes such as Oil Red O (ORO), which typically requires fixing the cells. The dye can be extracted with a solvent to quantify the amount bound to the cells, or the stained cells can be analyzed using microscopy, with the dye acting as a contrast agent for the LDs. Recently, Mehlem et al. presented a protocol that optimizes ORO staining for image analysis, and demonstrated that this protocol could be used to compare the differences in the tissue distribution of lipids in wild-type mice challenged with a high-fat diet (HFD) and transgenic (db/db) mice lacking leptin receptor activity (Ramirez-Zacarias, 1992). One limitation of using lipophilic dyes is that these dye also bind other lipids that are not associated with

intracellular LDs. Specificity can be improved by staining for LD-associated proteins, such as perilipin, adipose differentiation-related protein, and hormone-sensitive lipase, which co-localize to the surface of the droplets (Mehlem, 2013). On the other hand, this approach still requires fixing the cells, and thus cannot be used to observe dynamic behavior over time. Certain methods of fixing cells can deform and fuse the LDs, and thereby distort the analysis (Fukumoto, 2002).

Fixing the cells can be avoided by introducing labels, e.g. fatty acid analogs, which incorporate into native enzymatic pathways. For example, Kuerschner et al. added a fluorescent polyene-tagged lipid (*trans*-16:5 fatty acid) to the medium of cultured COS7 and 3T3-L1 cells to monitor the kinetics and spatial distribution of lipid flux (Kuerschhner, 2008). However, similar to lipophilic dyes, the polyene probes labeled not only LDs, but also other parts of the cell, including the ER. Moreover, fluorescent labeling of individual LDs occurred with very different kinetics, even for LDs of identical size, due to the rapid metabolism of the polyene, which may not reflect the native metabolism of naturally occurring lipids and thus confound the analysis.

In principle, one could avoid the use of synthetic dyes or exogenous labels by exploiting a distinctive optical or spectroscopic property of the LDs to image these intracellular objects. An attractive option is coherent anti-Stokes Raman scattering (CARS), which can be used to image lipids by tuning into the vibrational contrast of C-H bonds that are enriched in aliphatic molecules (Nan, 2003). An especially powerful feature of CARS microscopy is the ability to characterize the chemical composition of individual LDs, for example the degree

of unsaturation, based on stretching vibrations of C-C and C=C bonds (Nan, 2003; Rinia, 2008).

Another, simpler alternative is to utilize light microscopy. While spectroscopy-driven imaging methods offer superior specificity, these methods require more sophisticated instruments that may not be routinely available to many laboratories. The challenge in using light microscopy for extracting relevant LD parameters is that the images can be quite complex due to the heterogeneity in the size and distribution of the LDs, and distinguishing the LDs from other cellular objects is not trivial. In images acquired using bright-field (BF) microscopy, LDs generally appear as the brightest objects. This characteristic can be sufficient to identify LDs based on a simple threshold filter as long as the brightness differences between the LDs and other objects are relatively uniform. This filter can be readily implemented for automated analysis, as recently demonstrated by Or-Tzadikario et al. on images of cultured adipocytes treated with adipogenic or lipogenic factors (Or-Tzadikario, 2010). On the other hand, relying solely on a fixed brightness threshold can confound the analysis due to uneven contrast arising from various factors unrelated to LD morphology, such as variations in cell density, location within the well, and shadows caused by cellular debris. Furthermore, LDs of different sizes may appear brighter than others, and may skew the results of this analysis.

In the present study, we extend the algorithm for BF image analysis by incorporating additional features for LD identification with the goal of minimizing both false positives and negatives, while also improving the flexibility



to analyze a wide range of microscopy images acquired under different contrast and brightness settings. The algorithm recognizes LDs as objects that are (1) relatively light, (2) circular, and (3) surrounded by a relatively dark boundary, (4) which is also circular. In addition to manual analysis, we quantitatively compared the lipid volumes calculated from image analysis against enzymatic assay results, and found excellent agreement. Applied to images of cultured 3T3-L1 cells induced with an adipogenic cocktail, the image analysis showed that differentiation is highly heterogeneous in terms of spatial distribution with a culture well, occurring in distinct clusters separated by regions of nearly undifferentiated cells.

### ***3.3 Methods***

#### ***3.3.1 Materials***

3T3-L1 cells were purchased from ATCC (Manassas, VA). Tissue culture reagents including Dulbecco's Modified Eagle's Medium (DMEM), calf serum (CS), fetal bovine serum (FBS), human insulin, and penicillin/streptomycin were purchased from Invitrogen (Carlsbad, CA). Unless otherwise noted, all other chemicals were purchased from Sigma (St. Louis, MO).

#### ***3.3.2 Cell culture***

Low passage 3T3-L1 preadipocytes were seeded into 48 well plates at a concentration of  $2 \times 10^4$  cells/cm<sup>2</sup> and cultured in a humidified incubator at 37°C and 10% CO<sub>2</sub>. The cultures were expanded in a growth medium consisting of DMEM supplemented with CS (10 % v/v), penicillin, streptomycin, and

amphotericin. The growth medium was changed every 2-3 days until confluence was reached. Two days post-confluence (designated as day 0), the cells were induced to differentiate using an adipogenic cocktail (1  $\mu\text{g/ml}$  insulin, 0.5 mM isobutylmethylxanthine, 1  $\mu\text{M}$  dexamethasone, and 2 nM triiodothyronine) added to a basal medium (DMEM with 10 % FBS and penicillin/streptomycin/amphotericin). After 48 h, the first induction medium was replaced with a second induction medium consisting of the basal adipocyte medium supplemented with only insulin. After another 48 h, the second medium was replaced with the adipocyte basal medium. On days 4, 8, 12, and 16, images were recorded for six randomly selected wells, which were then sacrificed for enzymatic assays of total triglyceride (TG) content.

### **3.3.3 Enzymatic assay**

Triglyceride measurements were performed on cell lysates as described previously (Si, 2007). Briefly, cells were rinsed with warm 1 $\times$  PBS after aspirating the medium, and lysed *in situ* using a 0.1 % SDS buffer followed by sonication. Free glycerol and TG were measured using an enzymatic assay kit from Sigma (catalog number TR0100).

### **3.3.4 Microscopy**

Images were acquired using a Nikon Eclipse TE300 inverted microscope (Melville, NY), Orca-HR digital CCD camera and Simple PCI imaging software (HC Image/Hamamatsu, Sewickley, PA). The total area recorded per well was 0.44  $\text{mm}^2$ , which represents ~58 % of the available culture area. At 200 $\times$  total magnification (objective  $\times$  eyepiece), the image pixel to physical distance

calibration was  $\sim 3$  pixels/ $\mu\text{m}$ . The total number of images recorded was 300, representing an approximately square block of  $20 \times 15$  contiguous images inscribed in the center of each well. The images were captured using a semi-automated process, where one out of every 25 images was manually focused. Once an image was focused and captured, a  $5 \times 5$  block of images centered on the manually focused image was captured using programmed microscope stage motion (Prior Proscan, Rockland, MA). This process was repeated 12 times for each well, following a pattern of 4 rows and 3 columns. Using this process, the amount of time needed to image each well was  $\sim 7$  min. Images were acquired under three different modalities: BF, phase contrast (PC), and differential interference contrast (DIC). The algorithm was developed against the BF images. The PC and DIC images were used to evaluate whether the algorithm could also be used for images reflecting contrast generated due to differences in IOR or optical path length, respectively.

### ***3.3.5 Image Processing Overview***

The goal of image processing was to label each pixel in the raw gray-scale image as either part of an LD or not such that the processed image displays the location and size of the LDs as white pixels against a black background. The algorithm looks for objects in an image that have the following characteristics of LDs as they appear under BF microscopy: a circular shape with a dark boundary and light interior. While these characteristics are common to most cellular LDs, it is important to note that there were exceptions. In particular, depending on the contrast and brightness settings, the LDs in some images did not have an interior

region that was noticeably lighter than the background. Our processing algorithm takes into account this possibility by considering all three of the aforementioned LD characteristics.

The algorithm consists of the following six steps (Figure 3-1). First, the original gray-scale image is converted to a black and white (B/W) image using a “high” threshold value to isolate the light interiors of the LDs. In this image, objects that are lighter than the background pixels are labeled as white. Second, the original gray-scale image is converted to a B/W image using a “low” threshold value to identify the dark boundaries. In this image, only those regions that are surrounded by a very dark boundary are labeled as white. Third, these two B/W images are intersected to yield an image that is white only where there are objects that are both light and surrounded by a dark boundary.

Fourth, a circle finding step is applied to eliminate non-circular objects from this image. This step identifies circles based on the area to perimeter ratio, as a circle has the highest such ratio of any two-dimensional shapes. A second criterion is that a circular object should have boundary pixels that are equidistant (one radius away) from the object’s centroid. Fifth, the circle-finding step is applied to the low threshold image. Another filter is then applied to this image to evaluate each white-labeled object based on its solidity (defined as the fraction of an object’s convex hull that is occupied by the object) and the average pixel value of the corresponding region in the original gray-scale image. Sixth, the resulting image is combined with the intersected image (from step three) to yield the final processed image. All six steps of the processing algorithm were implemented in

MATLAB (MathWorks, Natick, MA) using a combination of custom code and built-in functions. Source code is available in Appendix A. The typical runtime for a stack of 300 images at  $1024 \times 1280$  pixel resolution was 1,500 sec.

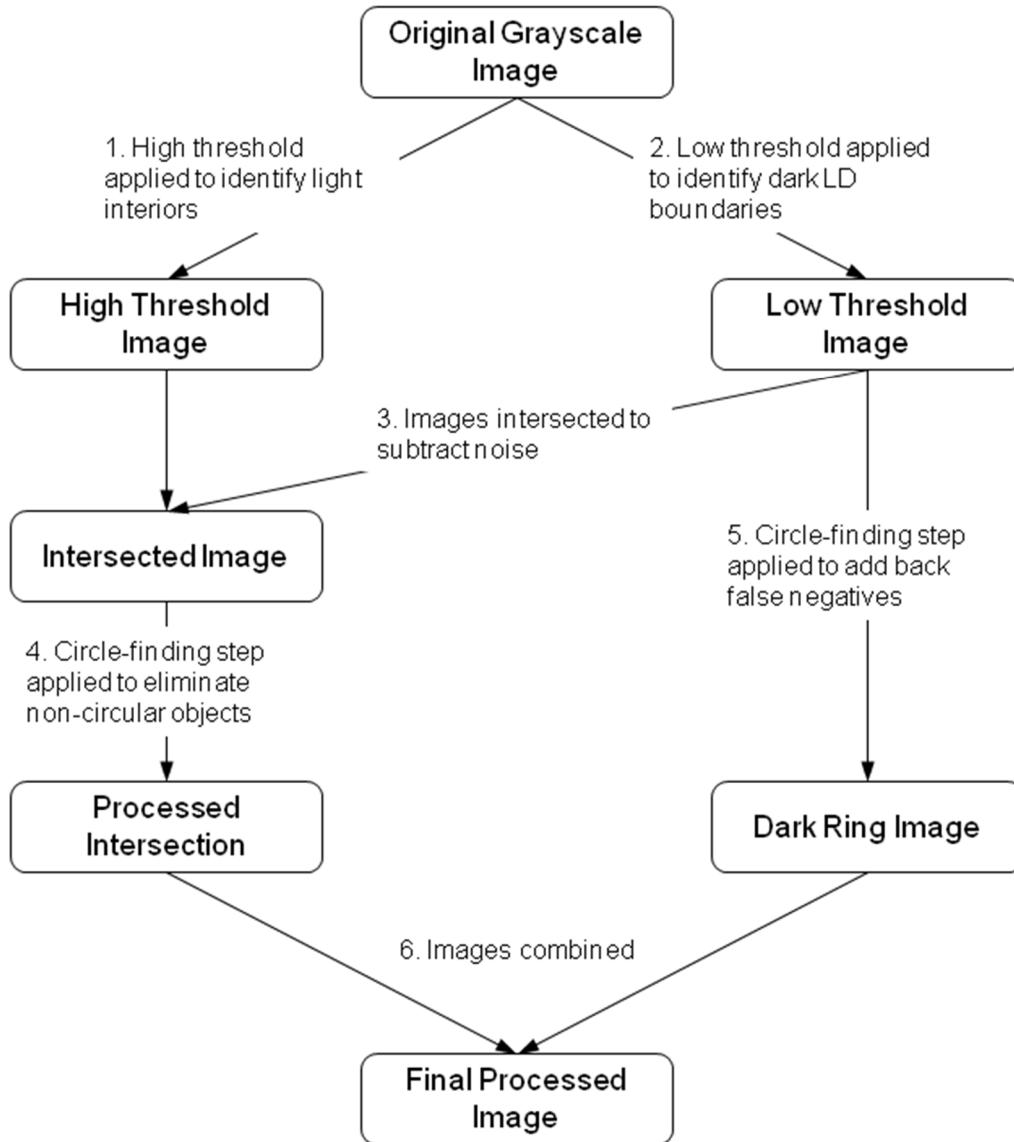


Figure 3-1: Overview of Image Processing Algorithm.

Boxes represent the image after each processing step, starting with the original grayscale image and ending with the final, processed image.

*Step 1: Black and White Conversion Using High-Threshold* - Each pixel in the original gray-scale image has a numerical value between zero (black) and one (white). To generate the “high” threshold B/W image, all pixels with values greater (lighter) than the threshold are set to white, and all pixels less (darker) than the threshold are set to black. Setting the threshold to an *a priori* fixed value, as was done in a previous work (Or-Tzadikario, 2010), was not desirable due to the possibility that overall brightness and contrast could vary between images. Therefore, the threshold was recomputed automatically for each image based on the pixel value distribution of the image using a built-in function of the Image Processing Toolbox in MATLAB. The function used Otsu’s method (Otsu, 1979) to choose a threshold value that minimizes the intra-class variance of the black and white pixels. We observed that the threshold chosen by the built-in function is usually close to the mean pixel value of the gray-scale image. Using the value returned by the built-in function led to B/W images that clearly included a substantial amount of background noise (Figure 3-2).

To better discriminate between LDs and other objects that appear lighter than the background, we compared the pixel value histogram of a representative image containing LDs to the histogram of an image from a culture that was not induced to differentiate and thus did not contain LDs. Based on the difference between these two histograms (Figure 3-3), we set the high threshold at a slightly larger value (15 % closer to white) than the value determined by Otsu’s method.

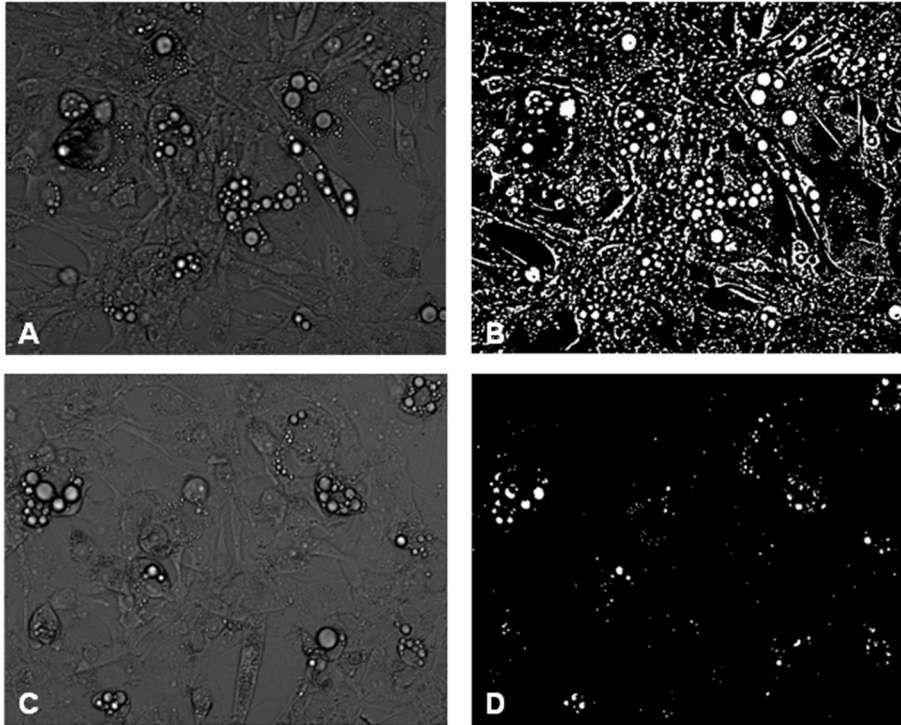


Figure 3-2: Representative Grayscale Images

(A, C) processed with a fixed threshold (B, D). (A, B) If the threshold is too high, most of the lipid droplets are included along with noise. (C, D) If the threshold is too low, many of the droplets may be missed.

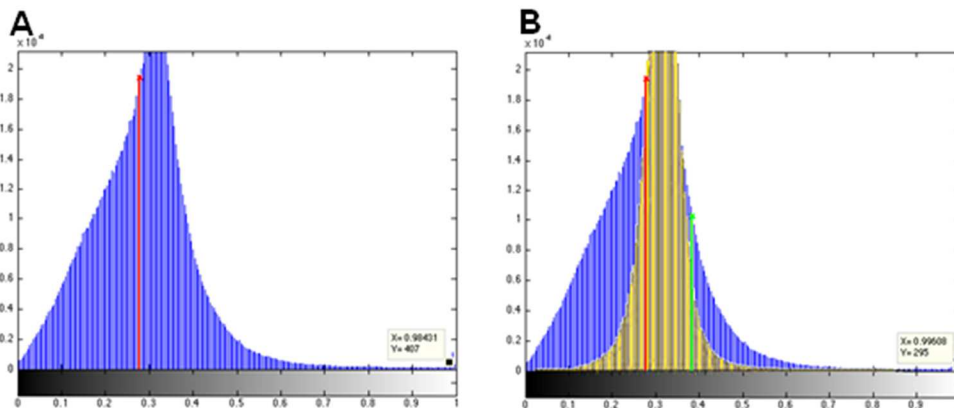


Figure 3-3: Pixel Histograms for Representative Images

(A) of cells containing LDs, shown in blue, and (B) overlaid with a histogram for a representative image of cells with no LDs shown in yellow. It can be seen in the overlaid image that the blue histogram includes a shoulder to the right of the average, indicating that images with differentiated cells contain a larger fraction of bright pixels (due to the interior of lipid droplets). The red line indicates the automatically determined threshold, and the green line indicates the “high threshold” set at a 15% higher value.

*Step 2: Black and White Conversion Using Low-Threshold* - The original gray-scale image was processed using an automatically computed “low” threshold to generate an image that identifies the dark rings surrounding the LDs. As was the case for the high-threshold value, the low-threshold value was determined based on a comparison of representative histograms from gray-scale images of differentiated and non-differentiated cultures. Using the threshold determined by Otsu’s method as a conveniently calculated reference, the low threshold was set at 90% of this reference value.

To identify white-labeled objects that are not associated with the dark rings and thus likely represent background, the area of every white object in the B/W low-threshold image was computed. Using a multiple of the largest LD size as a conservative cut-off, all objects larger than the cut-off were recorded as background. The low-threshold image was then inverted and then flood-filled, using the recorded object locations as seeds. The flood-filled image was then re-inverted to obtain an image (referred as the low-threshold image from hereon) where the white pixels represent the dark rings and enclosed areas, i.e. LDs, as well as residual noise representing background.

*Step 3: Intersecting the B/W Images* - In the high-threshold image, the white pixels represent objects that are lighter than the average background pixel in the gray-scale image, which include the LDs. In the low-threshold image, the white pixels represent the LDs and objects that are darker than the average pixel in the original image. By intersecting the high- and low-threshold images, a new image is generated where the white pixels correspond to pixels that were labeled white



in both images. The result is to eliminate most of the noise, i.e. background pixels falsely labeled as part of an LD, as these pixels cannot be simultaneously darker and lighter than the low- and high-thresholds, respectively, and thus do not overlap in the two images.

*Step 4: Identifying Circular Objects in the Intersected Image* - Much of the remaining noise (false positives) represents objects that are not circular, and thus unlikely to be an LD. Therefore, a circle-finding algorithm is applied to the intersected image from Step 3 to eliminate the non-circular objects. The circle-finding algorithm evaluates the circularity of each object in two ways. First, the algorithm calculates the area (A)-to-perimeter (P) ratio  $Z$ , which is maximal in two dimensions for a circle.

$$Z = \frac{4\pi A}{P^2} \quad (1)$$

Scaled by  $4\pi$ , this ratio ranges from zero for a line to one for a circle. The  $Z$  ratio, which is a measure of roundness, is easily computed for all objects in an image, but cannot distinguish smooth, oval-shaped objects (which probably are not LDs) from circular objects with irregular edges (which very well could be LDs). Therefore, another score is computed that determines how evenly distant an object's perimeter pixels are from the object's centroid. In a perfect circle, all boundary points are exactly one radius away from the center. After calculating the nominal radius ( $r_n$ ) of an object based on the object's area using the formula for a perfect circle, the actual radii ( $r_{a,i}$ ) of the boundary pixels are calculated from their coordinates and compared to the nominal radius. The differences between actual

and nominal radii are squared, normalized to the nominal radius, and averaged to compute a shape score S:

$$S = \sum_{i=1}^N \frac{1}{N} \frac{(r_n - r_{a,i})^2}{r_n^2} \quad (2)$$

To keep the computational time reasonable ( $< 10$  s), the number of boundary pixels analyzed for each image (N) was fixed at 32. The final circularity score was computed as a ratio of Z to S, such that an object that is more circular has a larger score. Based on the scores computed for representative LDs, the cut-off was set at 15, i.e. objects with circularity scores less than 15 were eliminated as potential LDs.

*Step 5: Identifying Solid Circular Objects in the Low-Threshold Image* - For large LDs ( $> 6\mu\text{m}$  in diameter), the presence of a dark ring around the droplet is a more reliable characteristic than the presence of a light interior. It is possible that intersecting the low- and high-threshold images will erroneously remove large LDs or underestimate the size of these LDs by only retaining the interior regions. To solve these “false negative” problems, the low-threshold image from step 2 is reprocessed to identify large, circular objects that should be restored in the final processed image. First, small objects were eliminated. Next, circularity scores are calculated for all remaining objects to identify likely LDs. As was the case for the earlier steps, the parameter values to determine smallness and circularity were chosen based on comparison with ground truth determined from visual inspection of the original BF images. A final filter is then applied to remove the remaining false positives (objects that are erroneously labeled as LDs) based on whether an

object is both solid and relatively light. Solidity is defined as the fraction of an object that is contained in its convex hull, and lightness is defined as the mean pixel value of the object normalized to the threshold computed by Otsu's method. The resulting image is referred to "dark ring image" from hereon.

*Step 6: Union of Intersected and Dark Ring Images* - The final processing step is to form the union of images resulting from steps 3 and 5. This final step restores several large LDs as well as boundaries eliminated during step 3.

### **3.3.6 Calculating LD Size, Volume, and Distribution**

The following statistics were calculated: number of LDs, fraction of image occupied by LD, average LD size, total LD volume, and a histogram of LD size distribution. All calculations were performed using the final processed image. The LD fraction was calculated by dividing the number of white pixels by the total number of pixels. Average LD size was calculated by dividing the number of white pixels by the number of distinct objects in the image. Total LD volume (in cubic pixels) was calculated by treating each object as a perfect sphere with a nominal radius estimated based on the object's area and the assumption that the area represents a circle defining the equator of the sphere. Size distributions based on LD volume were computed for each image as well as sets of images representing different time points in the differentiation experiment. As the number of small LDs ( $< 3 \mu\text{m}$  in diameter) was at least one order of magnitude greater than all other LDs, the bins of the histogram were determined based on the aggregate volume of the LDs in each bin, rather than number of LDs.

## **3.4 Results**

### **3.4.1 Comparison with ground truth**

A key desired feature for the image analysis algorithm is to process images that can be readily obtained using standard microscopy equipment without requiring the addition of fixatives, dyes and/or chemical probes. To this end, we developed the image analysis algorithm against micrographs of cultured 3T3-L1 adipocytes obtained under BF. Starting with a grayscale image (Figure 3-4A), the algorithm generates a high threshold image (Figure 3-4B) and a low threshold image (Figure 3-4C). The latter is inverted and flood-filled, then re-inverted to obtain a processed low threshold image (Figure 3-4D).

Intersecting the processed low and high threshold images eliminates much of the background noise (Figure 3-4E). However, some noise remains (boxed insert in Figure 2E), consisting of irregularly shaped objects that are falsely labeled as LDs. To remove these false positives, a circle finding step is applied. Figure 3-4F shows an image containing only the circular objects identified in the intersected image. Next, we identify larger solid objects from the processed low threshold image that should be retained as LDs (Figure 3-4G). The last step adds these circular objects to the intersected image (Figure 3-4F) to form the final image (Figure 3-4H). A comparison between Figure 3-4A and Figure 3-4H shows that the final processed image correctly identified nearly all of the LDs recognizable in the original grayscale image.

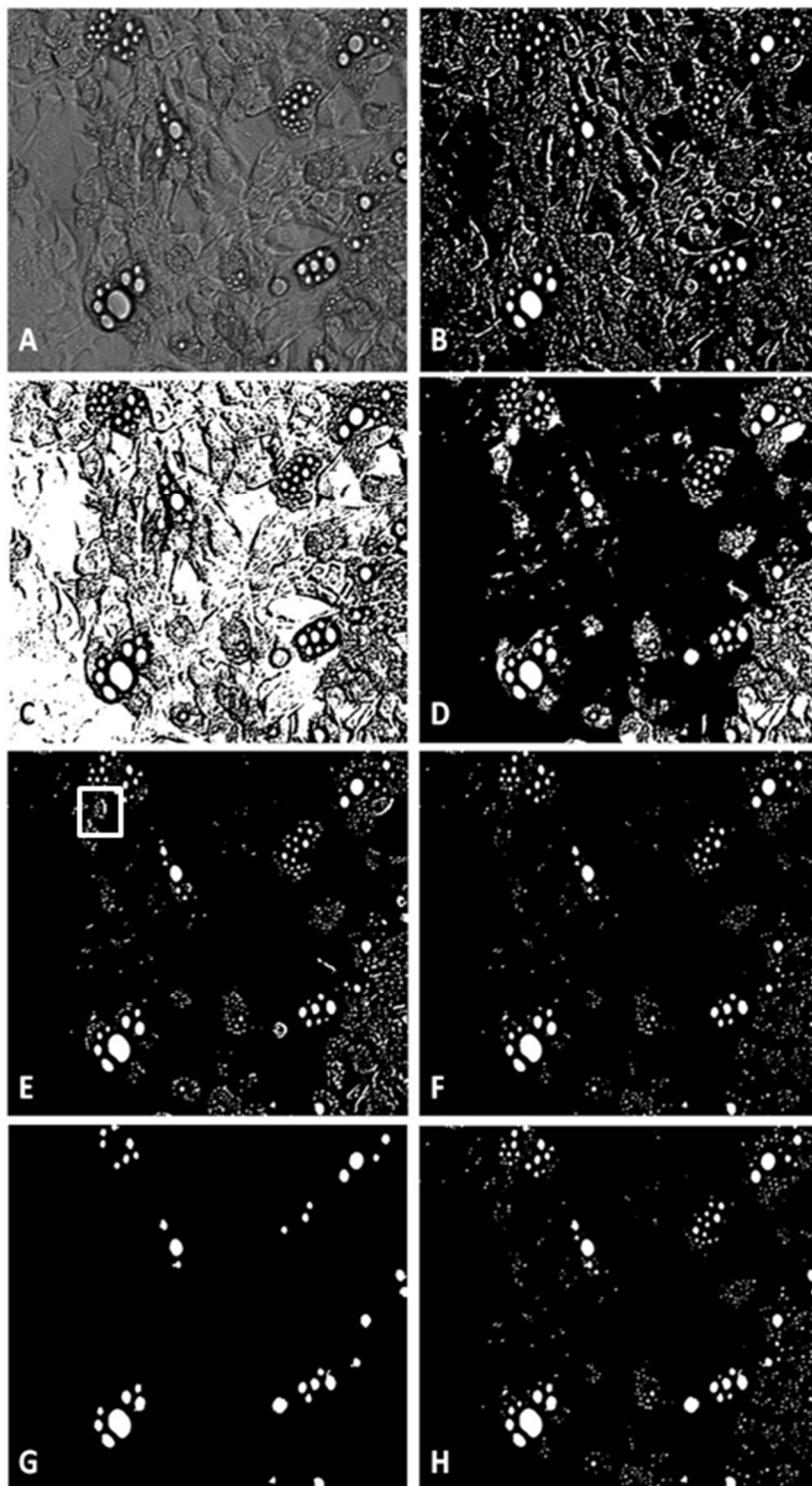


Figure 3-4: Illustration of Processing Steps

(A) Original grayscale, (B) high threshold, (C) low threshold, (D) processed low threshold, and (E) intersected images. (F) circular objects from the intersected image, (G) dark ring image, and (H) final processed image. Boxed insert shows irregularly shaped objects that are falsely labeled as LDs in (E).

### ***3.4.2 Comparison with biochemical data***

In this study, we used visual inspection to determine “ground truth,” i.e. whether an LD pixel was correctly labeled in the processed image. However, this determination can be prone to bias or user error. To obtain a more objective and quantitative assessment, we compared the calculated volume of LDs in a culture well against total TG content measured using an enzymatic assay on cell lysates. Over the course of a typical experiment, we noted that the extent of differentiation and lipid accumulation varied significantly from one region of a culture well to another. Consequently, it was possible that a small set of selected images may not be representative of the entire culture well.

For each well, we thus recorded a large contiguous ( $20 \times 15$ ) block of images covering approximately 58 % of the culture area. As shown in Figure 3-5, the calculated LD volume correlated linearly and very strongly with the corresponding TG data. Interestingly, the linear correlation was stronger ( $R^2 = 0.991$ ,  $p < 0.01$ ), when the data were averaged based on the time point ( $n = 6$  wells per time point). A well-by-well comparison of calculated LD volume and measured TG data (Figure 3-5A) showed a greater amount scatter ( $R^2 = 0.723$ ,  $p < 0.0001$ ), especially for wells corresponding to the later time points (days 12 and 16). The dominant source of scatter was the LD volume calculation, as the well-to-well variance in the enzymatically measured TG values was relatively small within a time point group (Figure 3-5B).

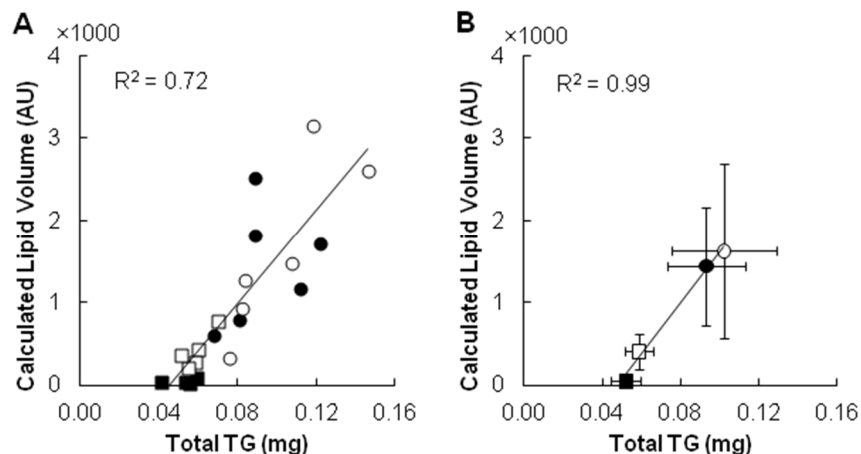


Figure 3-5: Calculated vs Enzymatically Measured TG content

(A) individual wells and (B) time point averages. Closed squares, open squares, closed circles, and open circles indicated, respectively, day 4, 8, 12, and 16 data. For the individual well comparison, matching images and enzymatic assay results were obtained on the same well. Error bars represent one SD ( $n = 6$  wells).

### 3.4.3 Culture heterogeneity

An important advantage of image analysis is the ability to obtain spatial information, which is impossible using destructive assays that require sample homogenization. To investigate the culture heterogeneity suggested by the sample scatter in Figure 3-5B, we mapped the distribution of LDs in a culture based on the calculated total LD volume for each image. The resulting heat maps (Figure 3-6) confirmed a highly heterogeneous distribution of LDs within a culture well. This trend was observed for all time points. To characterize the intra-well distribution of LDs, the pixel values in each heat map were scaled with respect to the image containing the largest amount of LD across all time points (set to white). We used a nonlinear (quadratic) scale for the purpose of visualization, as the gray colors resulting from linear scaling were difficult to distinguish from black. The scaled heat maps indicate that lipid accumulation, and presumably differentiation, occurs in clusters.

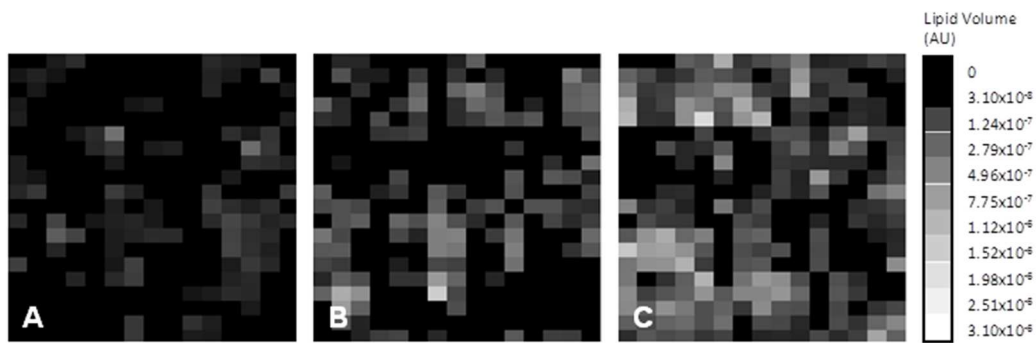


Figure 3-6: Heat Maps Showing Culture Heterogeneity

(A) day 8, (B) day 12, and (C) day 16. Each pixel represents a single image, with the intensity ranging from black (no lipid) to white (highest lipid content across all samples and time points). TG accumulation on day 4 is limited and not shown.

#### 3.4.4 *Size distribution of LDs*

In addition to spatial heterogeneity, image analysis can be used to characterize the size distribution of LDs. In one model of LD biogenesis, TG molecules ‘oil out’ between the leaflets of the bilayer membrane, initiating the formation of tiny primordial LDs (Pol, 2014). Once formed, the primordial LDs can fuse to form larger cytosolic LDs independent of TG synthesis, although it should be noted that the quantitative importance of fusion is subject to debate. Based on this model, we would expect to see a large number of LDs at early time points following adipogenic induction, with the number of LDs decreasing thereafter as smaller droplets fuse to form larger ones. This trend is indeed reflected in the data, with a steady increase in the number of LDs from day 4 to day 12, and a decrease on day 16 (Figure 3-7). An alternative model for LD biogenesis is the incorporation of locally synthesized TG molecules, which is supported by the presence of TG synthesis enzymes on the LD surface (Kuerschner, 2008). Both of these models imply that newly differentiated adipocytes will contain smaller LDs compared to mature adipocytes due to the time required to form larger LDs.



Comparing the size distributions of LDs on days 4, 8, 12 and 16, we found a steady increase in the fraction of large LDs with time post-induction (

Figure 3-8). On day 4, large LDs ( $> 11 \mu\text{m}$  in diameter, bins 10 and 11) contribute less than 20 % of the total lipid volume. In contrast, large LDs contribute more than 70 % of the lipid volume on day 16. Similarly, the contribution of the smallest droplets ( $< 4 \mu\text{m}$  in diameter, bin 1) to the total lipid volume steadily decreases from 47 % on day 4 to 5 % on day 16.

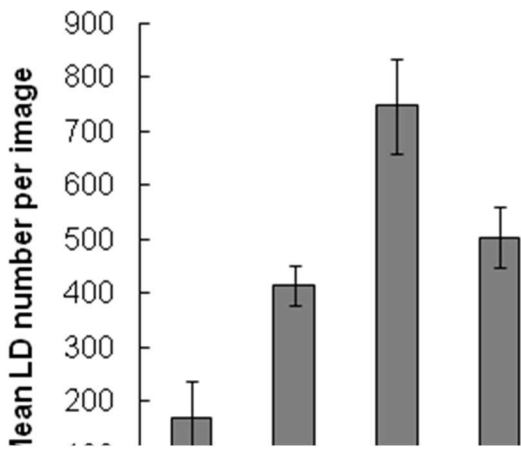


Figure 3-7: Average Number of Droplets per Image  
For each time point ( $n = 6$  wells). Error bars represent one standard deviation.

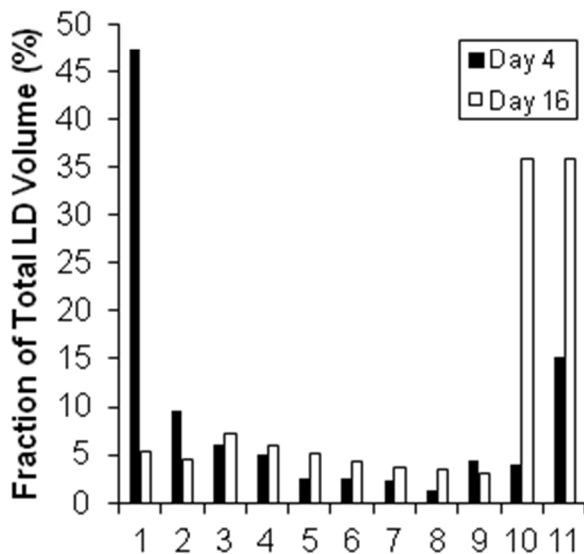


Figure 3-8: Droplet Size Distribution  
Day 4 (filled bars) and day 16 (open bars). Each droplet was binned according its contribution to the total lipid

volume of the corresponding image.

### 3.4.5 Comparison of Imaging Modalities

In addition to BF, PC and DIC microscopy have been commonly used to observe LDs. We thus investigated whether our processing algorithm could also analyze images captured using these two additional modalities. For comparisons, we recorded images of differentiating 3T3-L1 cells in the same field of view (comprising a 5×5 block of images) using all three (BF, PC, and DIC) modalities (Figure 3-9). The images were analyzed for total lipid volume, LD count, and LD size distribution, and the results from PC and DIC images were compared to the corresponding BF results.

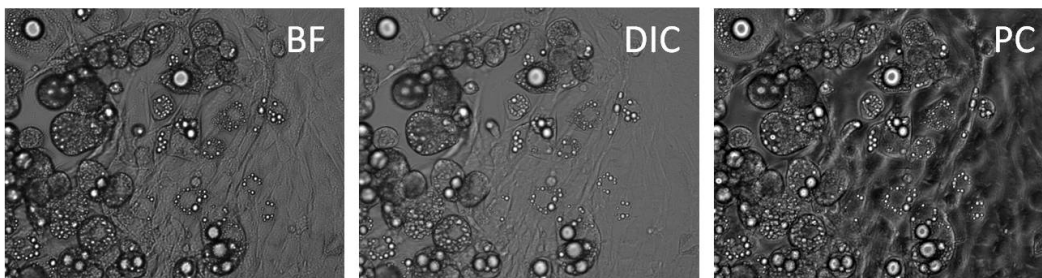


Figure 3-9: Representative Image Under Different Modalities  
Bright-field (BF), differential interference contrast (DIC), or phase contrast (PC) modality.

Overall, the DIC results correlated more strongly with the BF results than the PC results. For total lipid volume, the coefficient of determination ( $R^2$ ) for linear regression of DIC on BF was 0.82, whereas the  $R^2$  value for linear regression of PC on BF was only 0.55 (Figure 3-10). In both cases, total lipid volume was underreported relative to the BF analysis. The trend was similar for number of LDs, with linear regression of DIC and PC on BF yielding  $R^2$  values of 0.78 and 0.31, respectively (Figure 3-10). In contrast, we did not find any statistically significant differences (based on the two-sample Kolmogorov-Smirnov test) in the distribution of LD sizes calculated from BF, DIC, and PC images for any of

the four time points observed in this study (Figure 3-11). This finding, taken together with the observation that analysis of DIC or PC images tends to underestimate total lipid volume, suggests that the sizes of the LDs that the algorithm fails to detect in the DIC and PC images (but detects in the BF images) are likely randomly distributed; i.e. there is no clear bias for larger or smaller droplets.

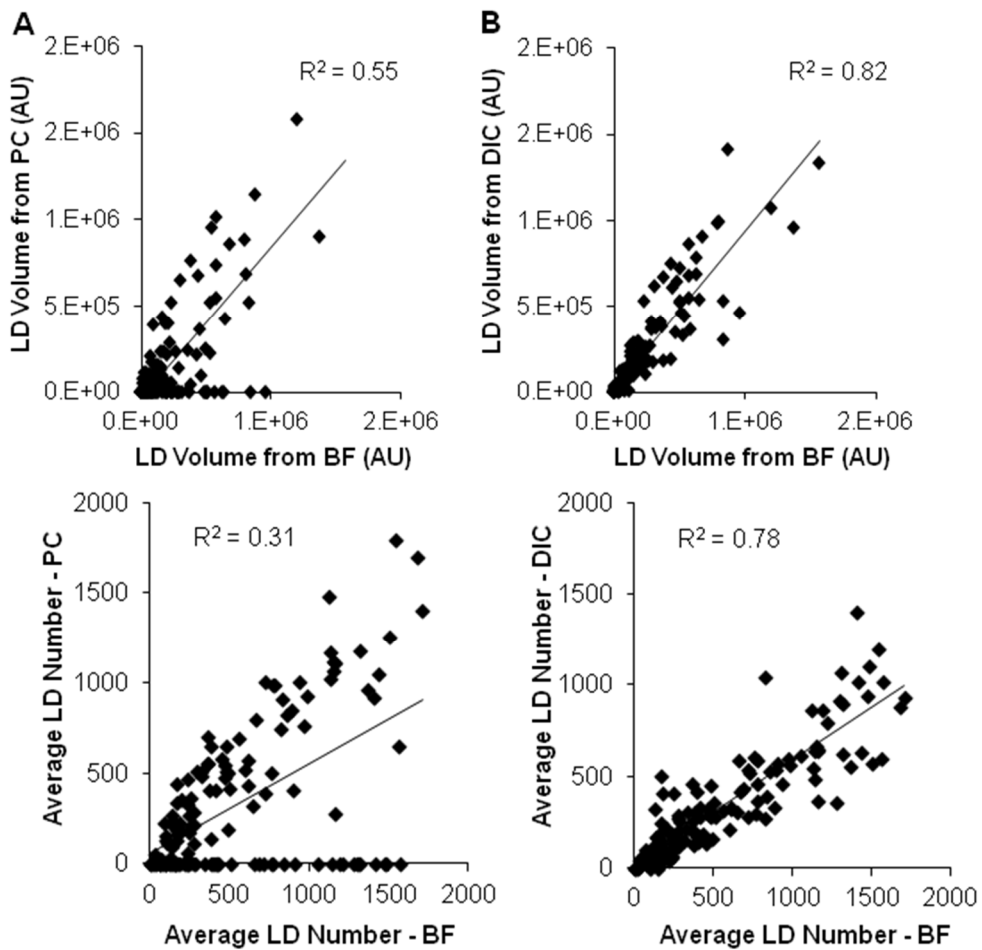


Figure 3-10: Comparison of Different Modalities

(A) PC and (B) DIC images compared to BF images. For LD volume, each data point represents a 5x5 block of images captured at different time points (day 4, 8, 12 and 16). For average LD number, each data point represents the average number of LDs calculated for a 5x5 block of images, captured at different time points (days 4, 8, 12, and 16). Averaging was performed by dividing the total number of LDs detected in the block by the number of images (25).

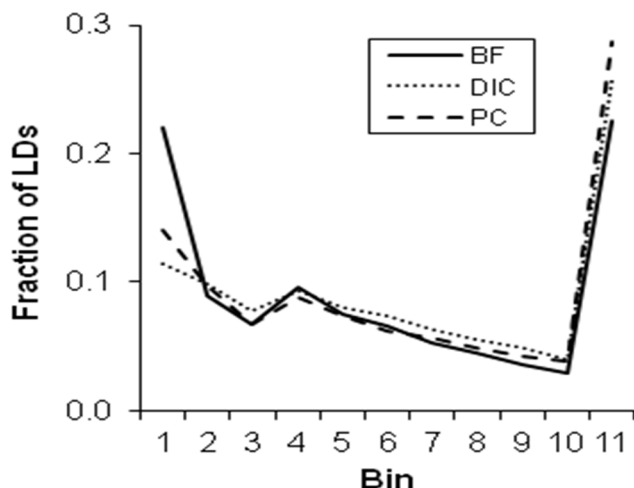


Figure 3-11: Droplet Size Distribution from BF, DIC and PC Images

Distributions were analyzed on images captured of the same cells in a 20×15 block of images. Data shown are for day 16. The analysis was performed for all time points. For each time point, the droplet size distribution was computed as follows. First, the number of LDs in each size bin was summed across all images. Then, the sum for each bin was divided with the total number of LDs across all bins to calculate the fraction of LDs in each bin. The BF, DIC, PC distributions were not found to be statistically significantly different based on the Kolmogorov-Smirnov test ( $p=0.01$ ).

### 3.5 Discussion

In this chapter, we present an automated image analysis algorithm that can be used with BF microscopy to accurately identify LDs in cultured adipocytes. Importantly, the images can be obtained using standard microscopy equipment, and the analysis does not require the cells to be fixed and/or labeled using a chemical probe. We develop the processing algorithm for images captured using BF microscopy, and show that we can obtain sufficient contrast even with this simple technique to robustly and accurately resolve LDs of varying sizes in cells at various stages of adipogenic differentiation.

An obvious benefit of automated analysis is efficiency, as manual analysis is time-consuming, especially if the images are heterogeneous and large numbers of

images need to be analyzed to obtain statistically robust results. Another benefit is consistency, as manual analysis of LDs can be error prone and biased. In certain cases, the designation of an object as an LD can be subjective, for example when only a part of an LD is visible due to spatial overlap with other LDs within a cell. Another potential source of error is the determination of LD boundaries, which is necessary to compute size. Due to practical issues such as focusing and microscope resolution, manual determination of an LD periphery may yield variable results, and thus significantly affect volume calculations.

Previous work on automated analysis of label-free images (Or-Tzadikario, 2010) relied on brightness contrast to identify LDs, with the implicit assumption that the LDs are the brightest objects in an image. In principle, this characteristic allows simple discrimination between LDs and other objects by applying a brightness threshold as a filter. However, this approach can become inadequate for complex images containing a heterogeneous distribution of non-uniformly differentiated cells with varying LD sizes. If the overall brightness of an image is too low, setting a fixed threshold can include many false positives due to background noise. Conversely, a fixed threshold could erroneously eliminate many actual LDs, if the brightness of an image is too low.

To address these issues, our algorithm utilizes two variable thresholds to exploit other characteristic features of LDs. Specifically, our method considers not only the lightness of an LD's interior, but also the darkness of the boundary and the circularity of both the LD and its boundary. By accounting for these multiple features, our algorithm can reproducibly process a variety of complex

images with different brightness and contrast to identify nearly all of the visible LDs while generating a very low number of false positives.

One particular challenge in both manual and automated analysis is the treatment of very small objects near the resolution limit of the microscopy instrument. In this study, we used a plan fluorite objective with a numerical aperture of 0.5 to acquire the images, yielding a resolution limit of approximately  $\sim 0.6 \mu\text{m}$  based on the Rayleigh criterion. In practice, we found that LDs with diameters less than  $1 \mu\text{m}$  were difficult to resolve, especially when juxtaposed with other similar sized objects. This difficulty was especially acute when identifying droplets manually, as it was practically impossible to consistently obtain an accurate measurement of a small LD's diameter. Even when the analysis utilizes image processing, the small LDs can be mistakenly eliminated as noise from the final processed image. Due to the limited resolution, we could not use the characteristic shape and contrast features of an LD to discriminate between true LDs and other objects.

On the other hand, these small droplets accounted for a very small fraction of the total LD volume in a given image. The volume fraction contributed by LDs with diameters  $< 4 \mu\text{m}$  was less than 1 % for images of newly differentiated adipocytes on day 4, the earliest time point where we observed microscopically visible intracellular LDs. This fraction was even smaller for images of the cells captured at subsequent time points. For these reasons, we tuned the algorithm's parameters (cutoff values for the low and high thresholds and circularity criteria) to focus on identifying the larger droplets that quantitatively determine the total

lipid volume. However, we also realized that larger lipid droplets are not as uniformly bright as small/medium droplets, therefore we tuned cutoff values for medium LDs and added the circle finding step for the low threshold image to make sure large LDs were not missed. For large lipid droplets, the interior will be less bright, and may be missed in the high threshold image. Furthermore, if the interior of a large LD is not uniformly bright, the portion that is included in the intersected image won't be circular. However, the dark ring is very circular, and will either add the object back to the processed image, or in the case of the test image, increase the size of LDs (and significantly add to the volume).

Overall, the results from automated image analysis correlated very well with the results from a standard enzymatic assay, especially across the different points along the differentiation time course (Figure 3-5B). We found that the correlation, while still significant, was weaker for individual culture wells (Figure 3-5A). The scatter in the data is likely due to the uneven nature of differentiation, both between wells and within an individual well. The heat maps of Figure 3-6 show that lipid accumulation is not uniformly distributed across the culture area in a well. Rather, lipid accumulation is quite heterogeneous and clusters into a few areas, presumably where differentiation has progressed to a greater extent compared to the rest of the culture. The uneven differentiation could explain the well-to-well variability in the image analysis data. If differentiation and lipid accumulation occurred uniformly, then every image would be equally representative of the entire culture regardless of the corresponding location of the image in the culture well. This is obviously not the case, and thus sampling



depends on both location of capture and number of images. For each well, the total area covered by the captured images represents approximately 58% of the available culture surface area, whereas the biochemical assay data was performed on homogenized cell extracts collected by processing the entire culture well.

Heterogeneity in the sizes and distribution of LDs in cultured adipocytes has long been recognized (Green, 1974). Loo et al. characterized this heterogeneity by examining LD morphologies and several key markers for adipogenesis in individual cells compared to population-averaged trends (Loo, 2009), and suggested that the heterogeneity reflects the presence of several subpopulations with distinct phenotypes. Using a single-cell approach, Le et al. found that the cell-to-cell phenotypic (non-mutative) variability in a clonal population of differentiating 3T3-L1 cells was not due to differences in the induction of adipogenic genes, as they observed that key regulatory genes such as PPAR $\gamma$  and C/EBP $\alpha$  were expressed in all cells. Rather, single-cell analysis of LD formation suggested that the variability was due to cell-to-cell differences in the kinetics of a signaling cascade that includes insulin sensitivity and glucose uptake (Le, 2009).

Still, this does not directly explain why adipocytes with microscopically visible LDs tend to differentiate in clusters within the culture well. One possible explanation is that the aforementioned kinetic variability between individual cells leads to different rates of LD formation early in the differentiation process, with the differences subsequently amplified via autocrine and paracrine signaling factors that are secreted by the differentiating adipocytes to promote the differentiation of neighboring cells. Enhanced differentiation of preadipocytes due

to the production of adipogenic factors by adipocytes has been reported in several *in vitro* studies involving conditioned media (Maumus, 2008), trans-well inserts (Stacey, 2009; Shillabeer, 1989), and microfluidic devices (Lai, 2012). However, the chemical identities of these adipocyte-derived factors and their effects of LD formation remain to be fully elucidated. In this regard, image analysis techniques that can characterize the time evolution of LDs in conjunction with live-cell microscopy should be useful in investigating the dynamics of LD formation in the context of local signaling between newly differentiated adipocytes and their neighboring cells.

In addition to obtaining spatially resolved information, another benefit of live-cell microscopy is the ability to repeatedly observe the same cells over time. In the present study, we used BF microscopy, which does not require fixing the cells and affords relatively rapid image capture, while still providing sufficient contrast to identify LDs. Employing the image processing algorithm presented in this chapter, we were able to detect the LDs without introducing dyes or probes, whose labeling kinetics could potentially confound the analysis when studying LD dynamics. Upon differentiation, adipocytes become relatively immotile, and the same cells can be readily monitored to estimate time constants for LD remodeling. For example, based on images recorded at 15 min intervals, we estimated that formation of small LDs (on the order of a few micrometers) occurs over several hours (Figure 3-12A), whereas further enlargement seems to occur over several days (Figure 3-12B). These estimates are consistent with a study by Nagayama et al., who manually analyzed time-lapse microscopy images to find

that nascent LDs form over several hours in primary stromal-vascular cells (SVCs) induced to differentiate into adipocytes (Nagayama, 2007).

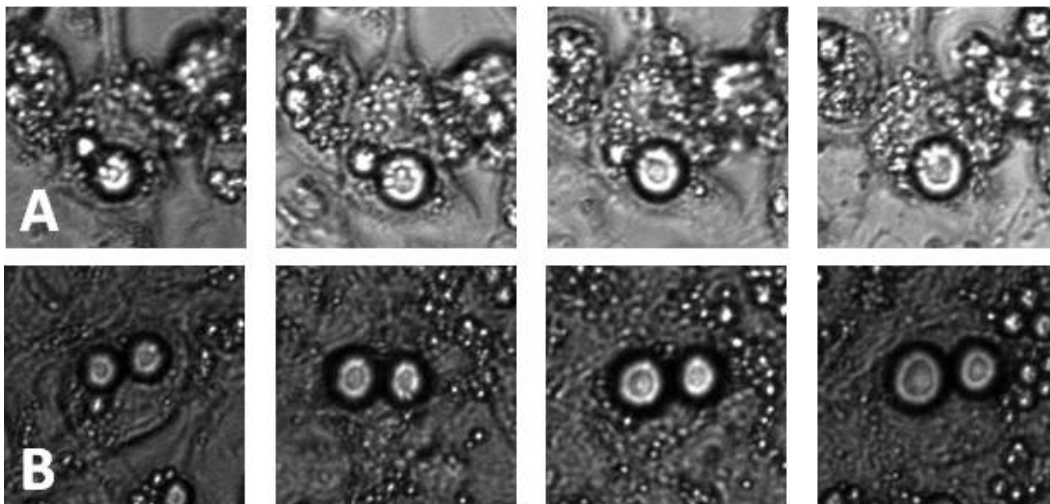


Figure 3-12: Representative Images Taken Over Time.

(A) Images were recorded for the same cell every 2 hours. (B) Images were recorded for the same cell every 48 hours. Images in (A) and (B) show different cells.

Clearly, the simplicity of the microscopy technique employed in the present study precludes finer analysis on the chemical composition of the LDs. Fine resolution chemical analysis can be performed with more advanced techniques that incorporate spectroscopy, notably CARS (Isomaki, 2014). However, these techniques require sophisticated equipment not readily available in most laboratories. For certain biological specimen, other light microscopy modalities such as PC and DIC have been shown to provide better resolution and contrast. Surprisingly, this was not the case for LDs in cultured adipocytes. Indeed, DIC images of LDs in adipocytes reported by several other groups (Nagayama, 2007; Wolins, 2005) appear quite similar to the BF images we recorded in the present study.

Consequently, we were able to use our image analysis algorithm to analyze LDs in DIC images without any parameter adjustments (

Figure 3-10B). On the whole, the algorithm performed relatively poorly on PC images, generally underestimating the number of LDs in an image. For selected PC images however, the results were nearly identical to the corresponding BF images (Figure 3-13). The number of LDs identified was 833, 268 and 1,153 for BF, DIC and PC images, respectively. Although many of the smaller droplets were missed in the DIC image, the total lipid volumes were comparable (972,000 for BF, 1,279,000 for DIC and 1,281,000 cubic pixels for PC). The distributions were not found to be statistically significantly different. These results suggest that the main limitation in extending the algorithm to PC images lies in the consistency of the image acquisition. PC images seem to be more sensitive to differences in focus level than BF or DIC images, indicating the combination of PC microscopy and semi-automated image acquisition involving intermittent focusing is not suitable for the feature-based LD identification processing described in the present study. This type of sensitivity to focusing was not as evident in the results of BF or DIC image analysis.

Taken together, our results suggest that automated detection of LDs can be applied to BF images for accurately estimating the lipid content and LD distribution of adipocyte cultures. The total LD volumes calculated using image processing correlated linearly with the amounts measured using a commercial enzymatic assay kit. In addition to offering an alternative to destructive assays for TG quantification, image analysis also affords spatially resolved analysis of LD

number and size distribution, which have been shown to directly vary with factors affecting cellular lipid metabolism, and thus could be used as readouts when testing agents designed to affect LD biogenesis or remodeling. For example, obese (fa/fa) Zucker rats fed a diet containing trans-10,cis-12 conjugated linoleic acid (CLA) showed increased glucose tolerance, reduced liver lipid content and reduced inflammation. Compared to Zucker rats fed a control diet, the livers of rats fed the diet containing trans-10,cis-12 CLA had a higher number of smaller LDs. *In vitro* experiments with cultured hepatocytes suggested that this anti-steatotic effect observed *in vivo* is due to influences of non-hepatic tissues, and likely involved increased utilization of lipids in WAT.

Smaller LDs expose a proportionately greater fraction of their lipid volume to degradation by hormone-sensitive lipase (Walther, 2009). Under lipolytic conditions, for example, induced by elevating cAMP via hormonal stimulation and consequent activation of protein kinase A, intracellular LDs transition from a clustered to dispersed state (Marcinkiewicz, 2006). This remodeling is thought to increase the total LD surface area within the cell and thereby accelerate lipolysis. As illustrated by hepatic steatosis, accumulation and mobilization of cellular LDs are not only important physiological processes, but also implicated in the pathophysiology of obesity and related diseases. In this light, methods that enable rapid, noninvasive, and spatially resolved analysis of LD dynamics should not only be useful in studying the biochemical and biophysical processes that govern cellular LD formation and morphology, but also in developing efficient screens for potential therapeutics that target LDs.

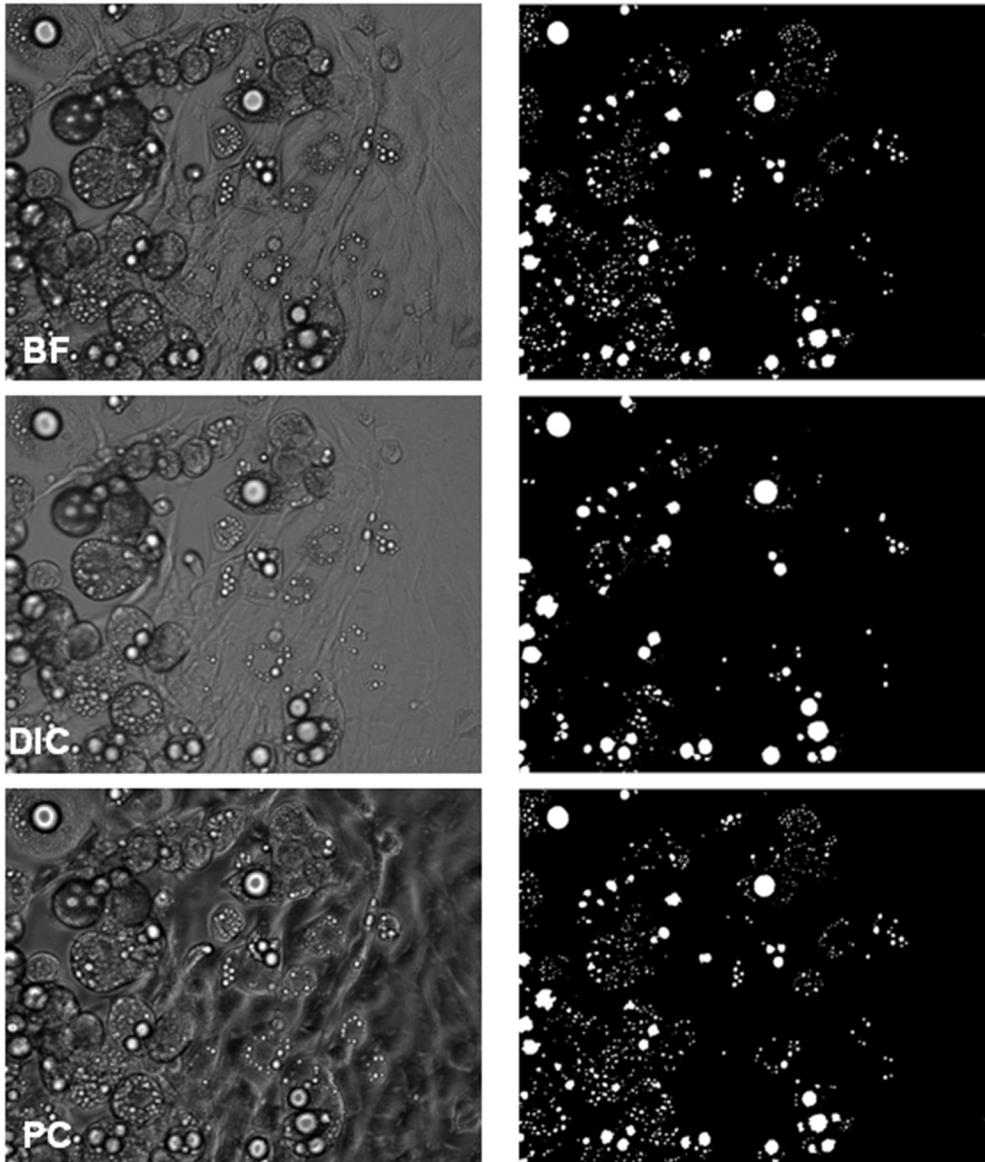


Figure 3-13: Representative Set of Processed BF, DIC, and PC Images  
These images were captured from the same location in the well (at the same time)  
under different microscopy modalities.  
Left column: unprocessed grayscale image; right column: processed image.

## ***4 Analysis of Network-wide Effects of Individual Enzyme Knockdown***

### ***4.1 Abstract***

Based on the results from Chapter 2, we selected the following targets for further analysis: pyruvate carboxylase (PCX), isocitrate dehydrogenase (IDH), diacylglycerol acyltransferase (DGAT), and fat specific protein (FSP27). We used a targeted metabolomic approach to understand the effects of knockdown. Using LC-MS, we measured concentrations of metabolites in many different pathways: glycolysis, TCA cycle, amino acid metabolism, fatty acids and cofactors. Changes in intracellular metabolite concentrations were greater on day 8 than day 14, with the most noticeable differences in DGAT and FSP knockdown, which were also surprisingly similar to each other. Knockdown of FSP and DGAT led to increased concentration of TCA cycle intermediates, and decreased concentrations in glycolysis and amino acids. Knockdown of PCX led to increases in some amino acid concentrations, and decreased concentrations of saturated fatty acids, but had no significant effect on the TCA cycle. IDH knockdown reduced glycolytic intermediates as well.

We used principal component analysis and hierarchical clustering to understand differences between knockdown conditions. This analysis confirmed observations that DGAT and FSP clustered tightly together. PCX and IDH also clustered together, but not as strongly. These trends were consistent from day 8 to

day 14, though slightly weaker on day 14, confirming observations that metabolite differences were less significant later in the experiment.

## ***4.2 Introduction***

Based on previous experiments described in Chapter 2 of this thesis, we selected the following targets for further analysis: pyruvate carboxylase (PCX), isocitrate dehydrogenase (IDH), diacylglycerol acyltransferase (DGAT), and fat specific protein (FSP27). PCX and IDH produce intermediates required for TG synthesis, DGAT catalyzes the final reaction in TG synthesis, and FSP27 promotes fusion of the lipid droplets and thereby regulates lipolysis. The goal was to understand the metabolic basis underlying the TG reduction we observed by examining the network-wide effects of the targeted knockdowns. We utilized a metabolomics approach to broadly profile the major intermediates of energy and lipid pathways in adipocytes.

Metabolomics is a growing field that applies a systems view to study the metabolic state of a biological system. Analogous to genomics, transcriptomics, and proteomics, metabolomics is concerned with obtaining a comprehensive picture of cellular physiology (Matilla, 2008). Of particular interest for adipose tissue biology has been lipidomics, which focuses on quantifying fatty acids, acylglycerols, phospholipids and other lipid species (Griffin, 2006). Pioneering studies in the field have highlighted the potential for lipidomics to enable simultaneous investigation of the multiple biological roles of lipid molecules as metabolic substrates, signaling intermediates, and structural components such as membranes of subcellular compartments (Manteiga, 2013; Choi, 2004). Recently,



lipidomics has been used to identify metabolic indicators of adipose tissue response to therapeutic intervention. In a study on the effects of rosiglitazone on lipid metabolism in diabetic mice, Watkins *et al.* identified palmitoleate (16:1n7) as an indicator of increased *de novo* FA synthesis in AT (Newton, 2011). More recently, Cao *et al.* found that palmitoleate is produced during *de novo* lipogenesis in AT, and that its production significantly correlates with improved insulin sensitivity (Wilson-Fritch, 2004). These findings are supported by studies in HSL-null mice, whose TG stores in AT depots contain significantly less palmitoleate (Foster, 2005). The proportion of palmitoleic acid was found to increase in obese, but otherwise healthy humans, suggesting that the production of this fatty acid could reflect an adaptation to restore insulin sensitivity (Bouwman, 2004). Notably, palmitoleic acid production was not increased in morbidly obese subjects.

In the present study, we utilized metabolomics to characterize not only the metabolites of lipid pathways, but also the intermediates of other major metabolic pathways that collectively govern the balance of intracellular TG in adipocytes. We developed and employed a series of liquid chromatography-mass spectrometry (LC-MS) methods to measure a broad range of intracellular metabolites and extracellular fluxes. Specifically, we profiled the following pathways and metabolites: amino acid metabolism and exchange rates, fatty acid profiles (both unsaturated and saturated), intermediates of glycolysis and the TCA cycle, and cofactors (ATP, NADH, etc). We utilized targeted product scans to robustly identify the metabolites of interest based on fragmentation spectra.

### **4.3 Materials and Methods**

#### **4.3.1 Materials**

3T3-L1 cells were purchased from ATCC (Manassas, VA). Tissue culture reagents including Dulbecco's Modified Eagle's Medium (DMEM), calf serum (CS), fetal bovine serum (FBS), human insulin, and penicillin/streptomycin were purchased from Invitrogen (Carlsbad, CA). Unless otherwise noted, all other chemicals were purchased from Sigma (St. Louis, MO).

#### **4.3.2 Cell culture**

Low passage 3T3-L1 preadipocytes were seeded into 12 well plates at a concentration of  $2 \times 10^4$  cells/cm<sup>2</sup> and cultured in a humidified incubator at 37°C and 10% CO<sub>2</sub>. The cultures were expanded in a growth medium consisting of DMEM supplemented with 10% v/v CS, 100 units/mL penicillin, 100 µg/mL streptomycin, and 2.5 µg/mL amphotericin. The growth medium was changed every 2-3 days until confluence was reached. Two days post-confluence (designated as day 0), the cells were induced to differentiate using an adipogenic cocktail (DM1: 1 µg/ml insulin, 0.5 mM isobutylmethylxanthine, 1 µM dexamethasone, and 2 nM triiodothyronine) added to a basal medium (DMEM with 10% FBS and penicillin/streptomycin/amphotericin). After 48 h, the first induction medium was replaced with a second induction medium (DM2) consisting of the basal adipocyte medium supplemented with only insulin (1 µg/ml). After another 48 h, DM2 was replaced with the adipocyte basal medium. On days 4, 8, and 14, images were recorded for three randomly selected wells, which were then sacrificed for enzymatic assays of total TG content.

### ***4.3.3 siRNA Transfection***

Beginning on day 4 post-induction, cells were transfected with siRNA at 30 nM. Lipofectamine 2000 (Invitrogen) was used as a transfection reagent based on the manufacturer's suggested protocol. Briefly, Lipofectamine and the target siRNA were combined in Opti-Mem reduced serum medium and incubated for 10 minutes at room temperature to allow the nucleic acids to complex with the liposomes. After replacing the insulin supplemented adipocyte medium (DM2) with the reduced medium containing the siRNA-lipid complexes, the cells were incubated as normal. Preliminary experiments using nonsense siRNA showed no signs of cytotoxicity. Knockdown was sustained by continuing the siRNA treatment every 48 hours for the remainder of culture. The siRNA sequences were optimized for target specificity based on Sigma's Rosetta predictions. The vendor did not provide the exact nucleotide sequences, but the approximate nucleotide positions on the target RNAs are known. The sequence locations for each target are listed in Table 2. The nucleotide position is given relative to the beginning of the NCBI RefSeq sequence for the given target gene. All sequences are for the target enzyme in mice, because 3T3-L1 preadipocytes come from a murine source. As a control, cells were transfected with a nonsense siRNA sequence.

### ***4.3.4 Metabolite Extractions***

Because salt-based detergents (e.g. SDS) are not compatible with LCMS, cells were extracted using an organic solvent mixture, methanol/chloroform/water (48:48:4 v/v) as follows. On days 8 and 14, media was removed and collected for separate analysis. Cells were rinsed with ice cold PBS and 524  $\mu$ L of

methanol/water (91:9 v/v) was added to each well. Cells were detached from the well using manual scraping over ice and stored in a 1.5 mL eppendorf tube. 476 uL of chloroform was added to each tube to reach the final concentration. Chloroform degraded tissue culture plastic, and thus could not be added directly to the well. The extraction protocol was optimized by varying the solvent to cell ratio to ensure that the volume of methanol/water was sufficient to detach cells from the plate and extract the metabolites while not overly diluting the samples. After addition of chloroform, the samples were vortexed and freeze/thawed 3 times in liquid nitrogen in order to fully lyse the cells. In order to remove cell debris, samples were centrifuged at 10,000 rpm for 10 minutes, and dried using a speed-vac at room temperature. Samples were reconstituted in 100 uL methanol/water (50:50 v/v) and stored at -20 °C until further analysis. Extracellular media was centrifuged to remove cell debris and diluted 10x in HPLC-grade water.

#### **4.3.5 LC-MS**

We analyzed the metabolite concentrations using multiple reaction monitoring (MRM) experiments performed on a QTRAP 3200 triple quadrupole ion-trap mass spectrometer (Ab Sciex, Framingham, MA). Chromatographic separation was achieved using an Agilent 1200 liquid chromatography system (Agilent, Santa Clara, CA). Separate runs were conducted for amino acids, fatty acids, and TCA/glycolysis intermediates. A complete list of columns and solvents used for chromatographic separation is available in the Appendix B. Each metabolite was confirmed based on its MRM transition (precursor and product ion pairing), and

were quantified by integrating the ion chromatogram to obtain the corresponding area under the curve (AUC). The AUC for each metabolite was then normalized to the total ion count (TIC) of the corresponding sample. Metabolite identities were confirmed based on their unique fragmentation spectra. Metabolite extraction buffers were not compatible with the Hoechst dye assay, which prevented the use of DNA content for normalization. While the DNA contents were relatively constant across different biological replicates and treatment conditions, normalization by sample TIC proved more robust.

#### ***4.3.6 Principal Component Analysis and Hierarchical Clustering***

In order to understand the significance of metabolite observations, we conducted a principal component analysis (PCA), using normalized metabolite measurements as independent variables, and knockdown conditions as dependent variables. We performed the analysis for both time points (day 8 and 14) as well as on control groups across time points. The analysis was conducted using built-in functions in MATLAB's Statistics Toolbox (Version 7.9.0.529, R2009B, Mathworks, Natick, MA). In addition, we categorized interactions between metabolite changes using hierarchical clustering. This analysis also utilized the built-in function of the Statistics Toolbox in MATLAB.

## **4.4 Results**

### **4.4.1 Measured Metabolite Levels and Extracellular Fluxes**

In general, changes in intracellular metabolite concentrations were greater on day 8 than day 14, with the most noticeable differences in FSP and DGAT knockdowns (Table 3 in Appendix C). Interestingly, the effects of FSP and DGAT were very similar to each other, and very different from the other knockdown conditions. The effects of PCX and IDH were also similar to each other, but not to the same extent. Knockdown of FSP and DGAT led to increased concentration of TCA cycle intermediates, and decreased intermediates of glycolysis and amino acid metabolism. Knockdown of PCX led to increases in some amino acid concentrations, and had no significant effect on the TCA cycle. IDH knockdown reduced glycolytic intermediates as well. Overall, knockdown conditions had less significant effects on fatty acid levels, with the exception of linoleic acid, which was significantly reduced in FSP, DGAT and PCX knockdown. As expected, PCX knockdown reduced the concentrations of palmitic and stearic acid as well. On day 14, differences were less significant, but metabolite levels were generally lower when compared to control, suggesting an overall decrease in metabolic activity, without significant effects on specific pathways.

Overall, there were fewer significant differences in measured extracellular fluxes (Table 7). Knockdown of the target enzymes/proteins did not significantly affect glucose uptake on day 8, while reducing the uptake slightly on day 14. On average, amino acid exchange rates were quantitatively very small compared to

flux through glycolysis, and generally similar across the control and treatment conditions.

#### 4.4.2 *Principal Component Analysis*

We first examined the principal components across each time point. We found good separation between the time points, despite a high degree of scatter within each group (Figure 4-1). Day 4 showed the most variability between replicates, consistent with the morphological heterogeneity present in cultures differentiating preadipocytes. As differentiation progressed, biological replicates exhibited less scatter. The primary metabolites contributing to the separation included TG, several amino acids, citrate and fumarate (Figure 4-2).

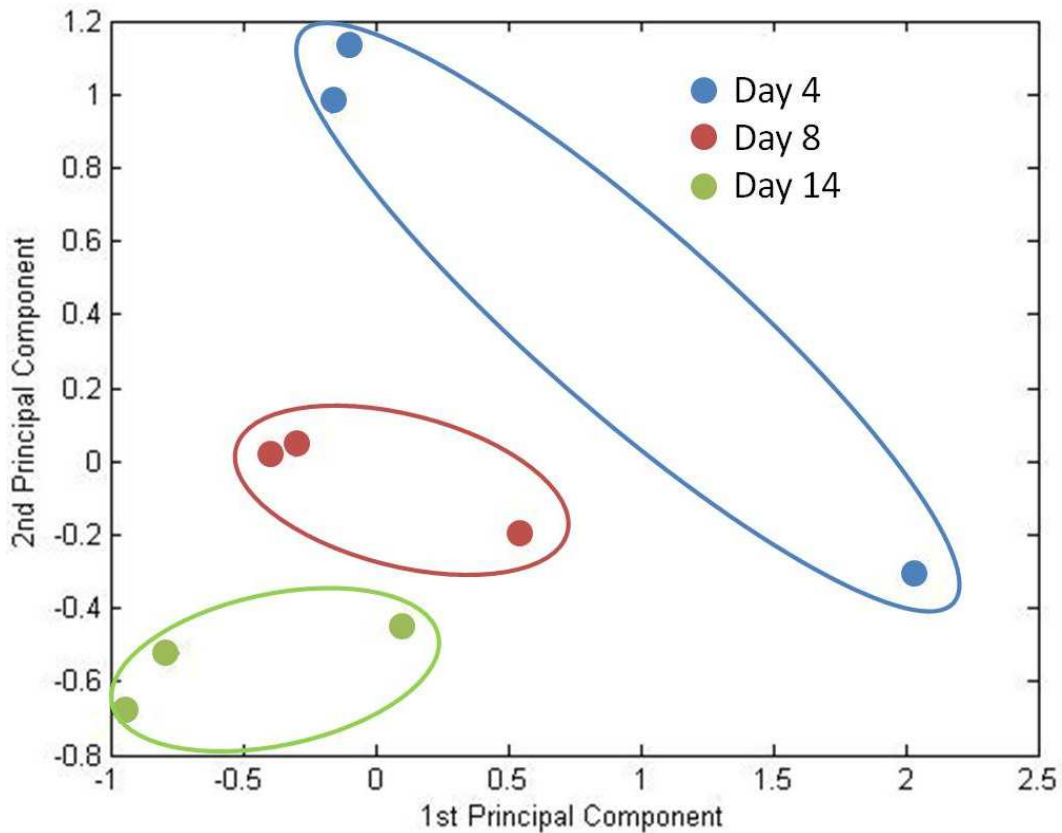


Figure 4-1: Principal Component Analysis (Over Time)

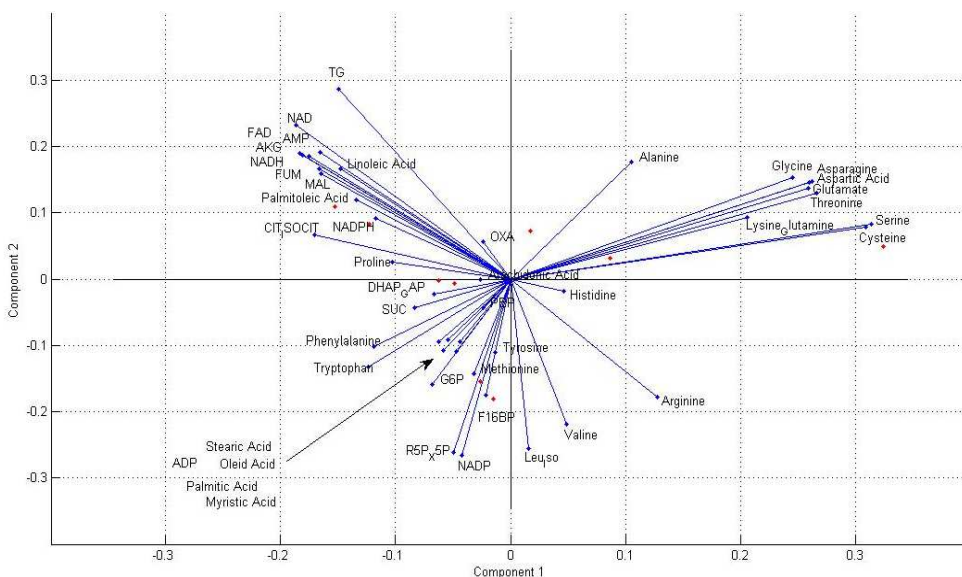


Figure 4-2: Components Scores (Over Time)

We then examined separation between knockdown conditions on day 8 and day 14. We observed strong clustering of DGAT and FSP, and weak clustering of PCX and IDH, with control groups in between (Figure 4-3). Metabolites contributing most strongly to the separation between DGAT/FSP and the other conditions mainly included amino acids and fatty acids (Figure S-0-1 in Appendix D). Fructose 1,6-bisphosphate caused separation between PCX and IDH, indicating that PCX knockdown may lead to increased concentrations of glycolytic intermediates.

On day 14, PCX and IDH clustered together (still with a high degree of scatter) and DGAT/FSP clustered closer to the control condition (Figure 4-3). Several cofactors (NAD, NADPH, etc) strongly contributed to separation between experimental conditions as well as citrate and some amino acids (Figure S-0-2 in Appendix D). Interestingly, though we observed significant differences in TG accumulation between control and knockdown conditions, this was not identified in the PCA analysis.



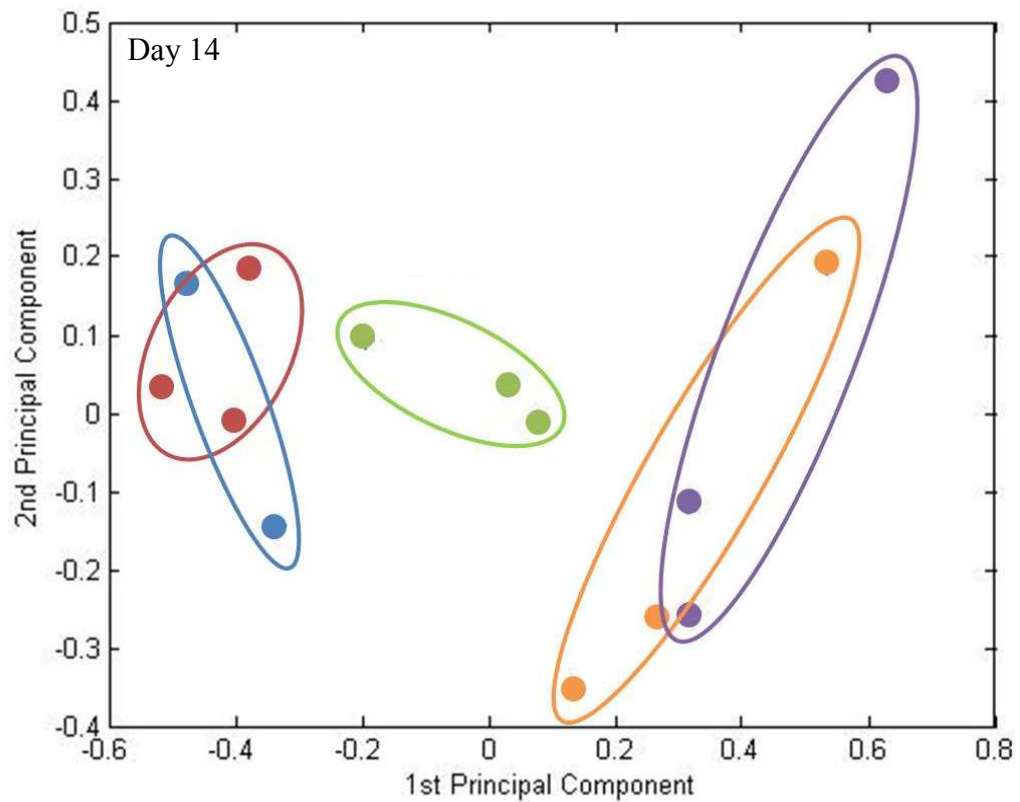
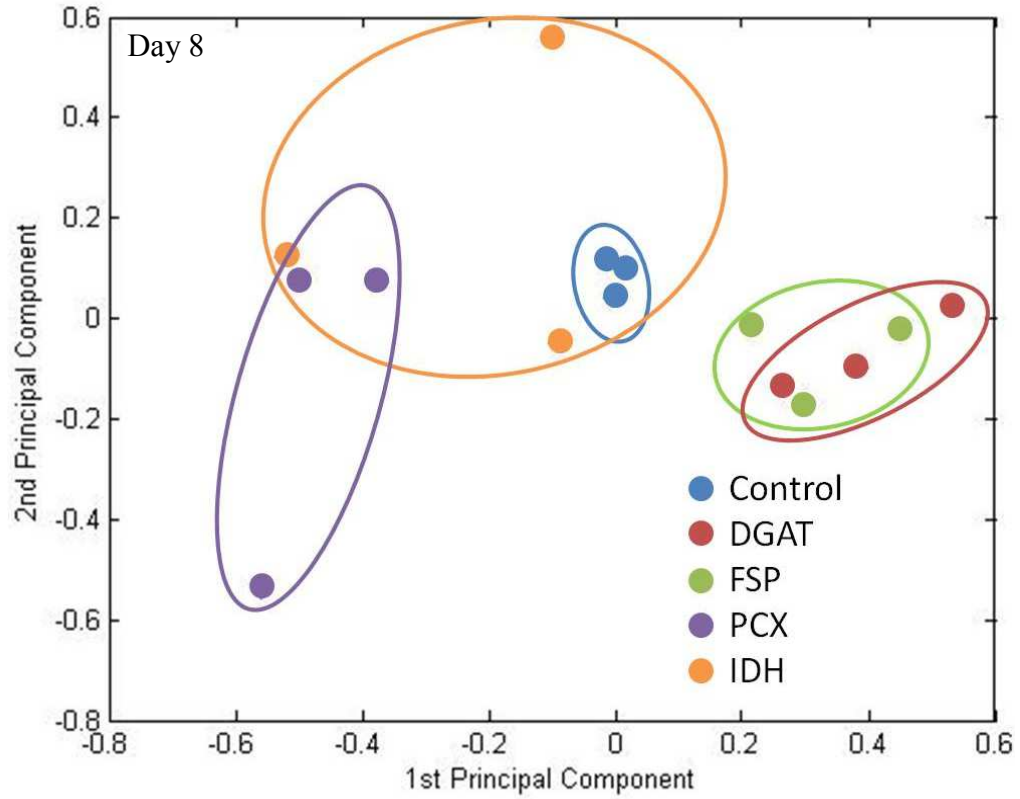


Figure 4-3: Principal Component Analysis (Day 8 and 14)

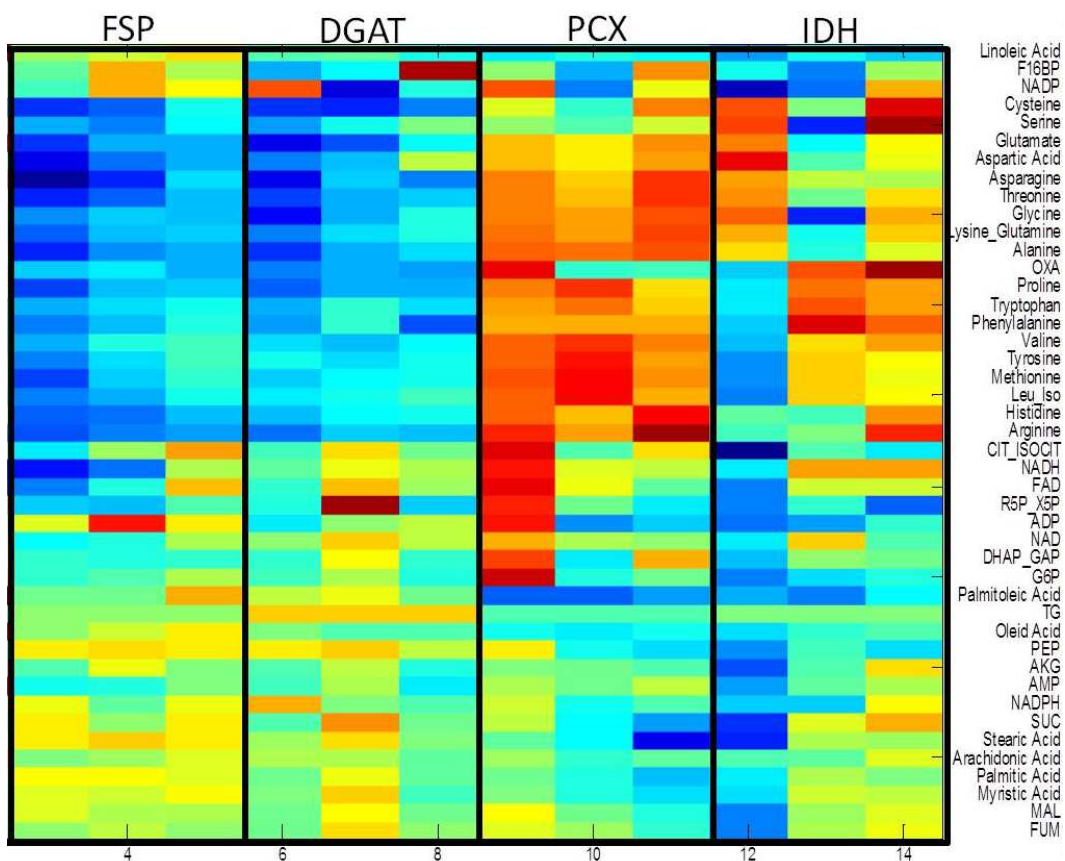


Figure 4-4: Heatmap of Normalized Metabolite Concentrations (Day 8)

Each column represents a biological replicate, and each row represents a metabolite measurement. Red/orange indicates increased concentrations, blue indicates decreased concentrations.

Lastly, in order to visualize changes in concentration across the entire network, we constructed a heatmap of normalized metabolite concentrations (Figure 4-4). We again observed strong similarities between the FSP and DGAT conditions when compared to the control and to the other knockdown conditions. PCX and IDH knockdown also have similar effects, but not to the same extent as FSP and DGAT. Metabolites were organized on the y-axis based on hierarchical clustering (Figure S-0-1 in Appendix E). Metabolites towards the bottom clustered most strongly. These included many TCA cycle intermediates and fatty acids. Interestingly, oxaloacetate clustered with amino acids, indicating that

changes in its concentration are more closely correlated with amino acid metabolism. Similarly, citrate clustered with cofactors, suggesting that the citrate pool is strongly affected by the cofactor balance within the cell.

#### ***4.5 Discussion***

In this chapter, we examined the effect of individual enzyme knockdown on metabolite profiles. Overall, changes in intracellular metabolite concentrations were greater on day 8 than day 14. This likely reflects the redundancy built-in to biological pathways, and the cell's ability to respond to perturbations and return to equilibrium. On day 8, 4 days after the initial siRNA treatment, we observe many significant differences in intracellular metabolite concentrations. However, by day 14, many of these differences have normalized. Despite this fact, TG accumulation on day 14 is still significantly reduced, indicating that perturbations to metabolism during the early stages of adipogenesis do affect the final differentiated state of the cells.

FSP and DGAT knockdown led to the most significant changes in metabolite concentrations, and these changes were surprisingly similar to each other. FSP/DGAT knockdown resulted in increased concentrations of TCA cycle intermediates (citrate, fumarate, and malate), which reflects an accumulation of precursors for fatty acid synthesis, and thus, feedback inhibition of the process. Fatty acid concentrations were highest in FSP knockdown, indicating that increased lipolysis (due to reduced droplet stability) results in accumulation of free fatty acids. In DGAT knockdown, some fatty acids increased, while others remained relatively constant, suggesting that accumulating fatty acids (before

esterification) had an immediate impact on continued fatty acid synthesis. Interestingly, unsaturated fatty acid concentrations were lower in DGAT and FSP knockdowns. By day 14, intracellular concentrations of TCA cycle intermediates, amino acids, and glycolytic intermediates decreased; however fatty acid levels increased, compared to control, with the exception of arachidonic acid, which is not typically incorporated into triglycerides.

Principal component analysis confirmed the empirical observations that FSP and DGAT knockdown had similar effects on metabolite profiles (Figure 4-3). On day 8, FSP/DGAT clustered tightly together, while PCX, IDH and control experiments were more spread. On day 14, FSP/DGAT were still distinct from PCX and IDH, but clustered more closely with the control group. This observation strengthens the hypothesis that intracellular metabolism returns to normal after metabolic perturbation.

While the effects of PCX and IDH knockdown were distinctly different from FSP and DGAT knockdown, they were also less similar to each other. They both led to increased concentrations in TCA cycle intermediates, but not significantly. Both conditions led to increased concentrations of many essential amino acids. IDH knockdown also had a stronger effect on glycolytic intermediates. Most notably, PCX knockdown led to significant reduction (up to 50%) in fatty acid concentrations on day 8, reflecting decreased availability of acetyl-coA, but these changes were smaller on day 14.

Interestingly, IDH knockdown did not significantly affect NADP/NADPH levels within the cell. One possible explanation is that there are many reactions

which produce and consume these cofactors, and, as mentioned previously, redundant pathways help to minimize the propagation of perturbation. However, cofactors are notoriously difficult to quantify due to stability and binding issues. For example, since cofactors are so ubiquitously utilized, they may bind to many substrates upon cell lysis, which impairs our ability to detect them at the appropriate m/z ratio. Furthermore, some cofactors are more stable than others, so it can be difficult to calculate redox and energy balance ratios accurately. Principal component analysis generally clustered PCX and IDH together, but not as tightly as FSP/DGAT and with less overlap between the two groups (Figure 4-3). At both time points, PCX/IDH were distinct from FSP/DGAT, but closer to the control group on day 8 than on day 14.

## ***5 Coordinated Knockdown of Multiple Targets***

### ***5.1 Abstract***

Based on the results from Chapters 2 and 4, we selected pyruvate carboxylase (PCX), diacylglycerol acyltransferase (DGAT), and fat specific protein (FSP27) as targets for combined knockdown experiments. Individual knockdown of each of these enzymes led to significant reduction in TG accumulation, ranging from 20-30%. When we combined knockdown of multiple targets, we saw slightly greater reduction across the board. Interestingly, combinations including PCX (i.e. PCX/DGAT and PCX/FSP) did not further reduce TG accumulation compared to DGAT or FSP alone. However, combining DGAT and FSP knockdown led to the largest reduction in TG accumulation.

Double knockdown of DGAT and FSP increased concentrations of TCA cycle intermediates, indicating feedback inhibition from fatty acid accumulation, as well as decreased amino acid concentrations, suggesting an overall depression in metabolic activity. In order to resolve metabolic fluxes, we conducted an isotopic labeling experiment and found significant differences in 24 out of 66 fluxes. Double knockdown resulted in a general decrease in flux through TCA cycle (>30%) and slight changes in amino acid metabolism, without affecting flux through glycolysis. In addition, fatty acid synthesis was reduced by 44% and TG accumulation was reduced by 36%. These results show that perturbing multiple steps in the same stage of TG synthesis, or in closely related stages may have the largest effect.

## 5.2 Introduction

Based on individual knockdown data, we selected pyruvate carboxylase (PCX), diacylglycerol acyltransferase (DGAT), and fat specific protein (FSP27) as targets for further analysis. Our goal is to selectively knockdown multiple stages of TG accumulation to examine the combinatorial effects. We combined knockdown of enzymes in a pair wise fashion, to understand if double knockdown results in a synergistic or additive effect (

Figure 5-1). For example, we know that individual knockdown of PCX and DGAT reduce TG accumulation, via reduction in fatty acid synthesis and TG synthesis, respectively. However, will combined knockdown of both enzymes reduce TG accumulation to a greater extent? Or is single knockdown sufficient to achieve the lowest level of TG accumulation. If PCX knockdown reduces synthesis of fatty acids, then it is possible that simultaneously knocking down DGAT will not have a significant effect because there is not enough substrate present in the first place.

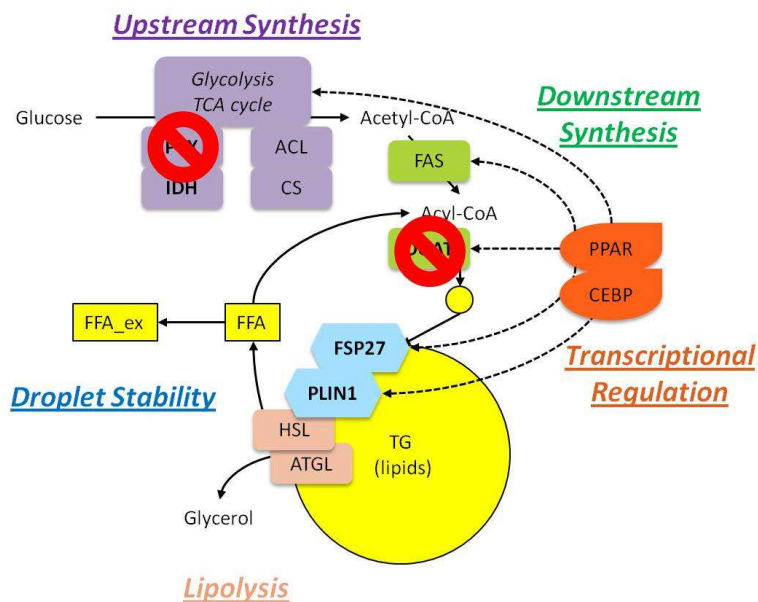


### Figure 5-1: Example Knockdown Strategy for Reducing TG Accumulation

To examine the effects of knockdown, we decided to use metabolic flux analysis (MFA) and isotopic labeling. MFA is a powerful tool in systems biology research; the basic principle is that intracellular reaction rates (fluxes) can be estimated based on exchange rates of extracellular metabolites. Previous work in the lab developed a stoichiometric model of adipocyte metabolism for MFA (Si, 2007). This model consists of 66 reactions and 38 metabolites. The intracellular fluxes are estimated by solving a constrained nonlinear optimization problem (Nolan, 2005).

To enhance this analysis, we also employed stable isotopic labeling within an elementary metabolite unit (EMU) framework. Isotopic labeling improves upon MFA by resolving the fluxes through parallel metabolic pathways and metabolic cycles (Wiechert, 2001). For isotopic labeling, a labeled substrate (e.g. [1,2-<sup>13</sup>C] glucose) is fed to the cells, and the labeled carbon atoms are then distributed throughout the metabolic network. The isotopic enrichment in specific metabolite pools can be measured and used to estimate intracellular fluxes. However, modeling every possible isotopomer dramatically increases the complexity of the problem (for example, citrate, a 6-carbon molecule has 64 possible isotopomers). To reduce the number of isotopomer variables and equations, we can perform an EMU decomposition (Antoniewicz, 2006; Si, 2009).



### **5.3 *Materials and Methods***

#### **5.3.1 *Materials***

3T3-L1 cells were purchased from ATCC (Manassas, VA). Tissue culture reagents including Dulbecco's Modified Eagle's Medium (DMEM), calf serum (CS), fetal bovine serum (FBS), human insulin, and penicillin/streptomycin were purchased from Invitrogen (Carlsbad, CA). Unless otherwise noted, all other chemicals were purchased from Sigma (St. Louis, MO).

#### **5.3.2 *Cell culture***

Low passage 3T3-L1 preadipocytes were seeded into 12 well plates at a concentration of  $2 \times 10^4$  cells/cm<sup>2</sup> and cultured in a humidified incubator at 37°C and 10% CO<sub>2</sub>. The cultures were expanded in a growth medium consisting of DMEM supplemented with 10% v/v CS, 100 units/mL penicillin, 100 µg/mL streptomycin, and 2.5 µg/mL amphotericin. The growth medium was changed every 2-3 days until confluence was reached. Two days post-confluence (designated as day 0), the cells were induced to differentiate using an adipogenic cocktail (DM1: 1 µg/ml insulin, 0.5 mM isobutylmethylxanthine, 1 µM dexamethasone, and 2 nM triiodothyronine) added to a basal medium (DMEM with 10% FBS and penicillin/streptomycin/amphotericin). After 48 h, the first induction medium was replaced with a second induction medium (DM2) consisting of the basal adipocyte medium supplemented with only insulin (1 µg/ml). After another 48 h, DM2 was replaced with the adipocyte basal medium. On days 4, 8, and 14, images were recorded for three randomly selected wells, which were then sacrificed for enzymatic assays of total TG content.

### ***5.3.3 siRNA Transfection***

Beginning on day 4 post-induction, cells were transfected with siRNA at 30 nM. Lipofectamine 2000 (Invitrogen) was used as a transfection reagent based on the manufacturer's suggested protocol. Briefly, Lipofectamine and the target siRNA were combined in Opti-Mem reduced serum medium and incubated for 10 minutes at room temperature to allow the nucleic acids to complex with the liposomes. After replacing the insulin supplemented adipocyte medium (DM2) with the reduced medium containing the siRNA-lipid complexes, the cells were incubated as normal. Preliminary experiments using nonsense siRNA showed no signs of cytotoxicity. Knockdown was sustained by continuing the siRNA treatment every 48 hours for the remainder of culture.

The siRNA sequences were optimized for target specificity based on Sigma's Rosetta predictions. The vendor did not provide the exact nucleotide sequences, but the approximate nucleotide positions on the target RNAs are known. The sequence locations for each target are listed in Table 2. The nucleotide position is given relative to the beginning of the NCBI RefSeq sequence for the given target gene. All sequences are for the target enzyme in mice, because 3T3-L1 preadipocytes come from a murine source. As a control, cells were transfected with a nonsense siRNA sequence. For double knockdowns, cells were transfected with either a combination of two target sequences, each at 30 nM, or a single target sequence combined with the scrambled sequence (so the total concentration of siRNA was held constant at 60 nM). Preliminary experiments were conducted to ensure that increased siRNA concentration did not lead to cell death.

#### **5.3.4 Triglyceride assay**

Triglyceride measurements were performed on cell lysates as described previously. Briefly, cells were rinsed with warm 1× PBS after aspirating the medium, and lysed *in situ* using a 0.1% SDS buffer followed by sonication. Free glycerol and TG were measured using an enzymatic assay kit from Sigma (catalog number TR0100).

#### **5.3.5 Metabolite Extractions**

Because salt-based detergents (e.g. SDS) are not compatible with LCMS, cells were extracted using an organic solvent mixture, methanol/chloroform/water (48:48:4 v/v) as follows. On days 8 and 14, media was removed and collected for separate analysis. Cells were rinsed with ice cold PBS and 524 uL of methanol/water (91:9 v/v) was added to each well. Cells were detached from the well using manual scraping over ice and stored in a 1.5 mL eppendorf tube. 476 uL of chloroform was added to each tube to reach the final concentration. Chloroform degraded tissue culture plastic, and thus could not be added directly to the well. The extraction protocol was optimized by varying the solvent to cell ratio to ensure that the volume of methanol/water was sufficient to detach cells from the plate and extract the metabolites while not overly diluting the samples. After addition of chloroform, the samples were vortexed and freeze/thawed 3 times in liquid nitrogen in order to fully lyse the cells. In order to remove cell debris, samples were centrifuged at 10,000 rpm for 10 minutes, and dried using a speed-vac at room temperature. Samples were reconstituted in 100 uL methanol/water (50:50 v/v) and stored at -20 °C until further analysis.

### **5.3.6 LC-MS**

We analyzed the metabolite concentrations using multiple reaction monitoring (MRM) experiments performed on a QTRAP 3200 triple quadrupole ion-trap mass spectrometer (Ab Sciex, Framingham, MA). Chromatographic separation was achieved using an Agilent 1200 liquid chromatography system (Agilent, Santa Clara, CA). Separate runs were conducted for amino acids, fatty acids, and TCA/glycolysis intermediates. A complete list of columns and solvents used for chromatographic separation is available in the Appendix B. Each metabolite was confirmed based on its MRM transition (precursor and product ion pairing), and were quantified by integrating the ion chromatogram to obtain the corresponding area under the curve (AUC). The AUC for each metabolite was then normalized to the total ion count (TIC) of the corresponding sample. Metabolite identities were confirmed based on their unique fragmentation spectra. Metabolite extraction buffers were not compatible with the Hoechst dye assay, which prevented the use of DNA content for normalization.

### **5.3.7 Stoichiometric Model**

A stoichiometric network model of adipocyte intermediary metabolism was constructed as described previously (Si, 2007). Table 5 in Appendix F provides a complete listing of the reactions. Intracellular fluxes were estimated from measurements on metabolite uptake and output rates (exchange fluxes) by solving a constrained non-linear optimization problem with stoichiometric and thermodynamic constraints (Nolan, 2005).

### ***5.3.8 Isotopomer Model***

Model based analysis of isotopomer distribution patterns provided additional flux estimates for selected experimental conditions. Briefly, calculation of reaction fluxes from mass isotopomer distribution data proceeded as follows (Si, 2009). The calculation initializes with an assumed set of reaction fluxes that satisfy the metabolite balance constraints (step 0). Steady state isotopomer balance equations then calculate the corresponding isotopomer distribution pattern (step 1). This calculation utilized the elementary metabolite unit (EMU) framework (Antoniewicz, 2006) to reduce the number of model equations and variables. The EMU decomposition also eliminated non-linear equations of mass isotopomer distribution (MID) and reaction flux variables. The next algorithm step compares the simulated isotopomer pattern against measured data and updates the reaction fluxes (step 2). Steps 1 and 2 repeat until the simulated and measured data converge. These steps were implemented through non-linear constrained optimization. The objective function was to minimize the sum-squared error between measured and calculated intracellular metabolite mass isotopomer distribution patterns, using measured metabolite exchange fluxes as bounds. The optimization problem was solved using a custom code written in MATLAB (Natick, MA).

### ***5.3.9 Isotopomer Measurements***

Previous work identified glucose labeled on carbons 1 and 2 as the optimal isotopomer input substrate. Thus, the labeling experiments used an enriched medium with [1,2-<sup>13</sup>C]glucose added at a final concentration of 4.5 g/L to a

glucose-free basal medium (DMEM supplemented with 10 % FBS and penicillin/streptomycin). After 2 days of culture in labeled media, metabolites were extracted (as above). We then analyzed the mass isotopomer distributions of target metabolites using a TOF-MS scan in negative mode and hydrophilic interaction chromatography (see Appendix B for column and solvent details). We simultaneously performed a product ion scan for each metabolite and its respective isotopomers (e.g. M+1, M+2, etc.) in order to confirm the identity of each species based on its fragmentation pattern. To validate this method, we analyzed mixtures of labeled and unlabeled standards and were able to recover the theoretical distribution. See Appendix H for a further explanation of this analysis.

#### ***5.3.10 Target Metabolites***

Previous work established the accuracy of EMU-based flux estimation based on certain target metabolites and determined optimal combinations of target metabolites (e.g. MAL/CIT or GAP/CIT). Although previous studies identified MAL/CIT as an optimal combination we also measured MIDs for 2-oxoglutarate (OXO), fumarate (FUM), succinate (SUC), aspartate (ASP), glutamate (GLU), serine (SER), and threonine (THR), as well as intermediates of the pentose phosphate pathway septulose 7-phosphate (S7P) and erythrose 4-P (E4P). Our analysis methods precluded the use of GAP, PEP, PYR and OAA, because their masses were not unique (i.e. other metabolites in the cell have the same mass and confound the analysis).

## 5.4 Results

### 5.4.1 Metabolic Network Mapping

In order to visualize changes in metabolite levels and fluxes, a network map was created in cytoscape (Version 3.1.1), including all metabolites and reactions in the stoichiometric model. Metabolites are represented as circles, and reactions are represented as triangles. Arrows represent the predominant direction of flux, though many reactions are reversible. Cofactors were left out of the network map for simplicity. The complete network is shown in Figure 5-2.

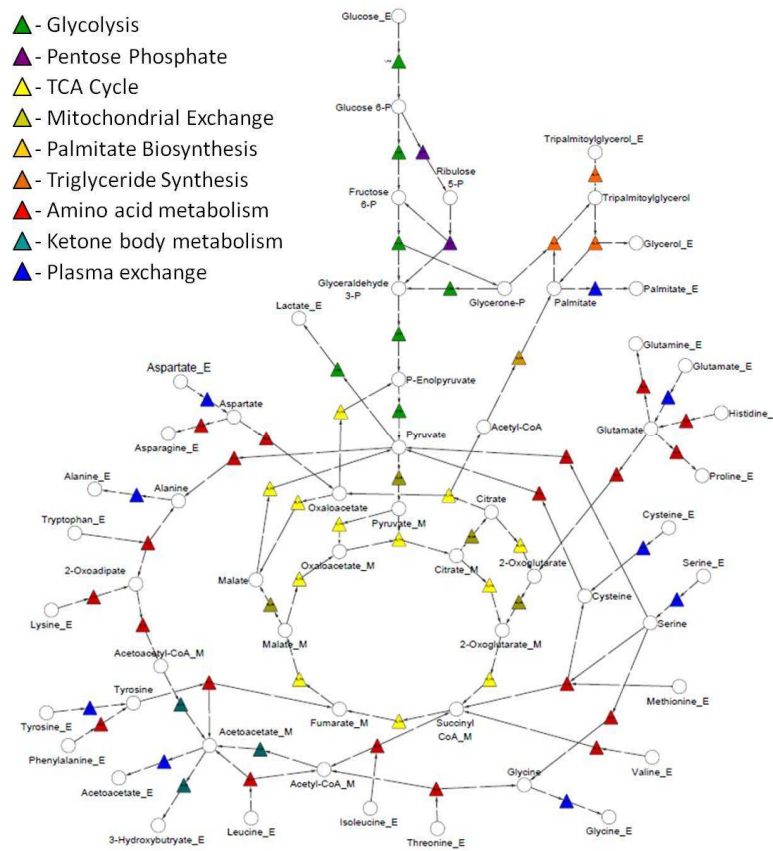


Figure 5-2 Network map of adipocyte metabolism

Circles represent metabolites and triangles represent reactions. Extracellular metabolites are denoted “\_E” and mitochondrial metabolites are “\_M”. Reaction colors are based on canonical pathways. Many reactions were condensed to form the stoichiometric matrix; therefore some extracellular fluxes have been combined with intracellular metabolic reactions (e.g. [ext] glucose → [int] glucose-P)

#### 5.4.2 Reduced TG Accumulation in Coordinated Double Knockdown

The amount of intracellular TG was monitored via enzymatic assay on days 4, 8 and 14. TG accumulation on day 4 was negligible. Similar to previous experiments, significant changes in TG were not observed on day 8, likely due to incomplete differentiation at that time point. However, by day 14 larger differences were noticeable (

Figure 5-3). The reduction in TG varied from 21 to 42%, with the largest reduction occurring in the FSP-27/DGAT double knockdown, although not statistically different from other knockdown conditions (note:  $p=0.02$  for PF to FD). Interestingly, combinatorial knockdown with PCX (of both FSP and DGAT) did not further reduce TG accumulation compared to knockdown of FSP and DGAT alone. Based on these observations, the combination of FSP-27 and DGAT was selected for further metabolic flux and isotopomer analysis.

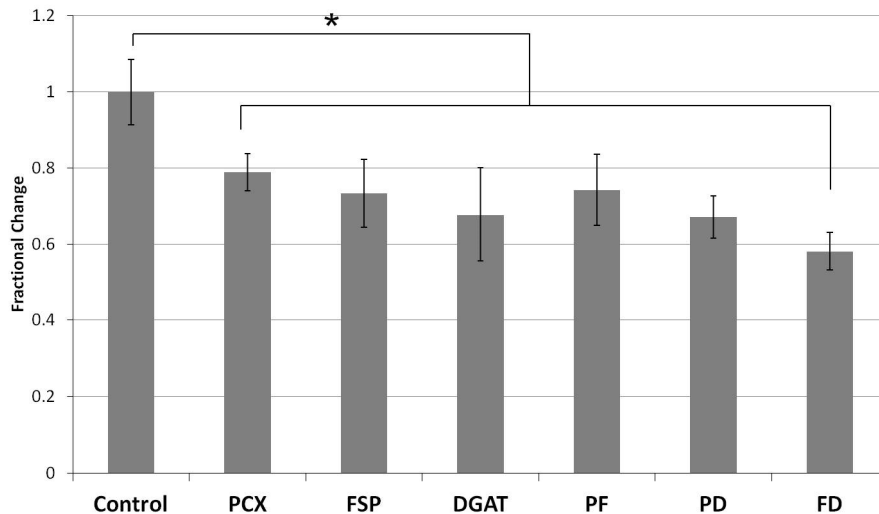


Figure 5-3 Reduction in Intracellular Triglyceride Concentration

Day 14 post-induction for PCX, FSP and DGAT knockdowns. TG concentrations of each knockdown condition were normalized to the control (scrambled siRNA) and error bars represent the standard deviation of  $n=3$  biological replicates. \*indicates statistically significantly different from control ( $p < 0.05$ ).



### ***5.4.3 Metabolite Levels and Measured Extracellular Fluxes***

In general, double knockdown of FSP/DGAT led to increased concentration of TCA cycle intermediates and decreased concentrations of intracellular amino acids. As seen in the single knockdown experiments, differences between control and treated conditions are more prominent on day 8. A complete table of intracellular metabolite concentrations is shown in Table 6 in Appendix G. Buildup of citrate is consistent with decreased triglyceride accumulation, as citric acid is used to produce acetyl-coA which feeds into fatty acid synthesis. Decreased lipogenesis (due to DGAT) and increased lipolysis (due to FSP) result in slightly elevated levels of saturated fatty acids (myristic, palmitic and stearic), which likely causes feedback inhibition towards fatty acid synthesis.

Overall, there were less apparent significant differences in measured extracellular fluxes (Table 7). Double knockdown did not affect glucose uptake on day 8, and reduced uptake by 10% on day 14. Fatty acids were mostly taken up by the cells at both time points, and knockdown did not reverse this trend. On average, amino acid exchange rates were very low compared to flux through glycolysis, and mostly consistent between control and knockdown.

### ***5.4.4 Mass Isotopomer Distribution***

MIDs were measured for numerous intermediates of the TCA cycle, amino acid metabolism and pentose phosphate pathway. As expected, each of the measured metabolites showed mass enrichment due to the labeled substrate. In general, 30-50% of a respective metabolite pool remained unlabeled (due to loss of label throughout the metabolic pathway or input from unlabeled substrates such

as extracellular amino acids in the media). For citrate, 25% of the metabolite pool was M+2 and <10% was fully labeled (M+6). In contrast, natural abundance of <sup>13</sup>C-glucose is ~1%, so the expected enrichment of M+1 citrate is roughly 6%, M+2 is ~1%, and enrichment of higher masses due to natural isotopic abundance decrease from there. Fumarate and malate showed similar labeling distributions. Amino acids overall retained less label, reflecting their displacement from central carbon metabolism and exchange with the media. For example, <20% of the aspartate pool was M+2 and ~5% was fully labeled (M+4). Differences between control and double knockdown (FSP/DGAT) were subtle but noticeable at both time points. A full summary of measured MIDs is available in Table 8 in Appendix I.

Although previous work identified CIT/MAL as optimal measurements for flux estimation (Si, 2009), initial modeling using this combination yielded variable results. This likely reflects discrepancies between the metabolite pools in the mitochondria and cytosol. The metabolite extraction protocol analyzes total cell lysates, and cannot distinguish between intracellular compartments; however, there is likely to be variation between these pools. Initial modeling showed consistency between mitochondrial and cytosolic citrate (suggesting rapid equilibrium between compartments), but MIDs for malate were often different. Therefore, we replaced malate with fumarate, because the concentration of fumarate in the cytosol (and metabolism therein) is negligible.

#### **5.4.5 Flux Profiles**

Using EMU decomposition and measured MIDs of citrate and fumarate, in combination with measured extracellular fluxes, all 66 reaction rates were estimated. A full table of these rates is available in Table 9 in Appendix J. To account for the slight variations in glucose uptake (both in experiments and results), all fluxes are expressed as a percentage of the glucose uptake for a given experiment (Table 10). Similar to trends in metabolite levels, differences in metabolic rates were more significant on day 8 than day 14. After normalization, 24 out of 66 estimated fluxes were significantly different from control on day 8, with only 10 significant differences on day 14. Double knockdown resulted in a general decrease in flux through TCA cycle (>30%) and slight changes in amino acid metabolism, without affecting flux through glycolysis (likely due to normalization). In addition, fatty acid synthesis was reduced by 44% and TG accumulation was reduced by 36%.

#### **5.4.6 Analyzing Network-wide Effects of Knockdown**

To understand the effects of the double knockdown, we plotted differences in measured metabolites along with fluxes estimated from the isotopomer analysis on the network map. We removed any fluxes that were less than 5% of the glucose flux (for simplicity), which eliminated all of the reactions in amino acid and ketone body metabolism, as well as corresponding exchange fluxes. Significant differences ( $p < 0.05$ ) are color coded- red for decreases and green for increases, with darker colors indicating a larger difference (

Figure 5-4). The most noticeable changes in flux are the reduction of palmitate biosynthesis and subsequent decreases in conversion of citrate to acetyl-coA and oxaloacetate. Decreased flux towards palmitate and triacylglycerol results in accumulation of citrate which propagates throughout the TCA cycle.

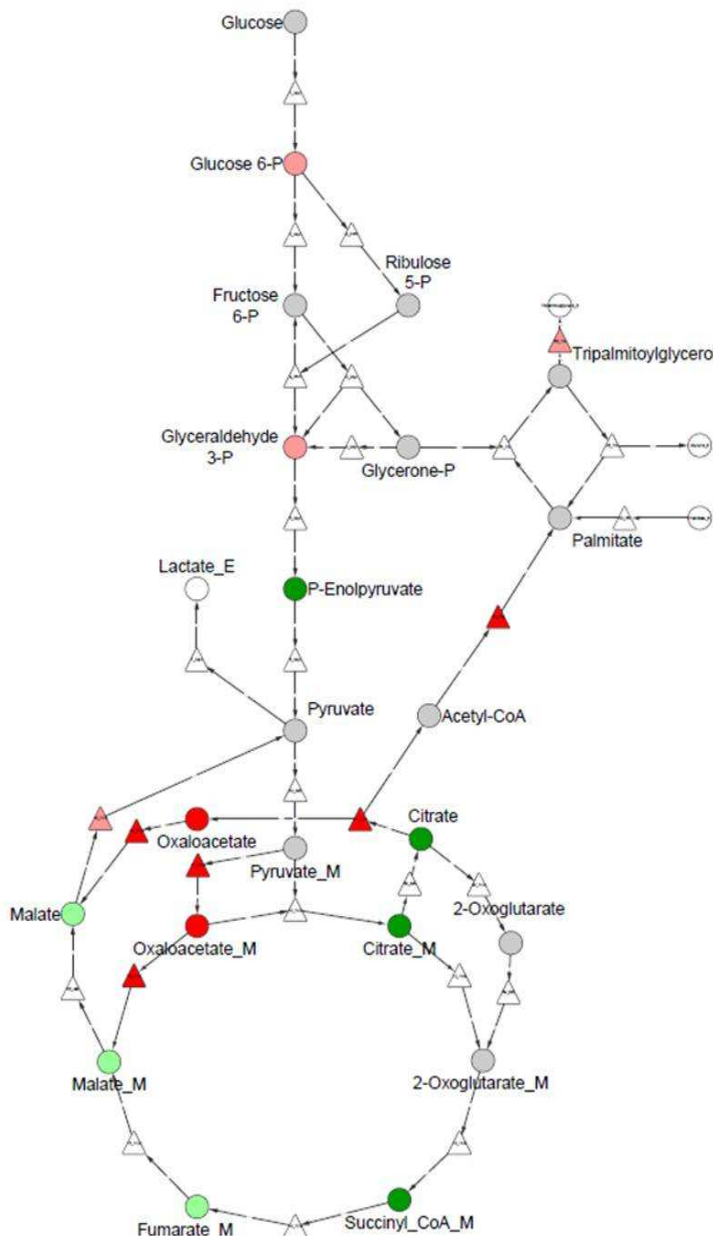


Figure 5-4 Metabolic Changes of Double Knockdown

Significant differences in metabolite concentrations (measured) and fluxes (estimated) on day 8. Circles represent metabolites and triangles represent fluxes. Decreasing metabolite concentrations and fluxes are colored red, and increasing

values are colored green ( $\pm 0-40\%$  difference), with darker colors indicating a higher magnitude of change ( $\pm >50\%$  difference).

## 5.5 Discussion

In this chapter, we investigate the combined knockdown of multiple enzymes. Based on preliminary experiments, we selected pyruvate carboxylase (PCX), diacylglycerol acyltransferase (DGAT) and fat specific protein (FSP) as targets, representing three different stages of triglyceride accumulation. We conducted isotopic labeling experiments to estimate fluxes through the metabolic network in order to understand the effects of knockdown. Based on the stoichiometric model, we constructed a network map of adipocyte metabolism to visualize these changes.

As expected, knockdown of PCX, DGAT and FSP led to significant reduction in TG accumulation (

Figure 5-3). The effects of single knockdown ranged from 20-30%. However, while PCX had previously shown the highest degree of knockdown, the effects were not as strong in these experiments. Overall, double knockdown led to slightly lower TG accumulation than single knockdown. However, when we compare double knockdowns to single knockdowns, it becomes clear that PCX does not contribute any added effect to DGAT or FSP knockdown. FSP and DGAT knockdown reduce TG accumulation by  $\sim 25\%$  and  $33\%$ , respectively. PCX/FSP and PCX/DGAT knockdown reduce TG accumulation by the same amounts. In contrast, combination of FSP and DGAT leads to a reduction of over  $40\%$ , which is greater than FSP or DGAT alone.

These results suggest that inhibiting one step of early synthesis (i.e. the production precursors for fatty acid biosynthesis) is not an optimal strategy for reducing TG accumulation. This is likely due to the fact that there are many production pathways for acetyl-coA within the network. Although knocking down PCX leads to a reduction in fatty acid synthesis, it does not really matter if fatty acids are not able to be esterified into TG (e.g. DGAT knockdown), or fatty acids are accumulating due to increased lipolysis (e.g. FSP knockdown). In contrast, combining knockdown of DGAT and FSP has an additive effect on reducing TG accumulation, which suggests that their distinct mechanisms work in tandem. DGAT knockdown reduces the final step in TG synthesis. FSP knockdown exposes the TG that *is* produced (within LDs) to lipolytic degradation. Finally, because DGAT is impaired, the lipolysis/lipogenesis cycle is shifted towards lipolysis.

An examination of metabolite concentrations confirms these observations, on day 8, saturated fatty acid concentrations are increased (compared to control), though unsaturated fatty acid concentrations are actually lower. However, by day 14, even unsaturated fatty acids have begun to accumulate within the cell. The accumulation of fatty acids also leads to increased concentrations of TCA cycle intermediates on day 8, indicating feedback inhibition towards production of more fatty acids. On day 14, TC cycle intermediates have decreased, suggesting an overall depression of metabolism due to the knockdown, although, glucose consumption is only slightly depressed.

Isotopic labeling further explains the effects of double knockdown. Although the changes in MID composition were subtle, they represent significant differences in the flux patterns throughout the network. Even after normalizing to glucose uptake, 24 out of 66 fluxes were significantly different from the control on day 8, with 10 significant differences on day 14. On day 8, flux through the entire TCA cycle was decreased. This complements the observation of accumulation of these intermediates, and illustrates that reducing TG accumulation in later stages propagates throughout the entire metabolic network. On day 14, flux was still decreased, but not to a significant extent, confirming that the cells may be returning to equilibrium over time. However, this also may reflect inefficiencies in knockdown. Knockdown led to significant changes in amino acid metabolism and exchange rates at both time points; however, these rates were such a small percentage of overall flux through the network, that they likely had little effect. Interestingly, isotopic labeling estimated a decrease in TG accumulation, even on day 8, suggesting that changes in intracellular fluxes at early time points preempted the subsequent reduction in the amount of TG.

Though the flux rates generally make sense, and agree with previous work, reaction 12 had a reaction rate of zero. Reaction 12 is the conversion of citrate to oxoglutarate in the mitochondria (condensed with the isomerization of citrate to isocitrate). However, the stoichiometric model has a built in “loop” transporting citrate out of the mitochondria (reaction 63), and conversion to oxoglutarate in the cytosol (reaction 20). Both of these reaction rates are positive, and comparable in magnitude to the other fluxes in the TCA cycle. This is likely an artifact of the

stoichiometric model and isotopomer analysis, and not an actual representation of the fluxes within the cell. One possible explanation would be that the labeling pattern of citrate is slightly different from fumarate, so the model forces flux from citrate out of the mitochondria first to correct this difference (i.e. some of the label on citrate will be transferred to acetyl-CoA and oxaloacetate in reaction 17). This reflects one drawback of using this stoichiometric model, because in our analysis, we lumped together the cytosolic and mitochondrial compartments. Though we assume rapid equilibrium between mitochondrial and cytosolic citrate (and thus, assume that the MIDs will be the same), this may not be the case in practice. In future analysis, we may attempt to fractionate the cell lysates and analyze the mitochondrial fraction on its own.



## ***Future Directions and Recommendations***

In this thesis, we aim to demonstrate the importance of cellular hypertrophy in adipocytes and examine the metabolic enzymes which contribute to TG accumulation. We identified several targets which significantly reduced TG accumulation (and subsequently, adipocyte size). These targets included pyruvate carboxylase (PCX), isocitrate dehydrogenase (IDH), diacylglycerol acyltransferase (DGAT), fat specific protein 27 (FSP), and perilipin (PLIN1). We conducted a metabolomic analysis to understand the network-wide effects of knockdown. We also examined the effect of combined knockdown of multiple targets. When combined, FSP and DGAT knockdown led to the largest reduction in TG accumulation; therefore, we used isotopic labeling and metabolomic analysis to understand the mechanistic effects of knockdown.

Proteomic analysis is still needed to confirm knockdown of target enzymes. Although RT-PCR of PLIN1 showed strong knockdown at early time points, mRNA levels increased over the course of the experiment. We assume, based on reduction in TG accumulation, that knockdown was successful for the other targets; however, mRNA and protein levels were not yet measured. While RT-PCR is a standard method of measuring transfection efficiency, the key outcome of transfection is a reduction in protein levels. Therefore, we plan to repeat knockdown experiments and measure protein content at each time point, compared to the untreated control. This analysis will be especially important in understanding the decreased affect on metabolite concentrations and fluxes over time. While it is reasonable to assume that the cells are striving to reach

equilibrium, and regulating redundant pathways to respond to our perturbations, it is important to confirm successful knockdown over time (i.e. if transfection efficiency goes down over time, protein levels may be returning to normal as well). Based on the results of the analysis, it would also be interesting to extend the length of experiments. Although reduction in TG was greatest on day 14, changes in flux and metabolite concentrations were most noticeable on day 8, and seemed to normalize later in the experiment. It is possible, that differences between knockdown and control would continue to normalize over time, and disappear completely after multiple weeks of culture (which would be more reminiscent of an *in vivo* experiment). However, it is also possible that given further optimization of transfection and culture conditions, the effects of knockdown could be amplified over time. This analysis might require the use of a different culture system (because extended culture in 2D is typically not possible due to peeling and cell death). Therefore, we should continue to investigate 3D culture models (such as collagen or alginate), which can remain stable for many weeks. In addition, transfection of siRNA will also need to be optimized to accommodate this system.

Another recommendation would be to extend both the breadth and depth of the current study. We decided to analyze the effects of DGAT/FSP knockdown (i.e. isotopic labeling experiments) which provided valuable information about fluxes throughout the metabolic network. This flux data is arguably more valuable than metabolomic data, because it yields details about reaction rates, without having to make inferences from metabolite pools (which could be affected in a

number of ways). In addition, there was considerable noise in the metabolite concentration data, which may have confounded the results. This is likely due to the fact that we could not directly normalize to cell content. In contrast, mass isotopomer distributions are self-normalizing in the analysis, and might be more reliable, though, the methods are new, and require further validation. Taken together, isotopic labeling experiments would be useful for individual knockdowns of selected targets, as well as for the combinations already tested. This analysis would confirm observations of metabolite concentration changes, and help us to understand the effects of knockdown.

Furthermore, it would be interesting to investigate more targets, in all stages of TG accumulation. The most interesting conclusion was that DGAT/FSP combination had the largest effect on TG accumulation. This was especially surprising because individual knockdown of these two enzymes led to very similar differences in metabolite concentrations (despite the fact that the enzymes have very different mechanisms for promoting TG accumulation). Nevertheless, knocking down both enzymes seemed have the greatest effect by reducing TG synthesis (DGAT) and increasing lipolysis, based on decreased droplet stability (FSP). In contrast, combinations including PCX, did not seem to be effective, suggesting that other stages of the pathway were rate-limiting (i.e. knocking down DGAT led to an accumulation of fatty acids, so unless the production of fatty acids was reduced *dramatically*, it would not further affect TG accumulation). Perhaps a better strategy would be to only test double knockdown of multiple targets in upstream synthesis (e.g. blockade acetyl-coA synthesis), or droplet

stability (e.g. eliminate multiple LD-associated proteins). However, based on the current results, knocking down multiple targets in downstream synthesis (e.g., fatty acid synthase and DGAT), might not reduce TG accumulation further than individual knockdown.

Lastly, we need to expand our understanding of the mechanisms of TG reduction. For example, DGAT and FSP knockdown leads to accumulation of fatty acids, which causes decreased flux through the TCA cycle and accumulation of these intermediates. However, it is not clear what happens to these intermediates after they accumulate. It is possible that citrate, for example, is transported out of the cell. By day 14, TCA cycle intermediates decrease, compared to the control, as does flux through the TCA cycle; therefore, accumulation of citrate at early time points, may cause sufficient feedback within the TCA cycle and glycolysis as well, resulting in decreased glucose uptake. In addition to confirming knockdown efficiency, proteomic analysis will provide insight about regulatory changes to other enzymes and proteins. For example, upon knockdown of FSP-27, the cells may up-regulate transcription of other lipid-droplet associated proteins.

Taken together, our results provide insight into the mechanism of TG (fat) accumulation in adipocytes. Currently, none of the drugs approved by the FDA to treat obesity *actually* target adipose tissue. Therefore, it is our goal that a better understanding of adipose tissue metabolism and development will enable the investigation of new treatment strategies of obesity and related illnesses.

## *Appendix A: Sample Code for Image Analysis Algorithm*

```
% function [results, images, filenames]=BR_rad()

%Load files to be analyzed

filenames=uigetfile('20x A1 1.tif','MultiSelect','on');
% filenames=uigetfile('20x A1 1.tif');

if isnumeric(filenames)==1
    break
end

clc
clearvars -except filenames
close all

initialtime=clock;

%results setup
results=zeros(length(filenames),14);
countdrops=zeros(length(filenames),8);
hist=zeros(11,1);
for j=1:10
    hist(j)=100*j;
end
hist(11)=10^7;
Z=1;
skipcount=0;
sumlights=zeros(length(filenames),1);
% sumdarks=zeros(length(filenames),1);
% tempas=zeros(length(filenames),1);
% temps=zeros(length(filenames),1);

% The Program
for ImageNumber=1:length(filenames)
%% Load Files
    im_RGB=imread(filenames{ImageNumber});
%   im_gray=rgb2gray(im_RGB);
    im_gray=im_RGB(:,:,1);
    im_gray=double(im_gray);
    im_gray=im_gray/255;
    im_gray=wiener2(im_gray);
    S=size(im_gray);

%% Test if there is any fat using lights
    thr=(1-graythresh(im_gray))*(.667)+graythresh(im_gray);
    bwlight=im2bw(im_gray,thr);
    sumlights(ImageNumber,1)=sum(sum(bwlight));

    thrdark=0.5*graythresh(im_gray);
    bwdark=im2bw(im_gray,thrdark);
```

```

% sumdarks(ImageNumber,1)=sum(sum(~bwdark));

if sumlights(ImageNumber,1)<150
    results(ImageNumber,1:14)=zeros(1,14);
    zeroed(Z,1)=ImageNumber;
    Z=Z+1;
    ImageNumber
    continue
end

%% Test to see if I want to analyze it

[x(1:256,2),x(1:256,1)]=imhist(im_gray);
% y=sortrows(x,-2);
% cutoff=mean(y(1:4,1));
[maxval index]=max(x(:,2));
if x(index,1)<(1-graythresh(im_gray))*4+graythresh(im_gray)
    start=index;
    leftsum=0;
    rightsum=0;
    while x(start,2)>.1*maxval
        start=start-1;
        if start==0
            break
        end
        leftsum=leftsum+x(start,2);
    end
    [maxval index]=max(x(:,2));
    finish=index;
    while x(finish,2)>.1*maxval
        finish=finish+1;
        if finish>=255
            break
        end
        rightsum=rightsum+x(finish,2);
    end

    rightside=finish-index;
    leftside=index-start;
    difference=rightside-leftside;

    if difference>=20
        skipcount=skipcount+1;
        skipped(skipcount,1)=ImageNumber;
        results(ImageNumber,1:14)=1000*ones(1,14);
        ImageNumber
        continue
    end
end

%% The big parts

threshold=graythresh(im_gray)*.9;
ibw1=im2bw(im_gray,threshold);

```

```
%Automatic determination of flood fill start location
```

```
[B L]=bwboundaries(ibw1,4);  
[tempL tempnum1]=bwlabel(ibw1,4);  
% tempnumlowthresh  
Astats=regionprops(L,'Area');  
A=zeros(length(B),1);  
for i=1:length(B)  
    bound=B{i};  
    A(i,1)=Astats(i).Area;  
    A(i,2)=bound(1,1);  
    A(i,3)=bound(1,2);  
end  
A2=sortrows(A,-1);  
ibw1f=~ibw1;  
q=1;  
SizeA2=size(A2);  
loc=0;  
if SizeA2(1,1)>0  
    while A2(q,1)>10000 && SizeA2(1,1)>q  
        r=A2(q,2);  
        c=A2(q,3);  
        loc(q,1)=r;  
        loc(q,2)=c;  
        q=q+1;  
    end  
end  
if loc(1,1)~=0  
    ibw1f=imfill(ibw1f,loc,4);  
end  
ibw1f=imfill(~ibw1f,'holes');  
[tempL tempnumlowthresh]=bwlabel(ibw1f,4);  
countdrops(ImageNumber,1)=tempnumlowthresh;  
bigs=bwareaopen(ibw1f,250);  
[tempL tempnumbigs]=bwlabel(bigs,4);  
countdrops(ImageNumber,2)=tempnumbigs;
```

```
%circle finder on ibw1f
```

```
[B,L]=bwboundaries(bigs,8);  
stats=regionprops(L,'Area','Centroid','Perimeter');  
areas=zeros(length(B),1);  
dcount=1;  
dr=0;  
dc=0;  
for k=1:length(B)  
    A=stats(k).Area;  
    bound=B{k};  
    areas(k,1)=A;  
    R=sqrt(A/pi);  
    centroid=stats(k).Centroid;  
    npoints=32;  
    everynth=floor(length(bound)/npoints);  
    errorsum=0;  
    for j=1:npoints  
        i=everynth*j;
```

```

        if i==0
            i=1;
        end
        dist=sqrt((bound(i,1)-centroid(2))^2+(bound(i,2)-centroid(1))^2);
        errorsum=errorsum+(dist-R)^2/R^2;
    end
    error=errorsum/npoints;

    P=stats(k).Perimeter;
    roundness=4*A*pi/P^2;

    circlescore=roundness/error;

    if circlescore<5
        dr(dcount,1)=bound(1,1);
        dc(dcount,1)=bound(1,2);
        dcount=dcount+1;
        continue
    end
end
if dr~=0
    deleted=bwselect(bigs,dc,dr,8);
end
temp=bigs&~deleted;
[tempL tempnumbigscircles]=bwlabel(temp,4);
countdrops(ImageNumber,3)=tempnumbigscircles;

%% The small parts
% threshold=graythresh(im_gray)*1.1;
% if threshold>1
%     threshold=graythresh(im_gray);
% end
% ibw2=im2bw(im_gray,threshold);
%
% %Automatic determination of flood fill start location
% [B L]=bwboundaries(ibw2,4);
% Astats=regionprops(L,'Area');
% A=zeros(length(B),1);
% for i=1:length(B)
%     bound=B{i};
%     A(i,1)=Astats(i).Area;
%     A(i,2)=bound(1,1);
%     A(i,3)=bound(1,2);
% end
% A2=sortrows(A,-1);
% % ibw2f=~ibw2;
% ibw2f=ibw2;
% q=1;
% SizeA2=size(A2);
% loc=0;
% if SizeA2(1,1)>0
%     while A2(q,1)>10000 && SizeA2(1,1)>q
%         r=A2(q,2);
%         c=A2(q,3);
%         loc(q,1)=r;

```



```

%     loc(q,2)=c;
%     q=q+1;
%     end
% end
% if loc(1,1)~=0
%     ibw2f=imfill(ibw2f,loc,4);
%     end
%     ibw2f=imfill(~ibw2f,'holes');
%
% [L num]=bwlabel(ibw2f,4);
% stats2=regionprops(L,'Area','PixelList');
% dcount=1;
% dr=0;
% dc=0;
% for z=1:length(stats2)
%     A=stats2(z).Area;
%     PL=stats2(z).PixelList;
%     if A<20 || A>250
%         dc(dcount,1)=PL(1,1);
%         dr(dcount,1)=PL(1,2);
%         dcount=dcount+1;
%         continue
%     end
% end
% if dr~=0
%     deleted=bwselect(ibw2f,dc,dr,4);
%     end
%     ibw2f=ibw2f&~deleted;
%
% %circle finder on ibw2f
% [B,L]=bwboundaries(ibw2f,4);
% stats=regionprops(L,'Area','Centroid','Perimeter');
% temp2=ibw2f;
% areas=zeros(length(B),1);
% dcount=1;
% dr=0;
% dc=0;
% for k=1:length(B)
%     A=stats(k).Area;
%     bound=B{k};
%     areas(k,1)=A;
%     R=sqrt(A/pi);
%     centroid=stats(k).Centroid;
%     npoints=32;
%     everynth=floor(length(bound)/npoints);
%     errorsum=0;
%     for j=1:npoints
%         i=everynth*j;
%         if i==0
%             i=1;
%         end
%         dist=sqrt((bound(i,1)-centroid(2))^2+(bound(i,2)-centroid(1))^2);
%         errorsum=errorsum+(dist-R)^2/R^2;
%     end
%     error=errorsum/npoints;
%

```

```

%     P=stats(k).Perimeter;
%     roundness=4*A*pi/P^2;
%
%     circlescore=roundness/error;
%
%     if circlescore<20
%         dr(dcount,1)=bound(1,1);
%         dc(dcount,1)=bound(1,2);
%         dcount=dcount+1;
%         continue
%     end
% end
% if dr~=0
%     deleted=bwselect(ibw2f,dc,dr,4);
% end
%     temp2=ibw2f&~deleted;

%% The Light Parts
t=(1-graythresh(im_gray))*0.15+graythresh(im_gray);
bw=im2bw(im_gray,t);
[B L]=bwboundaries(bw,4);
[tempL tempnum5]=bwlabel(bw,4);
% tempnum5
Astats=regionprops(L,'Area');
A=zeros(length(B),1);
for i=1:length(B)
    bound=B{i};
    A(i,1)=Astats(i).Area;
    A(i,2)=bound(1,1);
    A(i,3)=bound(1,2);
end
A2=sortrows(A,-1);
bwf=~bw;
q=1;
SizeA2=size(A2);
loc=0;
if SizeA2(1,1)>0
    while A2(q,1)>10000 && SizeA2(1,1)>q
        r=A2(q,2);
        c=A2(q,3);
        loc(q,1)=r;
        loc(q,2)=c;
        q=q+1;
    end
end
if loc(1,1)~=0
    bwf=imfill(bwf,loc,4);
end
bwf=imfill(~bwf,'holes');
[tempL tempnumhighthresh]=bwlabel(bwf,4);
countdrops(ImageNumber,4)=tempnumhighthresh;
% intersection of light interiors and dark rings

iclear=bwf;%&ibw1f;

```

```

[tempL tempnum7]=bwlabel(iclear,4);
%tempnum7
deleted=zeros(S);
[B,L]=bwboundaries(iclear,4);
stats=regionprops(L,'Area','Centroid','Perimeter');
areas=zeros(length(B),1);
dcount=1;
dr=0;
dc=0;
for k=1:length(B)
    A=stats(k).Area;
    bound=B{k};
    areas(k,1)=A;
    R=sqrt(A/pi);
    centroid=stats(k).Centroid;
    npoints=32;
    everynth=floor(length(bound)/npoints);
    errorsum=0;
    for j=1:npoints
        i=everynth*j;
        if i==0
            i=1;
        end
        dist=sqrt((bound(i,1)-centroid(2))^2+(bound(i,2)-centroid(1))^2);
        errorsum=errorsum+(dist-R)^2/R^2;
    end
    error=errorsum/npoints;

    P=stats(k).Perimeter;
    roundness=4*A*pi/P^2;

    circlescore=roundness/error;

    if circlescore<12
        dr(dcount,1)=bound(1,1);
        dc(dcount,1)=bound(1,2);
        dcount=dcount+1;
        continue
    end
end
if dr~=0
    deleted=bwselect(iclear,dc,dr,4);
end
iclearer=iclear&~deleted;
[tempL tempnumhighthreshcircles]=bwlabel(iclearer,4);
countdrops(ImageNumber,5)=tempnumhighthreshcircles;

iclearer=iclearer&ibw1f;
[tempL tempnumintersected]=bwlabel(iclearer,4);
countdrops(ImageNumber,6)=tempnumintersected;

%
% close all
% imshow(iclearer);
% figure;imshow(deleted)

```

```

% figure;imshow(im_gray)

%% Finding 'Cells' that were mistaken as LDs
% iclearest=temp|(temp2&bwf);

cells=temp;
[L num]=bwlabel(cells,8);
stats3=regionprops(L,'Area','BoundingBox','PixelList','Solidity');
boxdilation=20;
fractions=zeros(num,1);
num1s=zeros(num,1);
num2s=zeros(num,1);
thrL=(1-graythresh(im_gray))*0.5+graythresh(im_gray);
bwL=im2bw(im_gray,thrL);
dcount=1;
dr=0;
dc=0;
Sol=zeros(num,1);
As=zeros(num,1);
score=zeros(num,1);
for p=1:num
    PL=stats3(p).PixelList;
    Sol(p,1)=stats3(p).Solidity;
    As(p,1)=stats3(p).Area;
%     BB=round(stats3(p).BoundingBox);
%     UL_col=BB(1);
%     UL_row=BB(2);
%     cols=BB(3);
%     rows=BB(4);
%
%     rowstart=UL_row-boxdilation;
%     rowend=UL_row+boxdilation+rows;
%     colstart=UL_col-boxdilation;
%     colend=UL_col+boxdilation+cols;
%     if rowstart<1
%         rowstart=1;
%     end
%     if rowend>S(1)
%         rowend=S(1);
%     end
%     if colstart<1
%         colstart=1;
%     end
%     if colend>S(2)
%         colend=S(2);
%     end
%
%     % how many other big objects are nearby?
%     boxbig=temp(rowstart:rowend,colstart:colend);
%     [L1 num1]=bwlabel(boxbig);
%     num1s(p,1)=num1;
%
%     % how many other total objects are nearby?
%     boxall=iclearest(rowstart:rowend,colstart:colend);
%     [L2 num2]=bwlabel(boxall);

```

```

% num2s(p,1)=num2;

% Look in light parts from beginning to see if it's a droplet
[i j]=find(L==p);
summer=0;
for n=1:length(i)
    summer=summer+im_gray(i(n),j(n));
end
fractions(p,1)=summer/length(i);

score(p,1)=fractions(p,1)/graythresh(im_gray)*Sol(p,1);

if score(p,1)<=1.26
    dc(dcount,1)=PL(1,1);
    dr(dcount,1)=PL(1,2);
    dcount=dcount+1;
end
end
if dr~=0
    cells=bwselect(cells,dc,dr,8);
else
    cells=zeros(S);
end
temp=temp&~cells;
[L3 bigsafterfilter]=bwlabel(temp);
countdrops(ImageNumber,7)=bigsafterfilter;

%% Combining Images

if sunlights(ImageNumber,1)<=500
    iclearest=iclearer&~bwareaopen(iclearer,400);
else
    iclearest=(temp|iclearer);
end

%% Results Output
[L,num]=bwlabel(iclearest,4);
finalcount=num;
countdrops(ImageNumber,8)=finalcount;

stats2=regionprops(round(L),'Area');
S=size(iclearest);

areas=zeros(num,1);
for i=1:num
    areas(i,1)=stats2(i).Area;
end
areas=sort(areas);

results(ImageNumber,1)=100*sum(sum(iclearest))/(S(1)*S(2)); % %of the image occupied by
LDs
summer=0;
z=1;
bins=zeros(1,11);

```

```

for i=1:num
    while areas(i)>hist(z)
        bins(1,z)=summer;
        z=z+1;
        summer=0;
    end
    summer=summer+4/3*pi*(areas(i)/pi)^1.5;
end
bins(1,z)=summer;
results(ImageNumber,14)=sum(bins);
if results(ImageNumber,14)~=0
    histresults=100*bins/results(ImageNumber,14);
    results(ImageNumber,3:13)=histresults;
    results(ImageNumber,2)=sum(sum(iclearest))/num; % Average LD size
end

n=1;
if mod(ImageNumber,n)==0
    images(1:S(1),1:S(2),ImageNumber/n)=im_gray;
    images(S(1)+1:2*S(1),1:S(2),ImageNumber/n)=iclear;
    images(1:S(1),S(2)+1:2*S(2),ImageNumber/n)=iclearest;
    images(S(1)+1:2*S(1),S(2)+1:2*S(2),ImageNumber/n)=temp;
end
ImageNumber
end
filenames=filenames';

acount=0;
cleanresults=zeros(length(filenames)-skipcount,14);
for imagenumber=1:length(filenames)
    if results(imagenumber,1)==1000
        continue
    else
        acount=acount+1;
        cleanresults(acount,1:14)=results(imagenumber,1:14);
        cleanfilenames(acount,1)=filenames(imagenumber,1);
    end
end

finaltime=clock;
finaltime-initialtime

```

## ***Appendix B: Solvent and Column Info for LC-MS/MS***

All columns were purchased from Phenomenex, Torrance, CA

HPLC-grade solvents and other components were purchased from Sigma.

### ***TCA Cycle/Glycolysis/Cofactors***

Column: Luna 5  $\mu\text{m}$  NH<sub>2</sub> 100 Å, LC column

Dimensions: 250 mm x 2.00 mm I.D.

Particles: 5  $\mu\text{m}$  particle size, 100 Å pore size

Solvent A: 20 mM ammonium hydroxide and 20 mM ammonium formate  
in 95:5 (v/v) water and acetonitrile, pH=9.5

Solvent B: 100% acetonitrile

### ***Amino Acids***

Column: Synergi 4u Fusion reverse phase (C18) column

Dimensions: 150 mm x 2.00 mm I.D.

Particles: 4  $\mu\text{m}$  particle size, 80 Å pore size

Solvent A: 0.1% Formic acid in water

Solvent B: 0.1% Formic acid in methanol

### ***Fatty Acids***

Column: Luna C8(2) reverse phase column

Dimensions: 150 mm x 2.00 mm I.D.

Particles: 3  $\mu\text{m}$  particle size, 100 Å pore size

Solvent A: 10 mM tributylamine and 15 mM acetic acid  
in 97:3 (v/v) water and methanol, pH=4.5

Solvent B: 100% methanol

## *Appendix C: Measured Metabolites (Individual Knockdown)*

Table 3: Intracellular Metabolite Concentrations

		Day 8				Day 14			
		FSP	DGAT	PCX	IDH	FSP	DGAT	PCX	IDH
Glycolysis	G6P	<b>-0.284</b>	<b>-0.242</b>	-0.054	<b>-0.382</b>	-0.060	-0.086	-0.214	-0.346
	F16BP	0.356	0.449	1.485	0.173	-0.335	-0.684	-0.555	-0.748
	R5P_X5P	<b>-0.380</b>	-0.082	-0.072	<b>-0.395</b>	-0.023	-0.175	-0.112	-0.186
	DHAP_GAP	<b>-0.236</b>	-0.066	0.183	<b>-0.113</b>	<b>-0.230</b>	<b>-0.327</b>	<b>-0.231</b>	<b>-0.220</b>
	PEP	<b>0.467</b>	<b>0.529</b>	0.201	0.021	-0.310	-0.374	-0.272	-0.364
TCA Cycle	OXA	<b>-0.322</b>	<b>-0.352</b>	0.150	0.333	-0.251	-0.246	-0.250	-0.256
	FUM	0.132	<b>0.239</b>	0.196	0.106	-0.151	-0.116	-0.236	-0.112
	MAL	0.170	<b>0.200</b>	0.170	0.081	-0.165	-0.088	-0.228	-0.125
	CIT_ISOCIT	0.637	0.729	1.190	0.006	-0.147	-0.250	-0.618	-0.494
	SUC	<b>0.439</b>	<b>0.434</b>	0.129	0.294	-0.055	-0.080	-0.083	0.103
	AKG	-0.149	-0.164	-0.124	-0.198	-0.166	-0.169	-0.200	-0.209
Amino Acids	Alanine	-0.670	-0.618	-0.078	-0.258	-0.251	-0.204	0.271	-0.039
	Aspartic Acid	-0.392	-0.803	-0.679	-0.471	0.007	-0.506	-0.421	0.034
	Cysteine	-0.758	-0.782	-0.486	-0.356	-0.611	-0.568	-0.324	-0.462
	Glutamate	-0.759	-0.754	-0.423	-0.449	-0.520	-0.308	0.009	-0.281
	Glycine	-0.649	-0.641	-0.196	-0.314	-0.516	-0.463	-0.211	-0.345
	Histidine	<b>-0.508</b>	-0.311	0.330	0.010	-0.359	-0.357	-0.161	-0.255
	Leu_Iso	-0.159	0.085	<b>0.939</b>	0.333	-0.162	0.060	0.342	0.216
	Methionine	-0.116	0.067	<b>1.072</b>	<b>0.411</b>	-0.188	-0.203	-0.059	0.043
	Proline	<b>-0.338</b>	<b>-0.296</b>	<b>0.591</b>	<b>0.352</b>	-0.178	-0.204	0.047	0.176
	Serine	-0.673	-0.569	-0.451	-0.285	-0.585	-0.526	-0.169	-0.287
	Threonine	-0.722	-0.667	-0.237	-0.297	-0.437	-0.352	-0.012	-0.262
	Tyrosine	-0.068	0.089	<b>1.035</b>	<b>0.414</b>	-0.191	-0.262	-0.002	0.026
	Valine	0.151	0.161	<b>1.305</b>	<b>0.707</b>	-0.168	<b>-0.309</b>	-0.091	-0.041
	Phenylalanine	-0.008	-0.009	<b>1.022</b>	<b>0.884</b>	-0.322	<b>-0.516</b>	<b>-0.485</b>	-0.340
	Asparagine	-0.779	-0.717	-0.264	-0.339	-0.315	-0.104	0.180	0.035
Tryptophan	0.047	0.135	<b>1.066</b>	<b>0.825</b>	-0.188	-0.224	-0.242	-0.193	
Fatty Acids	Oleic Acid	-0.129	-0.205	-0.308	-0.250	0.195	0.028	<b>-0.186</b>	<b>-0.157</b>
	Myristic Acid	0.182	0.157	-0.035	0.126	0.219	0.124	0.013	0.038
	Palmitic Acid	0.075	-0.003	<b>-0.174</b>	-0.040	-0.007	0.013	-0.049	-0.028
	Linoleic Acid	<b>-0.223</b>	<b>-0.340</b>	<b>-0.387</b>	0.912	0.230	0.434	0.054	0.164
	Stearic Acid	<b>0.095</b>	0.040	<b>-0.347</b>	-0.196	0.240	0.347	0.197	0.188
	Palmitoleic Acid	-0.118	-0.058	-0.470	-0.352	0.273	-0.080	-0.248	-0.168
	Arachidonic	-0.043	-0.006	-0.051	0.039	-0.185	-0.148	-0.249	-0.312

Expressed as a percent change from the control each respective time point.

Significant differences (p<0.05) are bold and highlighted.



Table 4: Extracellular Flux Measurements

		Day 8				Day 14			
		FSP	DGAT	PCX	IDH	FSP	DGAT	PCX	IDH
Amino Acids	Alanine	<b>-0.211</b>	-0.371	-0.125	-0.133	0.142	0.157	0.434	0.035
	Aspartic Acid	-0.044	0.009	-0.029	-0.178	0.084	0.068	0.008	<b>0.089</b>
	Cysteine	1.071	0.979	1.393	1.231	-0.263	<b>1.326</b>	1.105	0.284
	Glutamate	0.000	-0.013	-0.038	-0.294	<b>0.173</b>	0.122	-0.017	0.068
	Glycine	-0.159	-0.480	-0.462	0.023	0.252	0.071	0.592	0.443
	Histidine	0.699	1.452	<b>2.871</b>	1.753	<b>-1.392</b>	<b>-1.860</b>	<b>-1.532</b>	<b>-2.425</b>
	Leu Iso	<b>0.135</b>	<b>0.160</b>	0.062	<b>0.858</b>	-0.028	-0.138	<b>-0.146</b>	-0.113
	Methionine	3.833	4.625	9.125	7.438	-0.416	-0.241	-0.493	-0.177
	Proline	0.050	0.213	<b>0.334</b>	0.356	0.006	-0.315	-0.311	0.097
	Serine	-0.015	0.003	0.151	0.002	0.024	-0.058	-0.108	-0.069
	Threonine	0.765	0.487	1.160	0.584	0.469	-1.295	-2.250	-0.853
	Tyrosine	-0.259	-0.578	<b>-0.534</b>	-0.310	0.197	0.124	-0.255	0.599
	Valine	0.045	-0.008	-0.020	0.119	-0.035	-0.233	-0.110	-0.411
	Phenylalanine	-0.364	<b>-0.500</b>	-0.500	-0.523	-6.366	-8.805	-8.561	-7.341
	Asparagine	<b>-0.152</b>	-0.173	0.002	-0.084	-0.048	0.074	0.353	0.003
Tryptophan	0.006	-0.064	-0.038	-0.064	<b>-1.722</b>	<b>-1.375</b>	<b>-1.833</b>	<b>-2.347</b>	
Fatty Acids	Oleic Acid	0.881	0.762	0.571	1.000	-1.071	-1.786	-2.429	-0.929
	Myristic Acid	9.496	5.067	3.899	<b>13.395</b>	-0.619	-1.829	-1.285	-1.319
	Palmitic Acid	-4.595	-1.024	-1.929	<b>-3.738</b>	-0.514	-2.432	-0.703	-0.432
	Linoleic Acid	-0.002	<b>0.175</b>	<b>0.275</b>	-0.225	<b>-0.175</b>	-0.178	-0.011	-0.053
	Stearic Acid	-1.431	<b>-0.615</b>	-0.154	<b>-0.692</b>	-0.556	-1.833	-0.972	-1.028
	Palmitoleic	0.597	0.105	0.069	0.395	0.362	0.124	0.191	-0.199
	Arachidonic	0.005	-0.008	0.008	-0.038	-0.018	-0.013	-0.032	-0.008

Expressed as a percent change from the control each respective time point.

Significant differences ( $p < 0.05$ ) are bold and highlighted.

## Appendix D: Principal Component Analysis

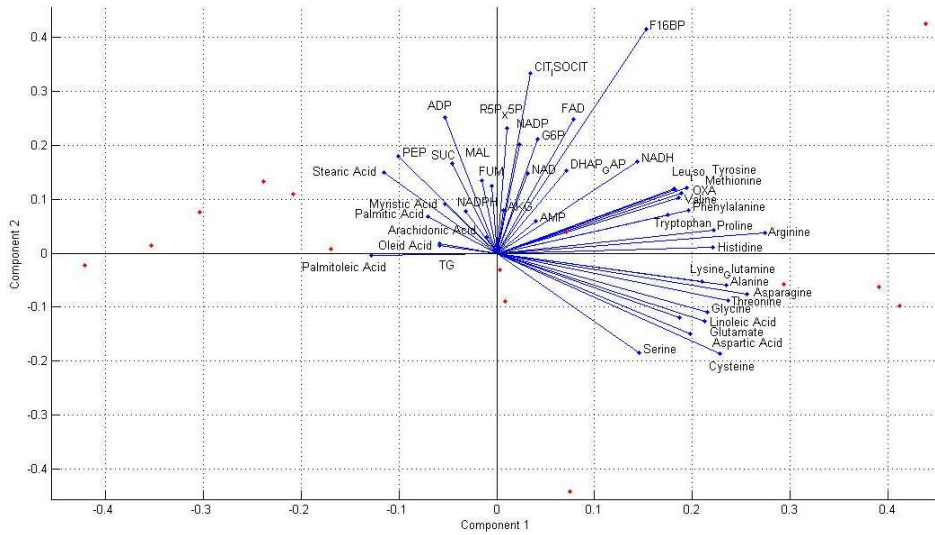


Figure S-0-1: Component Scores (Day 8)

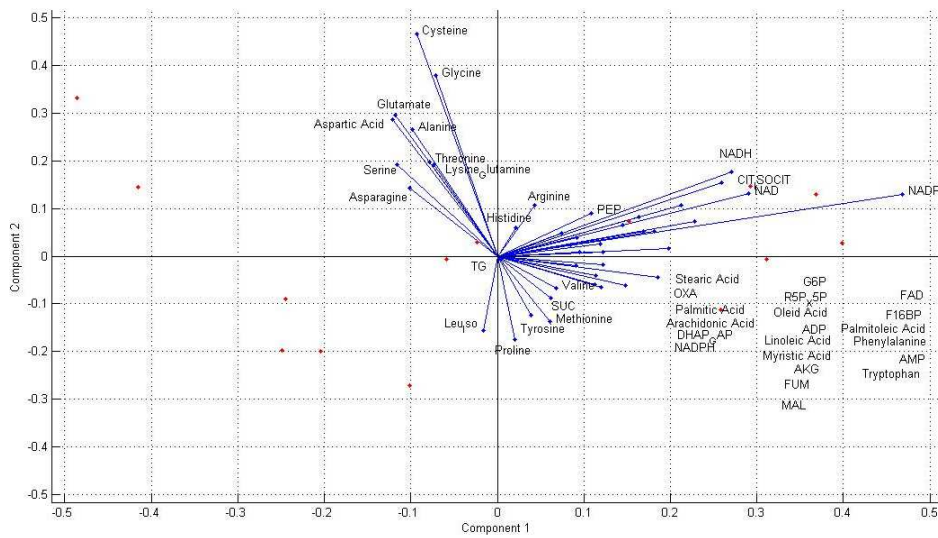


Figure S-0-2: Component Scores (Day 14)

## Appendix E: Hierarchical Clustering

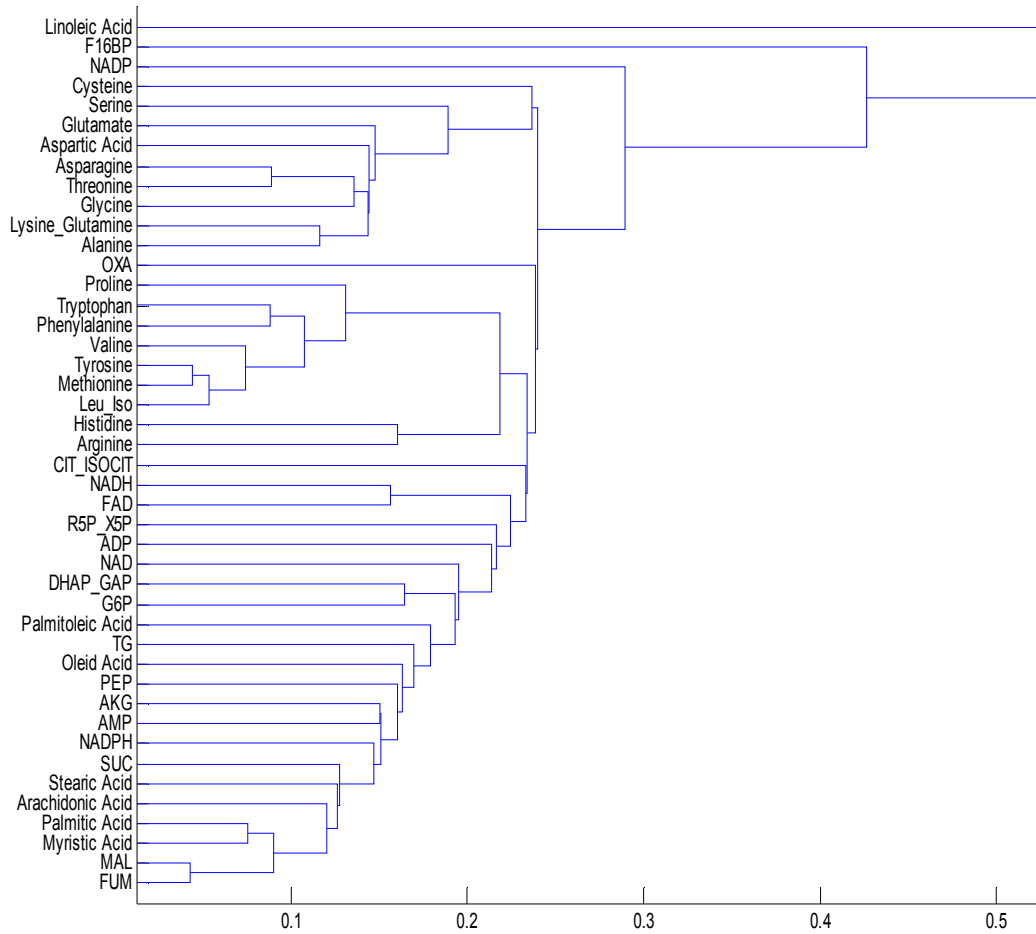


Figure S-0-1: Hierarchical Clustering of Metabolites (Day 8)

## Appendix F: Reaction stoichiometry of the model network

Table 5: Stoichiometric model for the adipocyte network

RXN	Pathway	Stoichiometry
1*	Glycolysis	<b>Glucose</b> = Glucose 6-P
2	Glycolysis	Glucose 6-P = Fructose 6-P
3	Glycolysis	Fructose 6-P = Glyceraldehyde 3-P + Glycerone-P
4	Glycolysis	Glycerone-P = Glyceraldehyde 3-P
5	Glycolysis	Glyceraldehyde 3-P = P-Enolpyruvate
6*	Glycolysis	P-Enolpyruvate = Pyruvate
7	Glycolysis	Pyruvate + NADH = <b>Lactate</b>
8	Pentose Phosphate Shunt	Glucose 6-P = Ribulose 5-P + CO <sub>2</sub> + 2 NADPH
9	Pentose Phosphate Shunt	3 Ribulose 5-P = 2 Fructose 6-P + Glyceraldehyde 3-P
10*	TCA cycle (mitochondria)	<b>Pyruvate + Oxaloacetate = Citrate</b> + CO <sub>2</sub> + NADH
11	TCA cycle (mitochondria)	<b>Pyruvate + CO<sub>2</sub> = Oxaloacetate</b>
12*	TCA cycle (mitochondria)	<b>Citrate = 2-Oxoglutarate</b> + CO <sub>2</sub> + NADH
13*	TCA cycle (mitochondria)	<b>2-Oxoglutarate = Succinyl-CoA</b> + CO <sub>2</sub> + NADH
14	TCA cycle (mitochondria)	<b>Succinyl-CoA = Fumarate</b> + FADH <sub>2</sub>
15	TCA cycle (mitochondria)	<b>Fumarate = Malate</b>
16	TCA cycle (mitochondria)	<b>Malate = Oxaloacetate</b> + NADH
17	TCA cycle	Citrate = Acetyl-CoA + Oxaloacetate
18*	TCA cycle	Oxaloacetate + NADH = Malate
19	TCA cycle	Malate = Pyruvate + CO <sub>2</sub> + NADPH
20	TCA cycle	Citrate = 2-Oxoglutarate + CO <sub>2</sub> + NADPH
21*	TCA cycle	Oxaloacetate = P-Enolpyruvate + CO <sub>2</sub>
22	Oxidative phosphorylation	NADH + 0.5 O <sub>2</sub> =
23	Oxidative phosphorylation	FADH <sub>2</sub> + 0.5 O <sub>2</sub> =
24	Palmitate biosynthesis	8 Acetyl-CoA + 14 NADPH = Palmitate
25*	TG biosynthesis	Glycerone-P + 3 Palmitate + NADH = Tripalmitoylglycerol
26*	TG biosynthesis	Tripalmitoylglycerol = <b>Glycerol</b> + 3 Palmitate
27	Ketone body metabolism	<b>2 Acetyl-CoA = Acetoacetate</b>
28	Ketone body metabolism	<b>Acetoacetyl-CoA = Acetoacetate</b>
29	Ketone body metabolism	<b>Acetoacetate + NADH = 3-Hydroxybutyrate</b>
30	Amino acid metabolism	Pyruvate + NH <sub>4</sub> <sup>+</sup> + NADPH = Alanine
31	Amino acid metabolism	Aspartate + NH <sub>4</sub> <sup>+</sup> = <b>Asparagine</b>
32	Amino acid metabolism	Aspartate = Oxaloacetate + NH <sub>4</sub> <sup>+</sup> + NADH
33*	Amino acid metabolism	Cysteine = Pyruvate + NH <sub>4</sub> <sup>+</sup> + NADH
34	Amino acid metabolism	Glutamate = 2-Oxoglutarate + NH <sub>4</sub> <sup>+</sup> + NADH
35	Amino acid metabolism	Glutamate + NH <sub>4</sub> <sup>+</sup> = <b>Glutamine</b>
36	Amino acid metabolism	Serine = Glycine
37*	Amino acid metabolism	<b>Histidine</b> = Glutamate + NH <sub>4</sub> <sup>+</sup>

38*	Amino acid metabolism	<b>Isoleucine</b> = <i>Succinyl-CoA</i> + <i>Acetyl-CoA</i>
39*	Amino acid metabolism	<b>Leucine</b> + CO <sub>2</sub> = <i>Acetoacetate</i> + <i>Acetyl-CoA</i>
40	Amino acid metabolism	<b>Lysine</b> = 2-Oxoadipate
41	Amino acid metabolism	2-Oxoadipate = <i>Acetoacetyl-CoA</i>
42*	Amino acid metabolism	<b>Methionine</b> + Serine = <i>Succinyl-CoA</i> + Cysteine
43*	Amino acid metabolism	<b>Phenylalanine</b> + O <sub>2</sub> + NADH = Tyrosine
44	Amino acid metabolism	Glutamate + 2 NADPH = <b>Proline</b>
45	Amino acid metabolism	Serine = Pyruvate + NH <sub>4</sub> <sup>+</sup>
46*	Amino acid metabolism	<b>Threonine</b> = Glycine + <i>Acetyl-CoA</i> + NADH
47*	Amino acid metabolism	<b>Tryptophan</b> = 2-Oxoadipate + Alanine
48*	Amino acid metabolism	Tyrosine + 2 O <sub>2</sub> = <i>Acetoacetate</i> + <i>Fumarate</i>
49*	Amino acid metabolism	<b>Valine</b> = <i>Succinyl-CoA</i>
50	Plasma exchange	Palmitate = <b>Palmitate</b>
51	Plasma exchange	<i>Acetoacetate</i> = <b>Acetoacetate</b>
52	Plasma exchange	Alanine = <b>Alanine</b>
53	Plasma exchange	<b>Aspartate</b> = Aspartate
54	Plasma exchange	<b>Cysteine</b> = Cysteine
55	Plasma exchange	<b>Glutamate</b> = Glutamate
56	Plasma exchange	Glycine = <b>Glycine</b>
57	Plasma exchange	<b>Serine</b> = Serine
58	Plasma exchange	<b>Tyrosine</b> = Tyrosine
59	Plasma exchange	<b>O<sub>2</sub></b> = O <sub>2</sub>
60	Plasma exchange	CO <sub>2</sub> = <b>CO<sub>2</sub></b>
61	Plasma exchange	NH <sub>4</sub> <sup>+</sup> = <b>NH<sub>4</sub><sup>+</sup></b>
62	Mitochondrial exchange	Pyruvate = <i>Pyruvate</i>
63	Mitochondrial exchange	<i>Citrate</i> = <b>Citrate</b>
64	Mitochondrial exchange	2-Oxoglutarate = <i>2-Oxoglutarate</i>
65	Mitochondrial exchange	<i>Malate</i> = <b>Malate</b>
66	TG Accumulation	Tripalmitoylglycerol = <b>Tripalmitoylglycerol</b>

Extracellular metabolites are indicated in **bold**. Mitochondrial metabolites are indicated in **bold italics**. Several entries in the table (e.g. reaction #10) represent pseudo-reactions obtained by condensing sequences of non-branching reactions. Starred reaction numbers indicate irreversible reactions (e.g. regulated steps of glycolysis, metabolism of essential amino acids, etc.). Many other reactions are assumed to only go in the forward direction (e.g. pentose phosphate pathway, glycolysis).

## Appendix G: Measured Metabolites (Double Knockdown)

Table 6: Intracellular Metabolite Concentrations (Double KD)

		Day 8	Day 14
Glycolysis	G6P	<b>-0.263</b>	-0.073
	F16BP	0.402	-0.510
	R5P_X5P	-0.231	-0.099
	DHAP_GAP	-0.151	<b>-0.279</b>
	PEP	<b>0.498</b>	<b>-0.342</b>
TCA Cycle	OXA	<b>-0.337</b>	<b>-0.249</b>
	FUM	<b>0.185</b>	-0.133
	MAL	<b>0.185</b>	-0.126
	CIT_ISOCIT	<b>0.683</b>	-0.199
	SUC	<b>0.436</b>	-0.068
	AKG	-0.156	-0.167
Amino Acids	Alanine	<b>-0.644</b>	-0.228
	Aspartic Acid	-0.597	-0.250
	Cysteine	-0.770	-0.590
	Glutamate	<b>-0.757</b>	-0.414
	Glycine	-0.645	-0.489
	Histidine	<b>-0.409</b>	<b>-0.358</b>
	Leu_Iso	-0.037	-0.051
	Methionine	-0.024	-0.195
	Proline	<b>-0.317</b>	-0.191
	Serine	-0.621	-0.556
	Threonine	-0.695	-0.395
	Tyrosine	0.010	<b>-0.226</b>
	Valine	0.156	<b>-0.238</b>
	Phenylalanine	-0.008	<b>-0.419</b>
	Asparagine	<b>-0.748</b>	-0.210
Tryptophan	0.091	-0.206	
Fatty Acids	Oleic Acid	-0.167	0.111
	Myristic Acid	<b>0.169</b>	<b>0.171</b>
	Palmitic Acid	0.036	0.003
	Linoleic Acid	<b>-0.281</b>	0.332
	Stearic Acid	<b>0.067</b>	<b>0.294</b>
	Palmitoleic Acid	-0.088	0.096
	Arachidonic Acid	-0.024	-0.166

Expressed as a percent change from the control each respective time point.

Significant differences ( $p < 0.05$ ) are bold and highlighted.

Table 7: Extracellular Flux Measurements (Double KD)

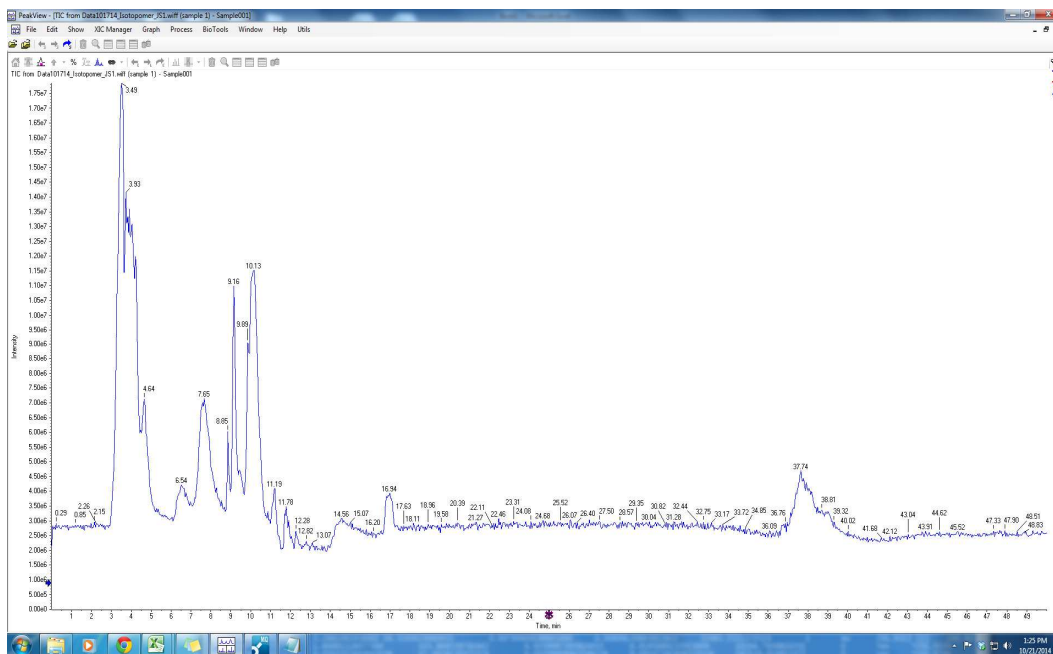
		Day 8	Day 14
Amino Acids	Alanine	-0.291	0.150
	Aspartic Acid	-0.018	<b>0.076</b>
	Cysteine	1.025	0.532
	Glutamate	-0.007	<b>0.148</b>
	Glycine	-0.319	0.162
	Histidine	1.075	<b>-1.626</b>
	Leu_Iso	<b>0.147</b>	-0.083
	Methionine	12.944	-0.329
	Proline	0.132	-0.154
	Serine	-0.006	-0.017
	Threonine	0.626	-0.413
	Tyrosine	-0.418	0.161
	Valine	0.018	-0.134
	Phenylalanine	<b>-0.432</b>	<b>-7.585</b>
	Asparagine	-0.163	0.013
	Tryptophan	-0.029	<b>-1.549</b>
Fatty Acids	Oleic Acid	<b>0.821</b>	-1.429
	Myristic Acid	1.986	-1.224
	Palmitic Acid	-2.810	-1.473
	Linoleic Acid	0.087	<b>-0.177</b>
	Stearic Acid	-1.023	-1.194
	Palmitoleic Acid	0.351	0.243
	Arachidonic Acid	-0.001	-0.016

Expressed as a percent change from the control each respective time point.

Significant differences ( $p < 0.05$ ) are bold and highlighted.

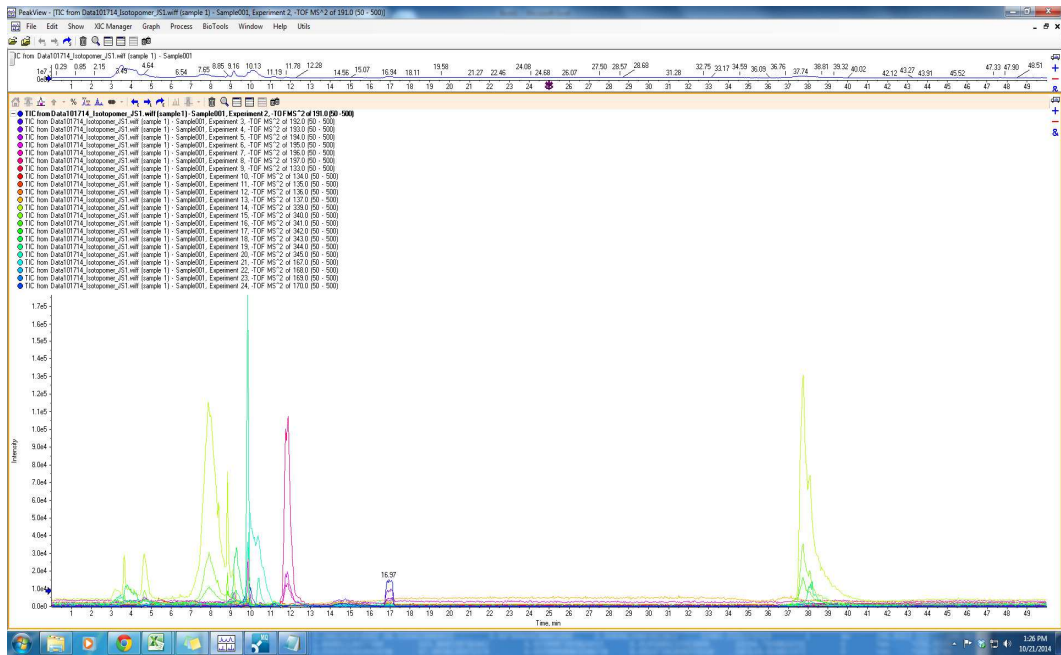
## Appendix H: Workflow for MID Measurements

In order to evaluate the MIDs of selected metabolites, we utilized a new LC-MS method. Briefly, we scanned for metabolites of interest and confirmed their identity based on fragmentation spectra. We simultaneously conducted product scans for each possible mass isotopomer ( $m+1$ ,  $m+2$ , etc.). Sample spectra are shown below.

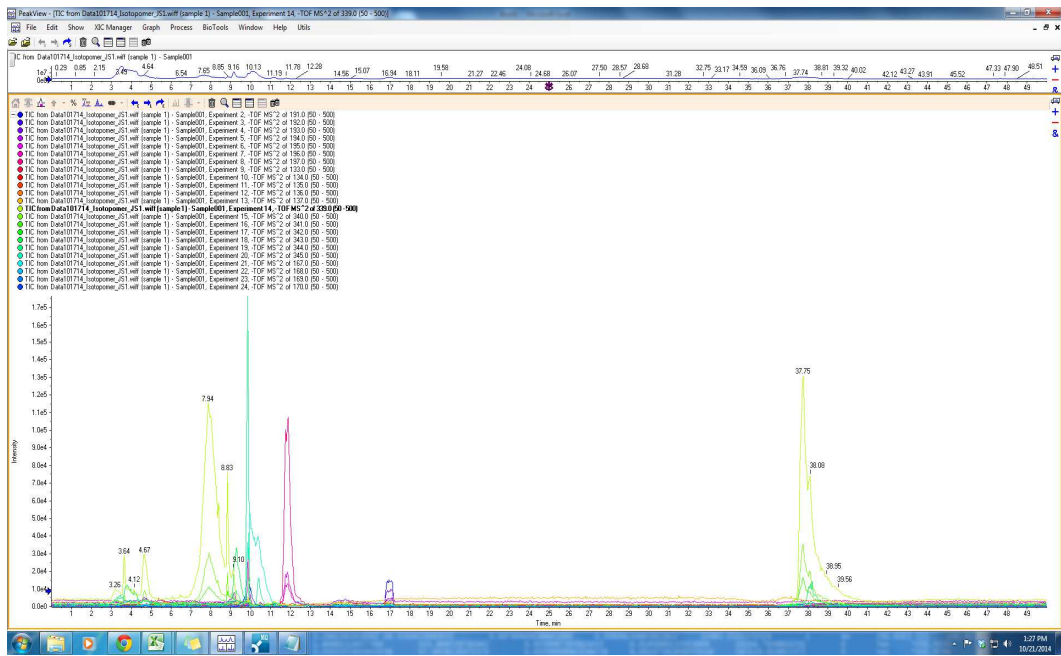


Total Ion Count for a representative sample.

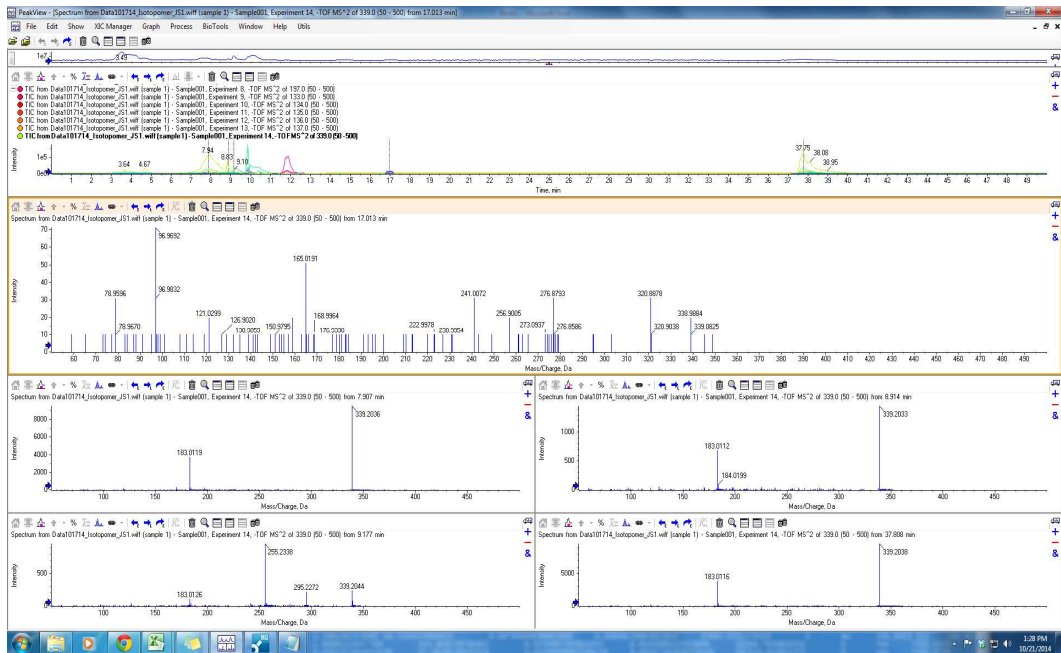




Extracted Ion Count (for each metabolite as well as isotopomers)

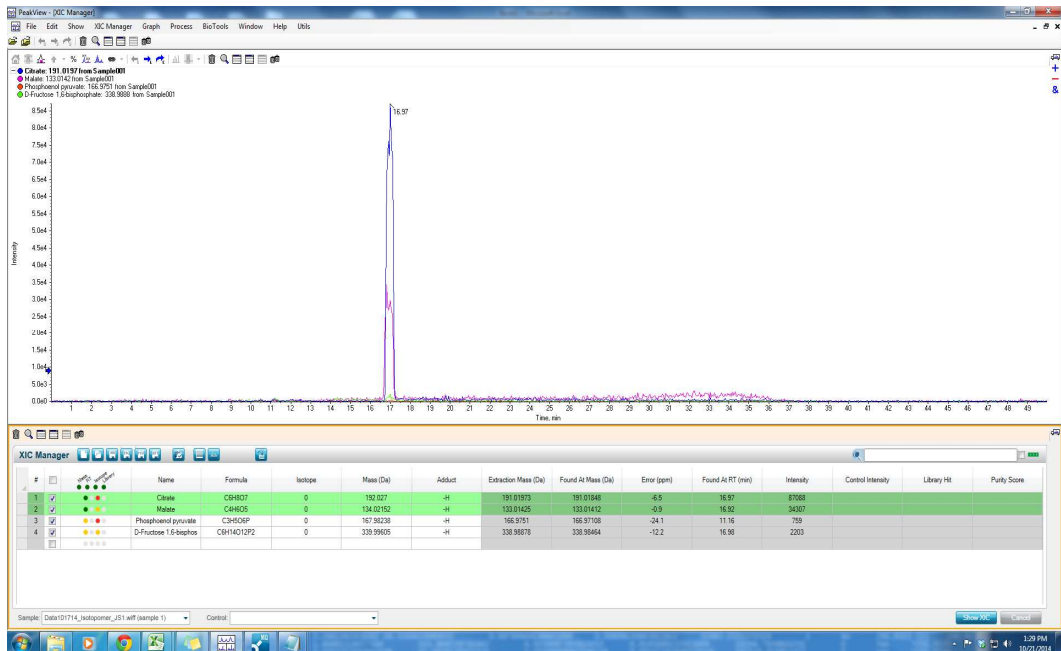


Selected XIC for Fructose 1,6 bisphosphate

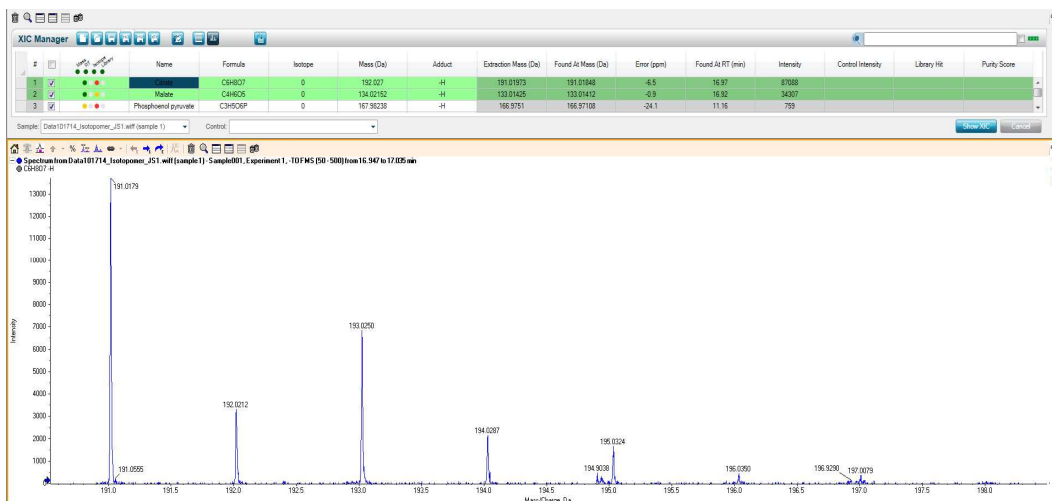


Fragmentation spectra for F16BP. Each spectra corresponds to a different peak.

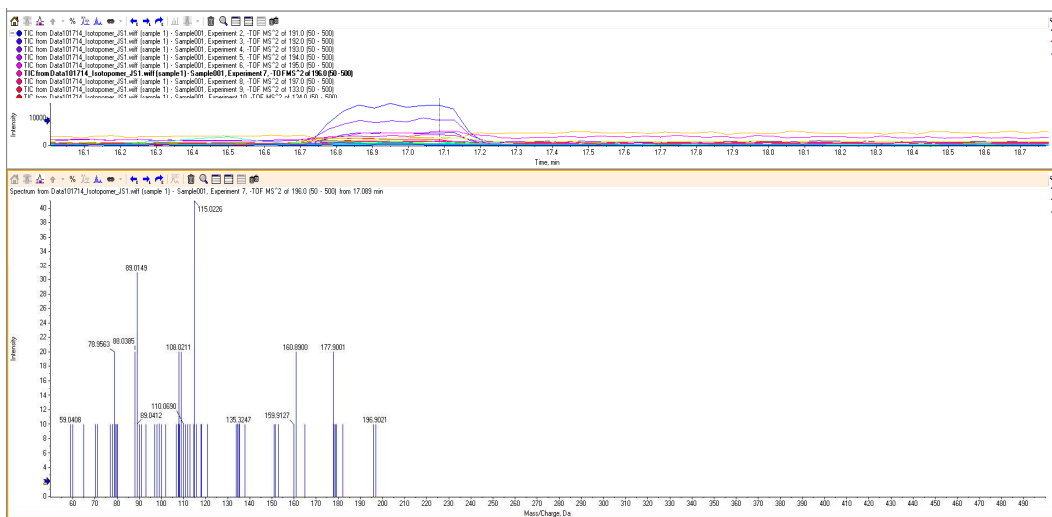
The correct peak was selected based on comparison of the fragmentation spectra to the Metlin Database.



After identifying the correct peaks, we can examine metabolites of interest (in this case, malate and citrate).



Within each peak, we examine the mass isotopomer distribution. Note: this feature is usually used to confirm peaks based on natural abundance of isotopes. However, in this case, from the distribution will not match natural abundance. Each peak corresponds to an isotopomer of citrate ( $m+1$ ,  $m+2$ , etc). From this plot, we can quantify the relative abundance of each isotopomer and then calculate the MID.



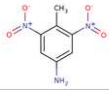
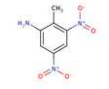
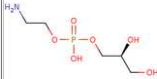
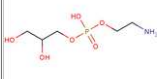
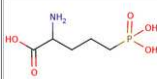
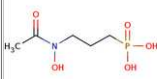
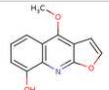
We can then examine the fragmentation spectra of isotopomers to confirm their identity. This plot shows the fragmentation of citrate ( $m+4$ ). Peaks within the spectra match expected peaks of citrate ( $m+0$ ) as well as enriched peaks.

METLIN  
Metabolites

Mass: 196.0356 with 30 ppm mass accuracy

[Change Query](#)

Total: 7 Metabolites

METLIN ID	MASS	Appm	NAME	MS/MS	STRUCTURE
71182 ...	[M-H] <sup>-</sup> m/z 196.0364 M 197.0437	3	4-Amino-2,6-dinitrotoluene Formula: C7H7N3O4 CAS: 19406-51-0	NO	
71183 ...	[M-H] <sup>-</sup> m/z 196.0364 M 197.0437	3	2-Amino-4,6-dinitrotoluene Formula: C7H7N3O4 CAS: 35572-78-2	NO	
98258 ...	[M-H2O-H] <sup>-</sup> m/z 196.0375 M 215.0559	9	sn-glycero-3-phosphoethanolamine Formula: C5H14NO6P CAS:	NO	
5151 ...	[M-H2O-H] <sup>-</sup> m/z 196.0375 M 215.0559	9	Glycerolphosphoethanolamine Formula: C5H14NO6P CAS:	NO	
69668 ...	[M-H] <sup>-</sup> m/z 196.0390 M 197.0453	12	2-Amino-5-phosphopentanoic acid Formula: C5H12NO5P CAS: 76226-31-3	NO	
63807 ...	[M-H] <sup>-</sup> m/z 196.0380 M 197.0453	12	FR 900038 Formula: C5H12NO5P CAS: 66508-32-6	NO	
68538 ...	[M-H2O-H] <sup>-</sup> m/z 196.0399 M 215.0582	21	Robustine Formula: C12H9NO3 CAS: 2255-50-7	NO	

Furthermore, we can mine the database for other compounds within the mass error range, to make sure the peaks could not be anything else. In this case, we search Metlin for compounds with the same mass as citrate (m+4), within an error of 30 ppm. There are several compounds with similar masses; however, it is clear that these particular compounds would not be present in a biological sample. When available, we examined the MS spectra for these compounds and compared them against the spectra of the compound of interest for further confirmation.

## *Appendix I: Mass Isotopomer Distributions*

Table 8: Mass Isotopomer Distribution (Double KD)

	Citrate			
	Day 8		Day 14	
	Control	KD	Control	KD
M+0	0.440	0.440	0.388	0.378
M+1	0.132	0.140	0.128	0.137
M+2	0.250	0.246	0.254	0.258
M+3	0.084	0.085	0.109	0.112
M+4	0.067	0.065	0.080	0.079
M+5	0.020	0.016	0.029	0.027
M+6	0.006	0.007	0.012	0.008

	Fumarate			
	Day 8		Day 14	
	Control	KD	Control	KD
M+0	0.386	0.428	0.430	0.349
M+1	0.171	0.133	0.154	0.163
M+2	0.257	0.266	0.252	0.240
M+3	0.080	0.089	0.094	0.140
M+4	0.106	0.084	0.070	0.109

	Malate			
	Day 8		Day 14	
	Control	KD	Control	KD
M+0	0.490	0.491	0.455	0.449
M+1	0.148	0.158	0.177	0.168
M+2	0.203	0.201	0.217	0.224
M+3	0.076	0.086	0.089	0.082
M+4	0.083	0.064	0.063	0.076

	Aspartate			
	Day 8		Day 14	
	Control	KD	Control	KD
M+0	0.498	0.499	0.459	0.461
M+1	0.128	0.112	0.119	0.116
M+2	0.181	0.185	0.210	0.195
M+3	0.119	0.125	0.159	0.154
M+4	0.074	0.080	0.054	0.073

MIDs are expressed as a percentage of the total metabolite pools. Values are self-normalized in the analysis. Data shown is the average of three biological replicates, though fluxes were calculated individually from each replicate.

## *Appendix J: Results of Isotopomer Model*

Table 9: Flux Estimates (Double KD)

RXN	Day 8			Day 14		
	Control	KD	%Diff	Control	KD	%Diff
1	371.690	340.028	<b>-0.085</b>	350.382	340.000	-0.030
2	189.214	171.045	<b>-0.096</b>	212.830	205.126	-0.036
3	310.865	283.701	<b>-0.087</b>	304.532	295.042	-0.031
4	289.171	251.449	<b>-0.130</b>	266.532	263.565	-0.011
5	660.861	591.477	<b>-0.105</b>	616.914	603.565	-0.022
6	660.861	591.477	<b>-0.105</b>	691.597	715.911	0.035
7	380.527	410.000	0.077	118.829	149.262	0.256
8	182.476	168.983	-0.074	137.552	134.874	-0.019
9	60.825	56.328	-0.074	45.851	44.958	-0.019
10	281.706	185.496	<b>-0.342</b>	489.796	439.395	-0.103
11	464.748	267.250	<b>-0.425</b>	464.433	504.005	0.085
12	0.000	0.000	-1.489	639.467	492.693	-0.230
13	196.414	139.344	-0.291	303.763	246.078	-0.190
14	202.420	146.214	-0.278	308.528	249.179	-0.192
15	205.158	149.154	-0.273	309.435	249.590	-0.193
16	-183.042	-81.754	<b>-0.553</b>	25.363	-64.610	-3.547
17	80.000	41.248	<b>-0.484</b>	176.000	178.667	0.015
18	79.875	41.150	<b>-0.485</b>	101.194	66.243	-0.345
19	468.075	272.059	<b>-0.419</b>	385.266	380.443	-0.013
20	201.706	144.248	-0.285	-325.671	-231.965	-0.288
21	0.000	0.000	-0.898	74.683	112.346	0.504
22	39.699	41.254	0.039	55.722	65.414	0.174
23	44.823	60.788	0.356	38.413	68.759	0.790
24	10.000	5.156	<b>-0.484</b>	22.000	22.333	0.015
25	21.694	32.251	0.487	38.000	31.477	-0.172
26	17.694	29.893	0.689	30.000	23.810	-0.206
27	2.071	2.366	<b>0.142</b>	2.118	2.204	0.041
28	1.590	2.100	0.321	1.373	1.278	<b>-0.070</b>
29	8.604	10.609	0.233	6.341	5.000	-0.211
30	3.541	2.881	<b>-0.186</b>	4.503	4.695	0.043
31	0.223	0.200	<b>-0.100</b>	0.205	0.168	<b>-0.183</b>
32	-0.125	-0.097	<b>-0.226</b>	-0.123	-0.078	<b>-0.366</b>
33	1.252	1.709	0.365	0.478	0.151	-0.683
34	-5.292	-4.904	-0.073	-10.033	-14.650	0.460
35	5.556	5.287	-0.048	9.770	14.545	0.489
36	-0.019	-0.126	<b>5.476</b>	-0.171	-0.578	<b>2.387</b>

RXN	Day 8			Day 14		
	Control	KD	%Diff	Control	KD	%Diff
37	0.049	0.086	<b>0.745</b>	0.050	0.042	-0.161
38	1.764	1.912	0.084	1.760	1.771	0.006
39	1.946	2.387	<b>0.227</b>	2.034	1.936	-0.048
40	0.475	1.000	1.106	1.000	1.000	0.000
41	1.590	2.100	0.321	1.373	1.278	<b>-0.070</b>
42	0.004	0.088	19.928	0.279	0.055	<b>-0.801</b>
43	3.402	3.086	-0.093	1.641	0.715	-0.564
44	0.176	0.166	-0.054	0.591	0.427	-0.277
45	0.335	0.382	0.140	0.220	0.851	<b>2.872</b>
46	0.433	0.433	0.001	0.442	0.702	<b>0.589</b>
47	1.115	1.100	-0.014	0.373	0.278	<b>-0.256</b>
48	2.738	2.940	0.074	0.907	0.412	-0.546
49	4.237	4.871	0.150	2.726	1.275	-0.532
50	-2.000	-1.920	-0.040	-2.000	-0.667	-0.667
51	-0.258	-0.817	2.165	0.092	0.829	8.047
52	4.656	3.981	<b>-0.145</b>	4.876	4.973	0.020
53	0.097	0.103	<b>0.062</b>	0.082	0.090	<b>0.092</b>
54	1.248	1.622	<b>0.299</b>	0.199	0.096	-0.518
55	0.391	0.464	<b>0.187</b>	0.278	0.280	0.006
56	0.413	0.307	<b>-0.257</b>	0.271	0.124	<b>-0.543</b>
57	0.320	0.343	<b>0.074</b>	0.328	0.329	<b>0.004</b>
58	-0.663	-0.146	<b>-0.780</b>	-0.734	-0.304	<b>-0.586</b>
59	69.227	53.899	-0.221	39.529	70.883	0.793
60	65.654	41.004	-0.375	42.371	66.725	0.575
61	27.484	41.099	0.495	33.192	43.641	0.315
62	746.455	452.746	<b>-0.393</b>	954.229	943.400	-0.011
63	281.706	185.496	<b>-0.342</b>	-149.671	-53.299	-0.644
64	196.414	139.344	-0.291	-335.704	-246.616	-0.265
65	388.200	230.908	-0.405	284.072	314.201	0.106
66	4.000	2.359	<b>-0.410</b>	8.000	7.667	-0.042

All units of flux are in mmol/g-DNA/2 days. Data shown are the means (n=3). Significant differences (p<0.05) are bold and highlighted. Reaction numbers refer to Table 5 in the Appendix.

Table 10: Glucose Normalized Fluxes (Double KD)

RXN	Day 8			Day 14		
	Control	KD	%Diff	Control	KD	%Diff
1	100.000	100.000	0.000	100.000	100.000	0.000
2	50.938	50.303	-0.012	60.788	60.331	-0.008
3	83.646	83.434	-0.003	86.929	86.777	-0.002
4	77.848	73.949	-0.050	76.066	77.519	0.019
5	177.848	173.949	-0.022	176.066	177.519	0.008
6	177.848	173.949	-0.022	197.635	210.562	0.065
7	102.601	120.578	0.175	34.209	43.901	0.283
8	49.062	49.697	0.013	39.212	39.669	0.012
9	16.354	16.566	0.013	13.071	13.223	0.012
10	75.639	54.553	-0.279	139.463	129.234	-0.073
11	124.762	78.597	<b>-0.370</b>	132.965	148.237	0.115
12	0.000	0.000	-1.546	179.917	144.910	-0.195
13	52.701	40.980	-0.222	86.273	72.376	-0.161
14	54.322	43.001	-0.208	87.626	73.288	-0.164
15	55.059	43.865	-0.203	87.882	73.409	-0.165
16	-49.123	-24.043	<b>-0.511</b>	6.498	-19.003	-3.924
17	21.531	12.131	<b>-0.437</b>	50.317	52.549	0.044
18	21.497	12.102	<b>-0.437</b>	28.712	19.483	-0.321
19	125.679	80.011	<b>-0.363</b>	110.096	111.895	0.016
20	54.108	42.423	-0.216	-90.771	-68.225	-0.248
21	0.000	0.000	-0.885	21.569	33.043	0.532
22	10.732	12.132	0.130	15.878	19.239	0.212
23	12.086	17.878	0.479	11.201	20.223	0.805
24	2.691	1.516	<b>-0.437</b>	6.290	6.569	0.044
25	5.798	9.485	0.636	10.864	9.258	-0.148
26	4.721	8.791	0.862	8.577	7.003	-0.183
27	0.558	0.696	<b>0.248</b>	0.605	0.648	0.071
28	0.431	0.618	0.432	0.393	0.376	-0.043
29	2.320	3.120	0.345	1.792	1.471	-0.179
30	0.953	0.847	<b>-0.111</b>	1.292	1.381	0.069
31	0.060	0.059	-0.017	0.059	0.049	<b>-0.160</b>
32	-0.034	-0.029	<b>-0.154</b>	-0.035	-0.023	<b>-0.348</b>
33	0.338	0.503	<b>0.488</b>	0.135	0.045	-0.670
34	-1.408	-1.442	0.024	-2.873	-4.309	0.500
35	1.479	1.555	0.051	2.797	4.278	0.529
36	-0.005	-0.037	<b>6.077</b>	-0.049	-0.170	<b>2.484</b>



RXN	Day 8			Day 14		
	Control	KD	%Diff	Control	KD	%Diff
37	0.013	0.025	<b>0.907</b>	0.014	0.012	-0.128
38	0.475	0.562	0.184	0.502	0.521	0.037
39	0.524	0.702	<b>0.339</b>	0.581	0.569	-0.021
40	0.131	0.294	1.242	0.286	0.294	0.029
41	0.431	0.618	0.432	0.393	0.376	-0.043
42	0.001	0.026	19.546	0.079	0.016	<b>-0.794</b>
43	0.915	0.908	-0.008	0.466	0.210	-0.549
44	0.047	0.049	0.034	0.170	0.126	-0.259
45	0.090	0.112	0.247	0.063	0.250	<b>2.966</b>
46	0.116	0.127	<b>0.094</b>	0.126	0.206	<b>0.634</b>
47	0.300	0.324	<b>0.078</b>	0.107	0.082	<b>-0.234</b>
48	0.737	0.865	0.173	0.256	0.121	-0.527
49	1.145	1.432	0.251	0.771	0.375	-0.513
50	-0.538	-0.565	0.049	-0.572	-0.196	-0.657
51	-0.069	-0.240	2.468	0.043	0.244	4.618
52	1.253	1.171	<b>-0.066</b>	1.399	1.463	0.046
53	0.026	0.030	<b>0.161</b>	0.023	0.026	<b>0.123</b>
54	0.337	0.477	<b>0.417</b>	0.056	0.028	-0.494
55	0.105	0.136	<b>0.297</b>	0.079	0.082	0.039
56	0.111	0.090	<b>-0.188</b>	0.077	0.036	<b>-0.530</b>
57	0.086	0.101	<b>0.174</b>	0.094	0.097	0.032
58	-0.178	-0.043	<b>-0.759</b>	-0.210	-0.089	<b>-0.576</b>
59	18.685	15.850	-0.152	11.034	20.848	0.889
60	17.615	12.059	-0.315	12.210	19.625	0.607
61	7.466	12.088	0.619	9.674	12.836	0.327
62	200.401	133.150	<b>-0.336</b>	272.428	277.470	0.019
63	75.639	54.553	-0.279	-40.454	-15.676	-0.612
64	52.701	40.980	-0.222	-93.644	-72.534	-0.225
65	104.183	67.909	-0.348	81.384	92.412	0.136
66	1.077	0.694	<b>-0.356</b>	2.287	2.255	-0.014

Data were normalized to the glucose uptake rate (RXN #1) for each condition.

Data shown are the means (n=3). Significant differences (p<0.05) are bold and highlighted. Reaction numbers refer to Table 5 in the Appendix.

## References

- Allen JW, Bhatia SN: Formation of steady-state oxygen gradients in vitro: application to liver zonation. *Biotechnol Bioeng* 2003, 82:253-262.
- Amantonico A, Urban PL, Fagerer SR, Balabin RM, Zenobi R: Single-cell MALDI-MS as an analytical tool for studying intrapopulation metabolic heterogeneity of unicellular organisms. *Anal Chem* 2010, 82:7394-7400.
- Amaral AI, Teixeira AP, Hakonsen BI, Sonnewald U, Alves PM: A comprehensive metabolic profile of cultured astrocytes using isotopic transient metabolic flux analysis and C-labeled glucose. *Front Neuroenergetics* 2011, 3:5.
- Antoniewicz MR, Kelleher JK, Stephanopoulos G. Elementary metabolite units (EMU): a novel framework for modeling isotopic distributions. *Metab Eng.* 2007 Jan;9(1):68-86.
- Avalos JL, Fink GR, Stephanopoulos G: Compartmentalization of metabolic pathways in yeast mitochondria improves the production of branched-chain alcohols. *Nat Biotechnol* 2013, 31:335-341.
- Barros LF, San Martin A, Sotelo-Hitschfeld T, Lerchundi R, Fernandez-Moncada I, Ruminot I, Gutierrez R, Valdebenito R, Ceballo S, Alegria K, et al.: Small is fast: astrocytic glucose and lactate metabolism at cellular resolution. *Front Cell Neurosci* 2013, 7:27.
- Bordbar A, Feist AM, Usaite-Black R, Woodcock J, Palsson BO, Famili I: A multi-tissue type genome-scale metabolic network for analysis of whole-body systems physiology. *BMC Syst Biol* 2011, 5:180.
- Bordbar A, Mo ML, Nakayasu ES, Schrimpe-Rutledge AC, Kim YM, Metz TO, Jones MB, Frank BC, Smith RD, Peterson SN, et al.: Model-driven multi-omic data analysis elucidates metabolic immunomodulators of macrophage activation. *Mol Syst Biol* 2012, 8:558.
- Bostrom P, Andersson L, Rutberg M, Perman J, Lidberg U, Johansson BR, et al. SNARE proteins mediate fusion between cytosolic lipid droplets and are implicated in insulin sensitivity. *Nature cell biology*.9:1286-93. 2007.
- Bouwman F, Renes J, Mariman E. A combination of protein profiling and isotopomer analysis using matrix-assisted laser desorption/ionization-time of flight mass spectrometry reveals an active metabolism of the extracellular matrix of 3T3-L1 adipocytes. *Proteomics* 2004, 4:3855–3863.
- Brasaemle DL. Thematic review series: adipocyte biology. The perilipin family of structural lipid droplet proteins: stabilization of lipid droplets and control of lipolysis. *J Lipid Res.* 2007 Dec;48(12):2547-59.
- Chatziioannou A, Palaiologos G, Kolisis FN: Metabolic flux analysis as a tool for the elucidation of the metabolism of neurotransmitter glutamate. *Metab Eng* 2003, 5:201-210.
- Chen HC, Farese RV Jr. Inhibition of triglyceride synthesis as a treatment strategy for obesity: lessons from DGAT1-deficient mice. *Arterioscler Thromb Vasc Biol.* 2005 Mar;25(3):482-6.

- Choi K-L, Wang Y, Tse CA, Lam KSL, Cooper GJS, Xu A. Proteomic analysis of adipocyte differentiation: Evidence that  $\alpha 2$  macroglobulin is involved in the adipose conversion of 3T3 L1 preadipocytes. *Proteomics* 2004, 4:1840–1848.
- Cinti S., Mitchell, G., Barbatelli, G., Murano, I., Ceresi, E., Faloia, E., Wang, S., Fortier, M., Greenberg, A.S., Obin, M.S.: Adipocyte death defines macrophage localization and function in adipose tissue of obese mice and humans. *J. Lipid Res.* **46**(11), 2347–2355 (2005).
- Crown SB, Ahn WS, Antoniewicz MR: Rational design of (1)(3)C-labeling experiments for metabolic flux analysis in mammalian cells. *BMC Syst Biol* 2012, 6:43.
- Dandekar T, Fieselman A, Majeed S, Ahmed Z: Software applications toward quantitative metabolic flux analysis and modeling. *Brief Bioinform* 2012.
- Davidson AJ, Ellis MJ, Chaudhuri JB: A theoretical approach to zonation in a bioartificial liver. *Biotechnol Bioeng* 2012, 109:234-243.
- Des Rosiers C, David F, Garneau M, Brunengraber H: Nonhomogeneous labeling of liver mitochondrial acetyl-CoA. *J Biol Chem* 1991, 266:1574-1578.
- Di Donato L, Des Rosiers C, Montgomery JA, David F, Garneau M, Brunengraber H: Rates of gluconeogenesis and citric acid cycle in perfused livers, assessed from the mass spectrometric assay of the  $^{13}\text{C}$  labeling pattern of glutamate. *J Biol Chem* 1993, 268:4170-4180.
- Edwards JS, Palsson BO: The Escherichia coli MG1655 in silico metabolic genotype: its definition, characteristics, and capabilities. *Proc Natl Acad Sci U S A* 2000, 97:5528-5533.
- Everts B, Amiel E, van der Windt GJ, Freitas TC, Chott R, Yarasheski KE, Pearce EL, Pearce EJ: Commitment to glycolysis sustains survival of NO-producing inflammatory dendritic cells. *Blood* 2012, 120:1422-1431.
- Feng, D., Tang, Y., Kwon, H., Zong, H., Hawkins, M., Kitsis, R.N., Pessin, J.E.: High-fat diet-induced adipocyte cell death occurs through a cyclophilin D intrinsic signaling pathway independent of adipose tissue inflammation. *Diabetes* **60**(8), 2134–2143 (2011).
- Fève B. Adipogenesis: cellular and molecular aspects. *Best Pract Res Clin Endocrinol Metab.* 2005 Dec;19(4):483-99.
- Foster LJ, Rudich A, Talior I, Patel N, Huang X, Furtado LM, Bilan PJ, Mann M, Klip A. Insulin-dependent interactions of proteins with GLUT4 revealed through stable isotope labeling by amino acids in cell culture (SILAC)\*. *J Proteome Res* 2005, 5:64–75.
- Freytag SO, Utter MF. Induction of pyruvate carboxylase apoenzyme and holoenzyme in 3T3-L1 cells during differentiation. *Proc Natl Acad Sci U S A.* 1980 Mar;77(3):1321-5.
- Fukumoto S, Fujimoto T. Deformation of lipid droplets in fixed samples. *Histochemistry and cell biology.* 118:423-8. 2002.
- Gille C, Bolling C, Hoppe A, Bulik S, Hoffmann S, Hubner K, Karlstadt A, Ganeshan R, Konig M, Rother K, et al.: HepatoNet1: a comprehensive metabolic reconstruction of the human hepatocyte for the analysis of liver physiology. *Mol Syst Biol* 2010, 6:411.

- Green H, Meuth M. An established pre-adipose cell line and its differentiation in culture. *Cell*. 1974;3:127-33.
- Griffin JL, Nicholls AW. Metabolomics as a functional genomic tool for understanding lipid dysfunction in diabetes, obesity and related disorders. *Pharmacogenomics*. 2006 Oct;7(7):1095-107.
- Harris CA, Haas JT, Streeper RS, Stone SJ, Kumari M, Yang K, Han X, Brownell N, Gross RW, Zechner R, Farese RV Jr. DGAT enzymes are required for triacylglycerol synthesis and lipid droplets in adipocytes. *J Lipid Res*. 2011 Apr;52(4):657-67.
- Haschemi A, Kosma P, Gille L, Evans CR, Burant CF, Starkl P, Knapp B, Haas R, Schmid JA, Jandl C, et al.: The sedoheptulose kinase CARKL directs macrophage polarization through control of glucose metabolism. *Cell Metab* 2012, 15:813-826.
- Hayashi S, Yoshida M, Fujiwara T, Maegawa S, Fukusaki E: Single-embryo metabolomics and systematic prediction of developmental stage in zebrafish. *Z Naturforsch C* 2011, 66:191-198.
- Hou BH, Takanaga H, Grossmann G, Chen LQ, Qu XQ, Jones AM, Lalonde S, Schweissgut O, Wiechert W, Frommer WB: Optical sensors for monitoring dynamic changes of intracellular metabolite levels in mammalian cells. *Nat Protoc* 2011, 6:1818-1833.
- Huo YX, Cho KM, Rivera JG, Monte E, Shen CR, Yan Y, Liao JC: Conversion of proteins into biofuels by engineering nitrogen flux. *Nat Biotechnol* 2011, 29:346-351.
- Ibanez AJ, Fagerer SR, Schmidt AM, Urban PL, Jefimovs K, Geiger P, Dechant R, Heinemann M, Zenobi R: Mass spectrometry-based metabolomics of single yeast cells. *Proc Natl Acad Sci U S A* 2013, 110:8790-8794.
- Isomaki A, Sillat T, Ainola M, Liljestrom M, Konttinen YT, Hukkanen M. Label-free imaging of adipogenesis by coherent anti-stokes Raman scattering microscopy. *Methods in molecular biology*. 1142:189-201. 2014.
- Jazmin LJ, Young JD: Isotopically nonstationary <sup>13</sup>C metabolic flux analysis. *Methods Mol Biol* 2013, 985:367-390.
- Jitrapakdee S, Slawik M, Medina-Gomez G, Campbell M, Wallace JC, Sethi JK, O'rahilly S, Vidal-Puig AJ. The peroxisome proliferator-activated receptor-gamma regulates murine pyruvate carboxylase gene expression in vivo and in vitro. *J Biol Chem*. 2005 Jul 22;280(29):27466-76.
- Kamei, N., Tobe, K., Suzuki, R., Ohsugi, M., Watanabe, T., Kubota, N., Ohtsuka-Kowatari, N., Kumagai, K., Sakamoto, K., Kobayashi, M., Yamauchi, T., Ueki, K., Oishi, Y., Nishimura, S., Manabe, I., Hashimoto, H., Ohnishi, Y., Ogata, H., Tokuyama, K., Tsunoda, M., Ide, T., Murakami, K., Nagai, R., Kadowaki, T.: Overexpression of monocyte chemoattractant protein-1 in adipose tissues causes macrophage recruitment and insulin resistance. *J. Biol. Chem.* **281**(36), 26602–26614 (2006).
- Koh HJ, Lee SM, Son BG, Lee SH, Ryoo ZY, Chang KT, Park JW, Park DC, Song BJ, Veech RL, Song H, Huh TL. Cytosolic NADP<sup>+</sup>-dependent isocitrate dehydrogenase plays a key role in lipid metabolism. *J Biol Chem*. 2004 Sep 17;279(38):39968-74.

- Konig M, Holzhutter HG, Berndt N: Metabolic Gradients as Key Regulators in Zonation of Tumor Energy Metabolism: A Tissue-scale Model Based Study. *Biotechnol J* 2013.
- Kovsan J, Ben-Romano R, Souza SC, Greenberg AS, Rudich A. Regulation of adipocyte lipolysis by degradation of the perilipin protein: nelfinavir enhances lysosome-mediated perilipin proteolysis. *J Biol Chem.* 2007 Jul 27;282(30):21704-11.
- Krauss M, Schaller S, Borchers S, Findeisen R, Lippert J, Kuepfer L: Integrating cellular metabolism into a multiscale whole-body model. *PLoS Comput Biol* 2012, 8:e1002750.
- Kuerschner L, Moessinger C, Thiele C. Imaging of lipid biosynthesis: how a neutral lipid enters lipid droplets. *Traffic*.9:338-52. 2008.
- Lai N, Jayaraman A, Lee K. Enhanced proliferation of human umbilical vein endothelial cells and differentiation of 3T3-L1 adipocytes in coculture. *Tissue Eng Part A.* 2009 May;15(5):1053-61.
- Lai N, Sims JK, Jeon NL, Lee K. Adipocyte induction of preadipocyte differentiation in a gradient chamber. *Tissue engineering Part C, Methods.*18:958-67. 2012.
- Lapidot A, Gopher A: Cerebral metabolic compartmentation. Estimation of glucose flux via pyruvate carboxylase/pyruvate dehydrogenase by <sup>13</sup>C NMR isotopomer analysis of D-[U-<sup>13</sup>C]glucose metabolites. *J Biol Chem* 1994, 269:27198-27208.
- Laurencikiene, J., Skurk, T., Kulyte, A., Heden, P., Astrom, G., Sjolin, E., Ryden, M., Hauner, H., Arner, P.: Regulation of lipolysis in small and large fat cells of the same subject. *J. Clin. Endocrinol. Metab.* **96**(12), E2045–E2049 (2011).
- Le TT, Cheng JX. Single-cell profiling reveals the origin of phenotypic variability in adipogenesis. *PloS one.*4:e5189. 2009.
- Lee K, Berthiaume F, Stephanopoulos GN, Yarmush ML: Profiling of dynamic changes in hypermetabolic livers. *Biotechnol Bioeng* 2003, 83:400-415.
- Lee, K. Kuo, CK. Extracellular Matrix Remodeling and Mechanical Stresses as Modulators of Adipose Tissue Metabolism and Inflammation. *The Mechanobiology of Obesity and Related Diseases. Studies in Mechanobiology, Tissue Engineering and Biomaterials Volume 16*, 2015, 105-122.
- Lligona-Trulla L, Arduini A, Aldaghlis TA, Calvani M, Kelleher JK: Acetyl-L-carnitine flux to lipids in cells estimated using isotopomer spectral analysis. *J Lipid Res* 1997, 38:1454-1462.
- Loo LH, Lin HJ, Singh DK, Lyons KM, Altschuler SJ, Wu LF. Heterogeneity in the physiological states and pharmacological responses of differentiating 3T3-L1 preadipocytes. *J Cell Biol.*187:375-84. 2009.
- Lumeng, C.N., Bodzin, J.L., Saltiel, A.R.: Obesity induces a phenotypic switch in adipose tissue macrophage polarization. *J. Clin. Investig.***117**(1), 175–184 (2007).
- Lumeng, C.N., DelProposto, J.B., Westcott, D.J., Saltiel, A.R.: Phenotypic switching of adipose tissue macrophages with obesity is generated by

- spatiotemporal differences in macrophage subtypes. *Diabetes* **57**(12), 3239–3246 (2008).
- MacDougald OA, Lane MD. Transcriptional regulation of gene expression during adipocyte differentiation. *Annu Rev Biochem.* 1995;64:345-73.
- Mahadevan R, Schilling CH: The effects of alternate optimal solutions in constraint-based genome-scale metabolic models. *Metab Eng* 2003, 5:264-276.
- Maier K, Hofmann U, Bauer A, Niebel A, Vacun G, Reuss M, Mauch K: Quantification of statin effects on hepatic cholesterol synthesis by transient (13)C-flux analysis. *Metab Eng* 2009, 11:292-309.
- Manteiga S, Choi K, Jayaraman A, Lee K. Systems biology of adipose tissue metabolism: regulation of growth, signaling and inflammation. *Wiley Interdiscip Rev Syst Biol Med.* 2013 Jul-Aug;5(4):425-47.
- Mantovani A, Biswas SK, Galdiero MR, Sica A, Locati M: Macrophage plasticity and polarization in tissue repair and remodelling. *J Pathol* 2013, 229:176-185.
- Marcinkiewicz A, Gauthier D, Garcia A, Brasaemle DL. The phosphorylation of serine 492 of perilipin a directs lipid droplet fragmentation and dispersion. *The Journal of biological chemistry.*281:11901-9. 2006.
- Martin S, Parton RG. Lipid droplets: a unified view of a dynamic organelle. *Nat Rev Mol Cell Biol.* 2006 May;7(5):373-8.
- Mathis D, Shoelson SE: Immunometabolism: an emerging frontier. *Nat Rev Immunol* 2011, 11:81
- Mattila I, Seppänen-Laakso T, Suortti T, Oresic M. Application of lipidomics and metabolomics to the study of adipose tissue. *Methods Mol Biol.* 2008;456:123-30
- Maumus M, Sengenès C, Decaunes P, Zakaroff-Girard A, Bourlier V, Lafontan M, et al. Evidence of in situ proliferation of adult adipose tissue-derived progenitor cells: influence of fat mass microenvironment and growth. *The Journal of clinical endocrinology and metabolism.*93:4098-106. 2008.
- Mehlem A, Hagberg CE, Muhl L, Eriksson U, Falkevall A. Imaging of neutral lipids by oil red O for analyzing the metabolic status in health and disease. *Nature protocols.*8:1149-54. 2013.
- Miccheli A, Tomassini A, Puccetti C, Valerio M, Peluso G, Tuccillo F, Calvani M, Manetti C, Conti F: Metabolic profiling by 13C-NMR spectroscopy: [1,2-13C2]glucose reveals a heterogeneous metabolism in human leukemia T cells. *Biochimie* 2006, 88:437-448.
- Mitrou, P., Boutati, E., Lambadiari, V., Maratou, E., Komesidou, V., Papakonstantinou, A., Sidossis, L., Tountas, N., Katsilambros, N., Economopoulos, T., Raptis, S.A., Dimitriadis, G.: Rates of lipid fluxes in adipose tissue in vivo after a mixed meal in morbid obesity. *Int. J. Obes.***34**(4), 770–774 (2010).
- Mueller D, Heinzle E: Stable isotope-assisted metabolomics to detect metabolic flux changes in mammalian cell cultures. *Curr Opin Biotechnol* 2013, 24:54-59.

- Nagayama M, Uchida T, Gohara K. Temporal and spatial variations of lipid droplets during adipocyte division and differentiation. *Journal of lipid research*.48:9-18. 2007.
- Nan X, Cheng JX, Xie XS. Vibrational imaging of lipid droplets in live fibroblast cells with coherent anti-Stokes Raman scattering microscopy. *Journal of lipid research*.44:2202-8. 2003.
- Nemes P, Knolhoff AM, Rubakhin SS, Sweedler JV: Metabolic differentiation of neuronal phenotypes by single-cell capillary electrophoresis-electrospray ionization-mass spectrometry. *Anal Chem* 2011, 83:6810-6817.
- Newton BW, Cologna SM, Moya C, Russell DH, Russell WK, Jayaraman A. Proteomic analysis of 3T3-L1 adipocyte mitochondria during differentiation and enlargement. *J Proteome Res* 2011, 10:4692–4702.
- Nguyen, M.T., Faveyukis, S., Nguyen, A.K., Reichart, D., Scott, P.A., Jenn, A., Liu-Bryan, R., Glass, C.K., Neels, J.G., Olefsky, J.M.: A subpopulation of macrophages infiltrates hypertrophic adipose tissue and is activated by free fatty acids via Toll-like receptors 2 and 4 and JNK-dependent pathways. *J. Biol. Chem.* **282**(48), 35279–35292 (2007).
- Niklas J, Noor F, Heinzle E: Effects of drugs in subtoxic concentrations on the metabolic fluxes in human hepatoma cell line Hep G2. *Toxicol Appl Pharmacol* 2009, 240:327-336.
- Nishino N, Tamori Y, Tateya S, Kawaguchi T, Shibakusa T, Mizunoya W, Inoue K, Kitazawa R, Kitazawa S, Matsuki Y, Hiramatsu R, Masubuchi S, Omachi A, Kimura K, Saito M, Amo T, Ohta S, Yamaguchi T, Osumi T, Cheng J, Fujimoto T, Nakao H, Nakao K, Aiba A, Okamura H, Fushiki T, Kasuga M. FSP27 contributes to efficient energy storage in murine white adipocytes by promoting the formation of unilocular lipid droplets. *J Clin Invest.* 2008 Aug;118(8):2808-21.
- Nolan RP, Fenley AP, Lee K. Identification of distributed metabolic objectives in the hypermetabolic liver by flux and energy balance analysis. *Metab Eng.* 2006 Jan;8(1):30-45.
- Nye C, Kim J, Kalhan SC, Hanson RW. Reassessing triglyceride synthesis in adipose tissue. *Trends Endocrinol Metab.* 2008 Dec;19(10):356-61.
- Or-Tzadikario S, Sopher R, Gefen A. Quantitative monitoring of lipid accumulation over time in cultured adipocytes as function of culture conditions: toward controlled adipose tissue engineering. *Tissue engineering Part C, Methods*.16:1167-81. 2010.
- Orman MA, Arai K, Yarmush ML, Androulakis IP, Berthiaume F, Ierapetritou MG: Metabolic flux determination in perfused livers by mass balance analysis: effect of fasting. *Biotechnol Bioeng* 2010, 107:825-835.
- Orman MA, Berthiaume F, Androulakis IP, Ierapetritou MG: Advanced stoichiometric analysis of metabolic networks of mammalian systems. *Crit Rev Biomed Eng* 2011, 39:511-534.
- Otsu N. Threshold Selection Method from Gray-Level Histograms. *Ieee T Syst Man Cyb.*9:62-6. 1979.

- Peregrin-Alvarez JM, Sanford C, Parkinson J: The conservation and evolutionary modularity of metabolism. *Genome Biol* 2009, 10:R63.
- Pol A, Gross SP, Parton RG. Review: biogenesis of the multifunctional lipid droplet: lipids, proteins, and sites. *J Cell Biol*.204:635-46. 2014.
- Puri V, Konda S, Ranjit S, Aouadi M, Chawla A, Chouinard M, Chakladar A, Czech MP. Fat-specific protein 27, a novel lipid droplet protein that enhances triglyceride storage. *J Biol Chem*. 2007 Nov 23;282(47):34213-8.
- Quinn KP, Bellas E, Furligas N, Lee K, Kaplan DL, Georgakoudi I: Characterization of metabolic changes associated with the functional development of 3D engineered tissues by non-invasive, dynamic measurement of individual cell redox ratios. *Biomaterials* 2012, 33:5341-5348.
- Ramirez-Zacarias JL, Castro-Munozledo F, Kuri-Harcuch W. Quantitation of adipose conversion and triglycerides by staining intracytoplasmic lipids with Oil red O. *Histochemistry*.97:493-7. 1992.
- Reid B, Afzal J, McCartney A, Abraham R, O'Rourke B, Elisseeff J: Enhanced tissue production through redox control in stem cell-laden hydrogels. *Tissue Eng Part A* 2013.
- Rinia HA, Burger KN, Bonn M, Muller M. Quantitative label-free imaging of lipid composition and packing of individual cellular lipid droplets using multiplex CARS microscopy. *Biophysical journal*.95:4908-14. 2008.
- Rodriguez PC, Yee DJ, Sames D: Expanding the use of fluorogenic enzyme reporter substrates to imaging metabolic flux changes: the activity measurement of 5 $\alpha$ -steroid reductase in intact mammalian cells. *ACS Chem Biol* 2010, 5:1045-1052.
- Rodriguez-Prados JC, Traves PG, Cuenca J, Rico D, Aragonés J, Martín-Sanz P, Cascante M, Bosca L: Substrate fate in activated macrophages: a comparison between innate, classic, and alternative activation. *J Immunol* 2010, 185:605-614.
- Rosen ED, Spiegelman BM. Molecular regulation of adipogenesis. *Annu Rev Cell Dev Biol*. 2000;16:145-71.
- Rubakhin SS, Romanova EV, Nemes P, Sweedler JV: Profiling metabolites and peptides in single cells. *Nat Methods* 2011, 8:S20-29.
- Rubakhin SS, Lanni EJ, Sweedler JV: Progress toward single cell metabolomics. *Curr Opin Biotechnol* 2013, 24:95-104.
- Ruhl M, Rupp B, Noh K, Wiechert W, Sauer U, Zamboni N: Collisional fragmentation of central carbon metabolites in LC-MS/MS increases precision of (1)(3)C metabolic flux analysis. *Biotechnol Bioeng* 2012, 109:763-771.
- San Martín A, Ceballos S, Ruminot I, Lerchundi R, Frommer WB, Barros LF: A genetically encoded FRET lactate sensor and its use to detect the Warburg effect in single cancer cells. *PLoS One* 2013, 8:e57712.
- Schilling CH, Palsson BO: The underlying pathway structure of biochemical reaction networks. *Proc Natl Acad Sci U S A* 1998, 95:4193-4198.
- Schroeder MA, Atherton HJ, Ball DR, Cole MA, Heather LC, Griffin JL, Clarke K, Radda GK, Tyler DJ: Real-time assessment of Krebs cycle metabolism using hyperpolarized <sup>13</sup>C magnetic resonance spectroscopy. *FASEB J* 2009, 23:2529-2538.



- Sharma NS, Nagrath D, Yarmush ML: Metabolic profiling based quantitative evaluation of hepatocellular metabolism in presence of adipocyte derived extracellular matrix. *PLoS One* 2011, 6:e20137.
- Shaw AJ, Podkaminer KK, Desai SG, Bardsley JS, Rogers SR, Thorne PG, Hogsett DA, Lynd LR: Metabolic engineering of a thermophilic bacterium to produce ethanol at high yield. *Proc Natl Acad Sci U S A* 2008, 105:13769-13774.
- Shen J, Petersen KF, Behar KL, Brown P, Nixon TW, Mason GF, Petroff OA, Shulman GI, Shulman RG, Rothman DL: Determination of the rate of the glutamate/glutamine cycle in the human brain by in vivo <sup>13</sup>C NMR. *Proc Natl Acad Sci U S A* 1999, 96:8235-8240.
- Shen, W.J., Yu, Z., Patel, S., Jue, D., Liu, L.F., Kraemer, F.B.: Hormone-sensitive lipase modulates adipose metabolism through PPARgamma. *Biochim. Biophys. Acta* **1811**(1), 9–16 (2011).
- Shi, H. Transcriptional regulation of adipocyte metabolism. Tufts University PhD Thesis, 2010. Abstracts International, Volume: 71-06, Section: B, page: 3810.
- Shillabeer G, Forden JM, Lau DC. Induction of preadipocyte differentiation by mature fat cells in the rat. *The Journal of clinical investigation*.84:381-7. 1989.
- Si Y, Yoon J, Lee K: Flux profile and modularity analysis of time-dependent metabolic changes of de novo adipocyte formation. *Am J Physiol Endocrinol Metab* 2007, 292:E1637-1646.
- Si Y, Shi H, Lee K: Impact of perturbed pyruvate metabolism on adipocyte triglyceride accumulation. *Metab Eng* 2009, 11:382-390.
- Sims JK, Manteiga S, Lee K. Towards High Resolution Analysis of Metabolic Flux in Cells and Tissues. *Curr Opin Biotechnol*. 2013, 24: 933-939.
- Sims JK, Rohr B, Miller E, Lee K. Automated Image Processing for Spatially Resolved Analysis of Lipid Droplets in Cultured 3T3-L1 Adipocytes. *Tissue Eng Part C Methods*. 2014 Nov 12. [Epub ahead of print]
- Smith KM, Liao JC: An evolutionary strategy for isobutanol production strain development in *Escherichia coli*. *Metab Eng* 2011, 13:674-681.
- Srivastava S, Chan C: Application of metabolic flux analysis to identify the mechanisms of free fatty acid toxicity to human hepatoma cell line. *Biotechnol Bioeng* 2008, 99:399-410.
- Stacey DH, Hanson SE, Lahvis G, Gutowski KA, Masters KS. In vitro adipogenic differentiation of preadipocytes varies with differentiation stimulus, culture dimensionality, and scaffold composition. *Tissue engineering Part A*.15:3389-99. 2009.
- Strigun A, Noor F, Pironti A, Niklas J, Yang TH, Heinzle E: Metabolic flux analysis gives an insight on verapamil induced changes in central metabolism of HL-1 cells. *J Biotechnol* 2011, 155:299-307.
- Strigun A, Wahrheit J, Niklas J, Heinzle E, Noor F: Doxorubicin increases oxidative metabolism in HL-1 cardiomyocytes as shown by <sup>13</sup>C metabolic flux analysis. *Toxicol Sci* 2012, 125:595-606.

- Strissel, K.J., Stancheva, Z., Miyoshi, H., Perfield 2nd, J.W., DeFuria, J., Jick, Z., Greenberg, A.S., Obin, M.S.: Adipocyte death, adipose tissue remodeling, and obesity complications. *Diabetes* **56**(12), 2910–2918 (2007).
- Sun, K., Kusminski, C.M., Scherer, P.E.: Adipose tissue remodeling and obesity. *J. Clin. Investig.* **121**(6), 2094–2101 (2011).
- Thiele I, Swainston N, Fleming RM, Hoppe A, Sahoo S, Aurich MK, Haraldsdottir H, Mo ML, Rolfsson O, Stobbe MD, et al.: A community-driven global reconstruction of human metabolism. *Nat Biotechnol* 2013, 31:419-425.
- Wang X, Yomano LP, Lee JY, York SW, Zheng H, Mullinnix MT, Shanmugam KT, Ingram LO: Engineering furfural tolerance in *Escherichia coli* improves the fermentation of lignocellulosic sugars into renewable chemicals. *Proc Natl Acad Sci U S A* 2013, 110:4021-4026.
- Walther TC, Farese RV, Jr. The life of lipid droplets. *Biochimica et biophysica acta.*1791:459-66. 2009.
- Walther TC, Farese RV Jr. Lipid droplets and cellular lipid metabolism. *Annu Rev Biochem.* 2012;81:687-714.
- Wiechert W. <sup>13</sup>C metabolic flux analysis. *Metab Eng.* 2001 Jul;3(3):195-206.
- Wilson-Fritch L, Nicoloso S, Chouinard M, Lazar MA, Chui PC, Leszyk J, Straubhaar J, Czech MP, Corvera S. Mitochondrial remodeling in adipose tissue associated with obesity and treatment with rosiglitazone. *J Clin Invest* 2004, 114:1281–1289.
- Wolins NE, Quaynor BK, Skinner JR, Schoenfish MJ, Tzekov A, Bickel PE. S3-12, Adipophilin, and TIP47 package lipid in adipocytes. *The Journal of biological chemistry.*280:19146-55. 2005.
- Xu HN, Zheng G, Tchou J, Nioka S, Li LZ: Characterizing the metabolic heterogeneity in human breast cancer xenografts by 3D high resolution fluorescence imaging. *Springerplus* 2013, 2:73.
- Yang H, Roth CM, Ierapetritou MG: Analysis of amino acid supplementation effects on hepatocyte cultures using flux balance analysis. *OMICS* 2011, 15:449-460.